University of Windsor

Scholarship at UWindsor

Electronic Theses and Dissertations

Theses, Dissertations, and Major Papers

1-1-2006

Active brake proportioning and its effects on safety and performance.

Nathan C. Nantais
University of Windsor

Follow this and additional works at: https://scholar.uwindsor.ca/etd

Recommended Citation

Nantais, Nathan C., "Active brake proportioning and its effects on safety and performance." (2006). *Electronic Theses and Dissertations*. 7067.
https://scholar.uwindsor.ca/etd/7067

This online database contains the full-text of PhD dissertations and Masters' theses of University of Windsor students from 1954 forward. These documents are made available for personal study and research purposes only, in accordance with the Canadian Copyright Act and the Creative Commons license—CC BY-NC-ND (Attribution, Non-Commercial, No Derivative Works). Under this license, works must always be attributed to the copyright holder (original author), cannot be used for any commercial purposes, and may not be altered. Any other use would require the permission of the copyright holder. Students may inquire about withdrawing their dissertation and/or thesis from this database. For additional inquiries, please contact the repository administrator via email (scholarship@uwindsor.ca) or by telephone at 519-253-3000ext. 3208.

ACTIVE BRAKE PROPORTIONING AND ITS EFFECTS ON SAFETY AND PERFORMANCE

By
Nathan C. Nantais

A Thesis
Submitted to the Faculty of Graduate Studies and Research
through Mechanical Engineering
in Partial Fulfillment of the Requirements for
the Degree of Master of Applied Science at the
University of Windsor

Windsor, Ontario, Canada
2006

© Copyright by Nathan C. Nantais, 2006

Library and
Archives Canada

Published Heritage
Branch

395 Wellington Street
Ottawa ON K1A 0N4
Canada

Bibliothèque et
Archives Canada

Direction du
Patrimoine de l'édition

395, rue Wellington
Ottawa ON K1A 0N4
Canada

Your file Votre référence
ISBN: 978-0-494-35928-0
Our file Notre référence
ISBN: 978-0-494-35928-0

NOTICE:
The author has granted a non-exclusive license allowing Library and Archives Canada to reproduce, publish, archive, preserve, conserve, communicate to the public by telecommunication or on the Internet, loan, distribute and sell theses worldwide, for commercial or non-commercial purposes, in microform, paper, electronic and/or any other formats.

The author retains copyright ownership and moral rights in this thesis. Neither the thesis nor substantial extracts from it may be printed or otherwise reproduced without the author's permission.

AVIS:
L'auteur a accordé une licence non exclusive permettant à la Bibliothèque et Archives Canada de reproduire, publier, archiver, sauvegarder, conserver, transmettre au public par télécommunication ou par l'Internet, prêter, distribuer et vendre des thèses partout dans le monde, à des fins commerciales ou autres, sur support microforme, papier, électronique et/ou autres formats.

L'auteur conserve la propriété du droit d'auteur et des droits moraux qui protège cette thèse. Ni la thèse ni des extraits substantiels de celle-ci ne doivent être imprimés ou autrement reproduits sans son autorisation.

In compliance with the Canadian Privacy Act some supporting forms may have been removed from this thesis.

While these forms may be included in the document page count, their removal does not represent any loss of content from the thesis.

Conformément à la loi canadienne sur la protection de la vie privée, quelques formulaires secondaires ont été enlevés de cette thèse.

Bien que ces formulaires aient inclus dans la pagination, il n'y aura aucun contenu manquant.

Canada

Abstract

A vehicle undergoing longitudinal or lateral accelerations experiences load transfer, dynamically changing the load carried by each tire. Conventional braking systems are designed only to work adequately over a large range of conditions, but ignore the dynamic state of the tires. Fortunately, new developments in braking system hardware include electro-hydraulic and electromechanical brakes, which give designers full control over the application of braking pressures.

The purpose of this research is to investigate possible advantages of active brake pressure control. By estimating the tractive ability of the tires as a function of measurable vehicle conditions, brake pressure can be applied in proportions appropriate for the current dynamic state of the vehicle. The result is increased braking ability before the onset of tire lockup (or ABS activation). Stopping distances are improved for all braking situations, and vehicle stability is improved during extreme obstacle avoidance maneuvers.

To my parents.

Acknowledgements

This work would not be possible without the support of Drs. Bruce Minaker and Greg Rohrauer, with whose assistance I selected this thesis topic. It was a great pleasure to complete my thesis work under the supervision of Dr. Minaker, whose acumen I have found to be second to none. I was only ever stuck on a problem for as long as it took me to find him and pick his brain.

I was extremely fortunate to obtain the generous support of the AUTO21 Network of Centres of Excellence, Natural Sciences and Engineering Research Council of Canada (NSERC), and Ontario Graduate Scholarships in Science and Technology (OGSST). The funding allowed me to pursue my automotive engineering research interests, which would not have been otherwise possible.

I would be remiss if I did not thank my longtime colleagues Sinisa Draca, E.W.K. Oh, Robert Rieveley, and Alex Wood. In two years we shared a lot of knowledge and laughs. I would also like to acknowledge and thank our fellow AUTO21 researchers at the University of Waterloo and the University of British Columbia.

Table of Contents

Abstract iii

Dedication iv

Acknowledgements v

List of Tables ix

List of Figures x

List of Symbols xv

1 Introduction 1

2 Literature Review 2
- 2.1 Braking Systems . . . 2
- 2.2 Antilock Braking System . . . 5
- 2.3 Electronic Braking Hardware and Control . . . 7

3 The Pneumatic Tire 9
- 3.1 Construction . . . 9
- 3.2 Slip . . . 11
- 3.3 Load sensitivity . . . 15
- 3.4 The Traction Circle . . . 17
- 3.5 Tire Modeling . . . 19
  - 3.5.1 Tire models for ride and durability . . . 19
  - 3.5.2 Tire models for handling . . . 20

4 Forming and Solving Equations of Motion 26
- 4.1 Newton's Equations and Eigen Analysis . . . 26
- 4.2 Vehicle Dynamics and Linear Models . . . 30
  - 4.2.1 The Bicycle Model . . . 30
  - 4.2.2 Quarter-Car and Bounce/Pitch Models . . . 33
- 4.3 Vehicle Modeling With CarSim . . . 34
  - 4.3.1 Model - General . . . 35
  - 4.3.2 Suspension . . . 36

4.3.3 Aerodynamics . . . 36
4.3.4 Steering . . . 37
4.3.5 Brakes . . . 37
4.3.6 Powertrain . . . 38
4.3.7 Tires . . . 39
4.3.8 Solver Method . . . 39

5 Braking Dynamics **41**
5.1 Braking Stability . . . 41
5.2 Static Vehicle Properties . . . 43
5.3 Dynamics and Load Transfer . . . 44
5.4 Braking Forces . . . 45
5.5 Lines of Constant Friction Coefficient . . . 48
5.6 Static Brake Proportioning . . . 53
5.7 Design of Static Brake Proportioning . . . 55
5.7.1 Braking Efficiency . . . 55
5.7.2 Design of Variable Brake Proportioning . . . 57

6 Brake Control Development **59**
6.1 Longitudinal Load Transfer . . . 60
6.1.1 Equivalent Mass . . . 60
6.1.2 Kinematics . . . 65
6.1.3 Longitudinal load transfer results . . . 67
6.2 Lateral Load Transfer . . . 71
6.2.1 Roll Force analysis . . . 71
6.2.2 Load transfer analysis . . . 75
6.2.3 Kinematics . . . 78
6.2.4 Lateral load transfer results . . . 79
6.3 Combined Longitudinal and Lateral Load Transfer . . . 83
6.4 Tractive Capabilities Prediction . . . 84
6.5 Tire Slip Correction . . . 86
6.5.1 Offset for front-locking . . . 89
6.6 Results: Tire slip correction . . . 89
6.7 Brake control system operation overview . . . 91

7 Steering effects of brake control **93**
7.1 Forces on a cornering vehicle . . . 93
7.2 Steer by steered wheels . . . 94
7.2.1 Steering forces in steady-state cornering . . . 95
7.3 Steer by laterally uneven brake forces . . . 98
7.4 Steering effect simulations . . . 101
7.4.1 Cornering and braking to a full stop . . . 101
7.4.2 Cornering at 110 $\frac{km}{h}$ and braking to 80 $\frac{km}{h}$ . . . 104
7.5 Discussion of results . . . 107

8 Braking Simulations **109**
8.1 Overview . . . 109
8.2 Straight-line braking . . . 110
8.2.1 Straight-line braking: Non-ABS vehicles . . . 111
8.2.2 Straight-line braking: ABS vehicles . . . 116
8.3 Braking while cornering . . . 119
8.3.1 Braking while cornering: Non-ABS vehicles . . . 120
8.3.2 Braking while cornering: ABS vehicles . . . 125
8.4 Braking and cornering with obstacle . . . 130
8.4.1 Braking and cornering with obstacle (inside swerve): Non-ABS vehicles 130
8.4.2 Braking and cornering with obstacle (inside swerve): ABS vehicles . 136
8.5 Discussion of Results . . . 141

9 Conclusions and Recommendations **144**

References **148**

Appendix A CarSim large sedan vehicle model **151**

Appendix B Predictive controls: alternate vehicle **153**

Appendix C Additional simulation result plots **156**
C.1 Braking and cornering with obstacle (inside swerve) . . . 156
C.1.1 Braking and cornering with obstacle (inside swerve): ABS vehicles . 156
C.2 Braking and cornering with obstacle (outside swerve) . . . 158
C.2.1 Braking and cornering with obstacle (outside swerve): ABS vehicles 163

Vita Auctoris **169**

List of Tables

8.1 Straight line braking (no ABS): Simulation results summary 111

8.2 Straight line braking (with ABS): Simulation results summary 116

8.3 Cornering and braking (no ABS): Simulation results summary 120

8.4 Cornering and braking (with ABS): Simulation results summary 125

8.5 Braking and cornering with obstacle (inside swerve, no ABS): Simulation results summary 130

8.6 Braking and cornering with obstacle (inside swerve, with ABS): Simulation results summary 136

A.1 CarSim large sedan vehicle model parameters 152

B.1 CarSim crossover vehicle model parameters 154

C.1 Braking and cornering with obstacle (outside swerve, no ABS): Simulation results summary 158

C.2 Braking and cornering with obstacle (outside swerve, with ABS): Simulation results summary 163

List of Figures

2.1 Drum brakes 3
2.2 Disc brakes 4
2.3 Tire adhesive capabilities vs. slip ratio 6

3.1 Tire carcass (beads and radial chords) 10
3.2 Tire tread 10
3.3 Pneumatic tire - Chord (ply) angles 11
3.4 Coefficient of friction vs. Slip ratio 12
3.5 Tire contact patch - Slip ratio 13
3.6 Tire slip angle 14
3.7 Tire lateral force vs. slip angle for three normal load cases 15
3.8 Tire lateral force coefficient vs. slip angle for three normal load cases 16
3.9 Longitudinal and lateral tire forces 17
3.10 Tire traction circle 18
3.11 Tire model - Vertical ride / vibration model (quarter-car) 20
3.12 Tire model - Radial spring model for rough terrain 21
3.13 Tire forces - Contact patch forces 22

4.1 Simple spring / mass / damper system 27
4.2 Bicycle model vehicle representation 31
4.3 Bounce-pitch model vehicle representation 34

5.1 Free body diagram of braking vehicle with front tires locked up 42
5.2 Free body diagram of braking vehicle with rear tires locked up 43
5.3 Optimal braking force curve 47
5.4 Normalized optimal brake force parabola 49
5.5 Normalized optimal brake forces showing acceleration and deceleration region 50

5.6 Normalized optimal brake force parabola with lines of constant friction coefficient . . . 51
5.7 Normalized optimal brake force parabola with constant friction lines 52
5.8 Optimal brake force parabola with stable static brake proportioning line . . 53
5.9 Optimal brake force parabola with unstable static brake proportioning line 54
5.10 Normalized optimal brake forces for two different rear load cases 55
5.11 Limitations of linear static brake proportioning 56
5.12 Bi-linear brake force proportioning curve using limiter valve 57
5.13 Bi-linear brake force proportioning curve using reducer valve 58

6.1 Sliding mass representation of a braking vehicle 61
6.2 Sliding and rolling mass representation of a braking vehicle 61
6.3 Detailed vehicle longitudinal load transfer free body diagram 63
6.4 Longitudinal load transfer vs. acceleration for simplified and detailed equations 64
6.5 Vehicle sprung vs unsprung mass 65
6.6 Suspension motion during longitudinal deceleration 66
6.7 Change in CG height and longitudinal deceleration vs. time 68
6.8 Simulink block diagram for longitudinal load transfer prediction 69
6.9 Normal loads during longitudinal deceleration (CarSim and predicted) . . . 69
6.10 Percent error in normal load transfer prediction during longitudinal deceleration . . . 70
6.11 Suspension and tire as springs in series 73
6.12 Free body diagram for roll stiffness calculation 74
6.13 Vehicle roll centres and roll axis 76
6.14 CG height change as vehicle undergoes lateral acceleration 78
6.15 Simulink block diagram for lateral load transfer prediction 79
6.16 Steady state cornering error in roll angle prediction 80
6.17 Tire loads during cornering maneuver 81
6.18 Error in tire normal load prediction during steady state cornering 82
6.19 Simulink module for longitudinal and lateral combined load transfer 83
6.20 Tire lateral load capabilities vs. normal load 84
6.21 Tire load sensitivity: μ trend and peak tractive load trend (exaggerated values) . . . 86
6.22 Tire load sensitivity: μ trend and peak tractive load trend 87

6.23 Tire lockup order during braking, vehicle with slip compensation vs. vehicle without slip compensation 90
6.24 Tire lockup order during braking, baseline vehicle 91

7.1 Cornering bicycle model: steer angle and tire slip angles 96
7.2 Steer angle versus vehicle forward speed and corner radius 97
7.3 Braking and cornering forces with and without ABP 98
7.4 Simulation of lateral steering effect of laterally proportioned braking forces 99
7.5 Vehicle path change caused by laterally proportioned brake forces 100
7.6 Master cylinder brake pressure for brake-steer simulations 101
7.7 Steering wheel angle - baseline versus ABP vehicle 102
7.8 Steering wheel torque - baseline versus ABP vehicle 103
7.9 Steering wheel angle - baseline versus ABP vehicle: Braking 110 $\frac{km}{h}$ to 80 $\frac{km}{h}$ 105
7.10 Steering wheel torque - baseline versus ABP vehicle, braking 110 $\frac{km}{h}$ to 80 $\frac{km}{h}$. 106

8.1 Master cylinder brake pressure curve for straight line braking 111
8.2 Straight line braking (no ABS): Vehicle and wheel speeds 112
8.3 Straight line braking (no ABS): Brake pressure 113
8.4 Straight line braking (no ABS): "Braking curve" - front axle braking versus rear axle braking 114
8.5 Straight line braking (no ABS): Longitudinal deceleration 115
8.6 Straight line braking (ABS): Vehicle and wheel speeds 117
8.7 Straight line braking (ABS): Brake pressure 118
8.8 Straight line braking (ABS): Longitudinal deceleration 118
8.9 Master cylinder pressure for braking while cornering simulations 119
8.10 Cornering and braking (no ABS): Vehicle and wheel speeds 121
8.11 Cornering and braking (no ABS): Brake pressure 122
8.12 Cornering and braking (no ABS): "Braking curves" - front braking versus rear braking, and inside braking versus outside braking 123
8.13 Cornering and braking (no ABS): Steering wheel angle and steering wheel torque 123
8.14 Cornering and braking (no ABS): Longitudinal deceleration and lateral acceleration 124
8.15 Cornering and braking (no ABS): Lateral deviation from desired path . . . 124
8.16 Cornering and braking (with ABS): Vehicle and wheel speeds 126
8.17 Cornering and braking (with ABS): Brake pressure 127

8.18 Cornering and braking (with ABS): Steering wheel angle and steering wheel torque . . . 128
8.19 Cornering and braking (with ABS): Longitudinal deceleration and lateral acceleration . . . 128
8.20 Cornering and braking (with ABS): Lateral deviation from desired path . . 129
8.21 Braking and cornering with obstacle (inside swerve, no ABS): Vehicle and wheel speeds . . . 131
8.22 Braking and cornering with obstacle (inside swerve, no ABS): Body slip angle 132
8.23 Braking and cornering with obstacle (inside swerve, no ABS): Brake pressure 133
8.24 Braking and cornering with obstacle (inside swerve, no ABS): Steering wheel angle and steering wheel torque . . . 134
8.25 Braking and cornering with obstacle (inside swerve, no ABS): Longitudinal deceleration and lateral acceleration . . . 134
8.26 Braking and cornering with obstacle (inside swerve, no ABS): Vehicle trajectory . . . 135
8.27 Braking and cornering with obstacle (inside swerve, with ABS): Wheel and vehicle forward speeds . . . 137
8.28 Braking and cornering with obstacle (inside swerve, with ABS): Body slip angle . . . 138
8.29 Braking and cornering with obstacle (inside swerve, with ABS): Brake pressure 139
8.30 Braking and cornering with obstacle (inside swerve, with ABS): Vehicle trajectory . . . 140

A.1 Graphical representation of CarSim large sedan model . . . 151

B.1 Graphical representation of CarSim crossover vehicle model . . . 153
B.2 Tire loads during cornering maneuver (crossover vehicle model) . . . 155

C.1 Braking and cornering with obstacle (inside swerve, with ABS): Steering wheel angle and steering wheel torque . . . 156
C.2 Braking and cornering with obstacle (inside swerve, with ABS): Longitudinal deceleration and lateral acceleration . . . 157
C.3 Braking and cornering with obstacle (inside swerve, with ABS): Lateral deviation from desired path . . . 157
C.4 Braking and cornering with obstacle (outside swerve, no ABS): Vehicle and wheel speeds . . . 159

C.5 Braking and cornering with obstacle (outside swerve, no ABS): Brake pressure 160

C.6 Braking and cornering with obstacle (inside swerve, no ABS): Body slip angle 160

C.7 Braking and cornering with obstacle (outside swerve, no ABS): Steering wheel angle and steering wheel torque 161

C.8 Braking and cornering with obstacle (outside swerve, no ABS): Longitudinal deceleration and lateral acceleration 161

C.9 Braking and cornering with obstacle (outside swerve, no ABS): Lateral deviation from desired path 162

C.10 Braking and cornering with obstacle (outside swerve, no ABS): Vehicle trajectory 162

C.11 Braking and cornering with obstacle (outside swerve, with ABS): Wheel and vehicle forward speeds 164

C.12 Braking and cornering with obstacle (outside swerve, with ABS): Brake pressure 165

C.13 Braking and cornering with obstacle (inside swerve, with ABS): Body slip angle 166

C.14 Braking and cornering with obstacle (outside swerve, with ABS): Steering wheel angle and steering wheel torque 166

C.15 Braking and cornering with obstacle (outside swerve, with ABS): Longitudinal deceleration and lateral acceleration 167

C.16 Braking and cornering with obstacle (outside swerve, with ABS): Lateral deviation from desired path 167

C.17 Braking and cornering with obstacle (outside swerve, with ABS): Vehicle trajectory 168

List of Symbols

The notation throughout this work is used to denote mathematical types. The notations for specific entities are listed below.

Label	Description
ABP	Active brake proportioning
ABS	Anti-lock braking system
a	Longitudinal distance from vehicle front axle to CG
$\vec{a}$	Acceleration
b	Longitudinal distance from vehicle rear axle to CG
c_{front}, c_{rear}	Front and rear suspension damping, respectively
c_s	Suspension damping
c_tire	Tire vertical damping
C_α, C, C_f, Cr	Tire cornering stiffness (general, general, front, rear, respectively)
CG	Vehicle centre of gravity
E	Energy stored in a moving vehicle
E_F, E_R	Front and rear braking efficiency, respectively
$\vec{f}$	Vector of external forces
F	Force
F_f, F_r	Lateral force on front and rear tires, respectively
$F_{i,y}$	Lateral force at axle (general, i = 'Front' or 'Rear')
F_{Xi}	Braking force on the i^{th} axle
F_{XF}	Braking force on front axle
F_{XR}	Braking force on rear axle
$F_{XF,opt}$, $F_{XR,opt}$	Optimal front and rear braking forces, respectively

Label	Description
$F_{zF,static}$, $F_{zR,static}$	Front and rear static axle loads, respectively
$F_{zi,dyn}$	Dynamic normal load on the i^{th} axle
$F_{zF,dyn}$, $F_{zR,dyn}$	Dynamic normal load on the front and rear axles, respectively
h_{rc}	Height of roll centre above ground
h_s	Height of CG above roll centre
I	Mass moment of inertia
k_1, k_2, k_3, k_4	Runge-Kutta derivatives
k_s	Suspension spring stiffness
k_{front}, k_{rear}	Front and rear suspension stiffness, respectively
k_tire, $or\ k_t$, $or\ k_{tf}, k_{tr}$	Tire vertical stiffness (general, front, rear, respectively)
K_{arb}	Anti-roll bar stiffness
K_{roll_i}	Stiffness of suspension in roll (i = 'front' or 'rear'
L	Wheelbase
ΔL	Load transfer due to acceleration
m	Mass
$m_{effective}$	Effective mass of vehicle including inertial effects
m_{sprung}	Vehicle sprung mass
m_{tire}	Mass of wheel and tire assembly
$M\ orT$	Moment; torque
M_{arb}	Moment applied by anti-roll bar
$M_{\phi,i}$	Moment caused by roll about the i^{th} axle
$M_{rigid,i}$	Moment caused by lateral load transfer through rigid path
$P_{brake,i}$	Brake pressure applied at the i^{th} wheel
r	Yaw rate
r_{tire}	Tire rolling radius
R	Vehicle turning radius
t	Time
$T\ or\ t$	Track width
u	Forward velocity in vehicle-fixed coordinates
v	Lateral velocity in vehicle-fixed coordinates
$\vec{v}$	Velocity

Label	Description
$V_{vehicle}$	Vehicle forward velocity
V_{wheel}	Tire contact patch forward velocity
W	Vehicle curb weight
W_f, W_r	Static weight on front and rear axles, respectively
z_{ground}	Ground vertical motion
$[A]$	Dynamic matrix
$[C]$	Damping matrix
$[K]$	Stiffness matrix
$[M]$	Mass matrix
α	Tire slip angle
$\vec{\alpha}$	Rotational acceleration
β	Body slip angle
γ	Tire camber angle
δ	Steer angle
θ	Pitch angle
κ	Tire longitudinal slip ratio
$\mu_{friction}$, $\mu_{friction}i$	Tire-road coefficient of friction (general, i = F(ront) or R(ear))
μ *or* μ_{Ti}	Traction coefficient of the i^{th} axle
μ_{front} / μ_f, μ_{rear} / μ_r	Traction coefficient of the front and rear axles, respectively
ϕ	Roll angle
Φ	Static brake proportioning ratio
χ	Ratio of CG height to wheelbase
Ψ	Ratio of static rear axle load to total vehicle weight
Ψ	Yaw (heading) angle
$\vec{\omega}$	Rotational velocity

Chapter 1

Introduction

The behaviour of an automobile undergoing braking is critical in terms of both performance and passenger safety. The brakes are the single-most important safety component on an automobile, and are charged with the vital task of stopping the moving vehicle. The basic goals of braking systems are to decelerate a vehicle during stopping, to maintain vehicle speed during downhill operation, and to hold a vehicle stationary on a grade [17]. The design goals of the deceleration aspect of the braking system can then be expanded:

> The braking system must slow the vehicle to a stop with an adequate deceleration level...

- Subject to varying vehicle conditions (loading, etc.)
- In a manner that utilizes as much of the available traction as possible over a large range of road conditions
- Without causing vehicle instability during braking events
- In a manner that is predictable to the driver

Like many other aspects of automobile design, brake hardware is conventionally designed as a compromise between the different performance requirements. Furthermore, a factor of safety is designed into the components to assume close to worst case scenario road conditions, severely limiting performance in favourable conditions. New developments in electronic braking devices will give brake designers the freedom to control brakes without compromise, in order to ensure optimal braking and vehicle stability under all conditions. This thesis will investigate some of the possibilities in this area.

Chapter 2

Literature Review

2.1 Braking Systems

The mechanics of the brake devices found on today's automobiles have been well established for decades, and have been well summarized and described by Heisler [11]. Heisler states that "a hydraulic braking system is a compact method of transmitting the driver's foot-pedal effort to the individual road-wheel brakes by conveying pressurized fluid from one position to another and then converting the fluid pressure into useful work at the wheels to apply the brakes and so retard or stop the rotation of the wheels" [11]. Preceding very recent developments in electronics, all modern passenger automobiles used hydraulic fluid circuits to actuate their brakes. Mechanical brakes, where only a mechanical linkage such as a cable actuates the brake, are commonly used for static applications such as parking brakes. Air actuated brakes are also commonly used on large transport trucks.

The actual hardware device used to brake the rotating wheels has predominantly been *drum brakes* during most of the past century (Figure 2.1). Drum brake systems consist of pivoting brake *shoes* which are contained within, and forced outward into, a drum which is fixed to the rotating wheel [11]. The alternative to drum brakes is *disc brakes*, for which a disc (rather than a drum) is fixed to the rotating wheel, and sandwiched between two pistons and friction pads (Figure 2.2). The brake pads clamp the faces of the disc during brake application. Since their introduction, disc brakes have proven themselves to be the superior technology, and are used almost exclusively at the front axle of passenger cars and trucks, and without exception at all four wheels on performance vehicles [17].

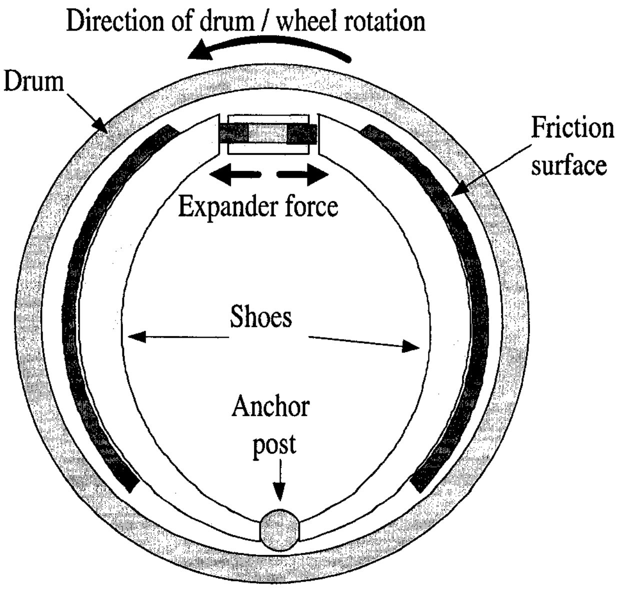

Figure 2.1: *Drum brakes.* Drum brakes slow the vehicle by pressing friction pads outward into the inner radius of a drum that is fixed to the rotating wheel. The friction pads are fixed to *shoes*, which pivot at an anchor post.

Limpert [17] has provided a far-reaching and in-depth summary of the equations governing typical braking system design and analysis. Of particular concern are the equations governing the changes in tractive ability at the different tires during braking events, and the consequential design methods used for brake force proportioning. Limpert defines the *traction coefficient* as the "ratio of braking force to dynamic axle load" [17] (Equation 2.1.1).

$$\mu_{Ti} = \frac{F_{xi}}{F_{zi,dyn}} \tag{2.1.1}$$

where:

μ_{Ti} = traction coefficient of the i^{th} axle

F_{xi} = braking force at the i^{th} axle

$F_{zi,dyn}$ = dynamic normal load on the i^{th} axle

The traction coefficient is not the same as the *tire-road friction coefficient.* The tire-road friction coefficient essentially represents the peak attainable traction coefficient. The traction coefficient will then always be less than the tire-road friction coefficient, and can

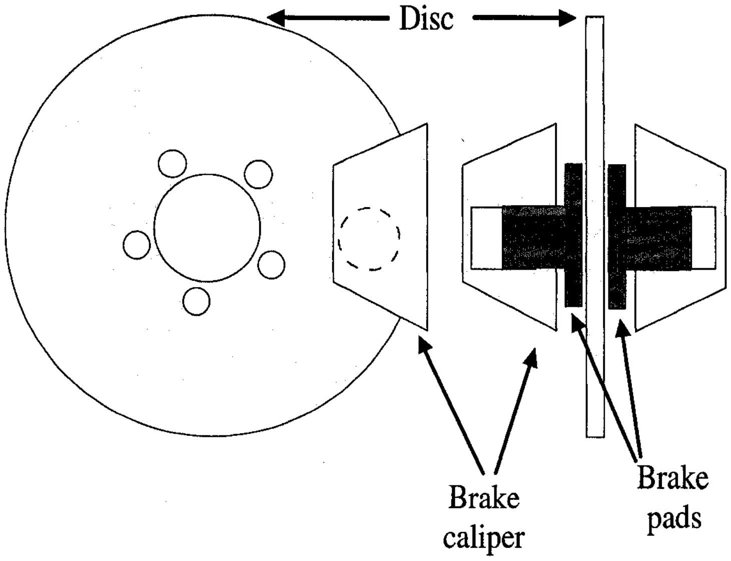

Figure 2.2: *Disc brakes.* Disc brakes slow a vehicle by pressing friction pads into a steel disc (or rotor) that is fixed to the rotating wheel. The brake caliper houses pistons; hydraulic pressure forces the pistons into the brake pads, squeezing the brake rotor.

be interpreted as the portion of the available friction that is utilized to create the current tire forces.

As the driver commands increasing brake force application, the tires will use a larger proportion of the available traction, until the traction coefficient reaches the limit of available tire-road friction. Limpert further states that "when both axles are braked at sufficient levels so that the front and rear wheels are operating at incipient or peak friction conditions, then the maximum traction capacity between the tire-road system is utilized" [17]. Thus, braking system design is concerned with applying the proper braking forces F_{xi} to utilize the same traction coefficient at the front and rear axles for all levels of deceleration, until the point where maximum available braking is achieved (Equation 2.1.2). This is known as *optimal braking.*

$$\mu_{front} = \mu_{rear} = \mu_{friction} = vehicle\ acceleration\ \ [g] \tag{2.1.2}$$

where:

μ_{front} = traction coefficient of front axle

μ_{rear} = traction coefficient of rear axle

$\mu_{friction}$ = tire-road friction coefficient

Brake force proportioning is typically designed with a static front to rear ratio to closely replicate the optimal braking force ratio. The design attempts to optimize a vehicle for straight line braking, with no consideration for cornering dynamics. Design is further complicated by the fact that with increasing tire normal load, the peak achievable coefficient of friction is reduced, in an effect known as *tire load sensitivity* [23]. This effect is not reflected in Limpert's analysis.

2.2 Antilock Braking System

Anti-lock braking systems (ABS) are systems which add a degree of computer control to braking systems in order to improve braking abilities at or near the traction limit. The goal of ABS is to prevent tire lockup during braking, so that the vehicle remains steerable. The system typically consists of wheel-speed sensors, an electronic control unit (ECU), a hydraulic pressure modulator, and four wheel brakes [26].

The electronic computer control algorithm for ABS consists of a set of logical rules which switch the individual brakes on and off according to the sensed wheel speeds [30]. Because of the range of operating conditions under which the ABS system is required to function, the typical controls are quite complicated and are based on extensive physical testing.

In order to achieve the goal of the ABS system, the speed of each of the four wheels is measured and compared [23]. The speeds of the individual wheels are used to closely estimate the tire slip at each wheel. When one tire begins to slip, the brake pressure at that wheel is cut off. This allows the wheel to spin back up to the vehicle speed, at which point the brake pressure to the wheel can be turned back on. In this way the tires are prevented

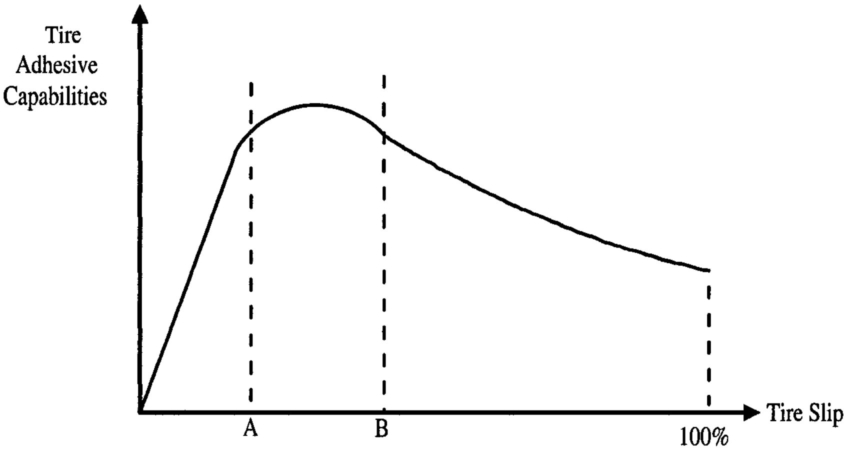

Figure 2.3: *Tire adhesive capabilities vs. slip ratio.* For a rolling tire to create any amount of grip, a portion of the tread will slip on the road. As more grip is demanded of the tire, slip increases until 100% slip, when the tire is "locked up". The peak force is created at a low level of slip, approximately 10%. ABS operation attempts to keep wheel slip near the peak, in the range between points A and B.

from completely locking up. The cycling off and on of the brakes give ABS systems their characteristic pulsing feel. Cycle times are currently in the range of 10 hertz [22].

The precise safety benefits of anti-lock braking systems have been up for debate. According to Denny [4], ABS slightly reduces stopping distances on dry pavement, greatly improves performance on wet pavement, but actually worsens performance on loose surfaces such as gravel or loosely packed snow. It is thought that non-ABS brakes accumulate material in front of the tires during braking on loose surfaces, and this helpful effect is canceled out by the ABS.

There have previously been further doubts about the safety of ABS equipped vehicles, possibly due to the driver's reaction to the system. Farmer et al. [6] found that, all other things being the same, vehicles equipped with ABS were more likely to be involved in accidents fatal to their own passengers, especially single vehicle run-off-the-road accidents and rollovers. The incidence of accidents was reduced for other types of accidents, and the conclusion was that ABS had only a slight effect on the likelihood of fatal crashes. Researchers hypothesized that the large increase in fatal single vehicle accidents could be due to drivers behaving more aggressively due to their confidence in the ABS equipped vehicles, or the fact that the drivers may panic steer the vehicle off the road (as it remains steerable with ABS).

Updated results in 2001 [5] suggested that drivers may have adjusted to ABS systems, and were no longer more likely to drive their vehicles off the road. The author concluded that at best, ABS was producing a modest reduction in fatal motor vehicle accidents.

2.3 Electronic Braking Hardware and Control

Continuing advances in automotive electronics have prompted a trend towards *x-by-wire* technology, whereby typically mechanical components are replaced with electrical equivalents. The inherent advantage is that the designer is granted more freedom in programming an electronically controlled device, as opposed to one with mechanical or hydraulic connections. Throttle-by-wire technology is already seeing widespread integration in passenger automobiles. Steer-by-wire and brake-by-wire are under development and already implemented in a smaller number of cases.

The fundamental distinction of a "brake-by-wire" system is that the brake pedal no longer directly mechanically actuates brake application, but rather produces a sensor value. The actual brake pressure application system may be replaced by an electro-hydraulic combination system [13], or fully electronic motorized brakes [28, 27, 19].

Many systems have made use of active implementation of the wheel brakes to affect vehicle motion (for example [16, 14]). Most research has focused on the correction of yaw behaviour of the cornering vehicle by brake application, rather than braking performance in emergency or evasive stops. Schenk et al. [29] state that "future vehicle brake technology must comprehend the increasing requirements for closed loop control of the normal braking event to minimize variability and provide active control of front-to-rear and side-to-side brake balance".

Choi et al. proposed an electronically controlled braking system using electrorheological brake fluid [3]. The fluid pressure in such a system is modulated using electric current. The authors investigated the possibility of actively controlling front to rear brake proportioning to optimize longitudinal braking in all loading situations. In order to achieve a desired rear tire slip angle at all times a sliding mode controller was implemented, which was validated through hardware-in-the-loop simulation. A similar control scheme was described by Buschmann et al. [2].

Jonner et al. developed an electrohydraulic braking system for Robert Bosch GmbH [13] that allowed four wheel independent brake application. In addition to brake application for yaw control, the authors re-proportioned the brakes based on a *brake force distribution module*, which used "various information about vehicle speed, wheel slip, lateral acceleration, estimated vehicle weight, weight distribution, estimated tire normal force, and estimated brake temperature" [13]. For straight line deceleration the module produced a brake distribution mimicking the "ideal, parabolic, dynamic weight distribution between front and rear" [13]. At low acceleration levels where the tires were not at risk of lockup the authors suggested proportioning more brake force than typically appropriate to the rear to reduce pitch and improve driver *feel*. The normal loads at each tire, the most important variable in determining distribution, were determined using the location of the centre of gravity (CG) and the deceleration of the vehicle.

The authors also proposed re-proportioning the brakes laterally during combined braking and cornering events, as is the subject of this thesis, based on a vehicle model that makes use of a lateral accelerometer sensor. The conclusion was that the active lateral proportioning "can lead to more stable behaviour of the vehicle still before a detected mismatch between the driver's intended course and actual vehicle course leads to a VDC-system interaction" [13], where VDC refers to Bosch's Vehicle Dynamics Control architecture.

Chapter 3

The Pneumatic Tire

Despite one hundred years of development and production the pneumatic tire remains one of the least understood components on the modern automobile. At the same time, it must be recognized that the tire is pivotal in determining both the safety and the performance of any vehicle. This complicated component is the only part of an automobile which comes into contact with the road. Thus, just as the behaviour of a tire will make or break the successful realization of the performance characteristics designed into a vehicle, the modeling of the tires will likewise affect vehicle simulations. As such, it is essential to discuss the tire before discussing the goals and methods of the remainder of this project.

3.1 Construction

A pneumatic tire is a toroid shaped pressure vessel, constructed of two major components: the carcass, and the tread. The tire must be seated on a metal wheel, such that the complete pressure vessel consists of both the tire and the wheel with a sealed seam. The wheel/tire pressure vessel is responsible for supporting the normal load of the vehicle, creating longitudinal and lateral forces in order to accelerate the vehicle, and absorbing bumps and irregularities in the road to improve the quality of the ride.

The carcass (Figure 3.1) is the most important structural element of the tire, and is made up of the two beads and the chords. The beads form two flexible rings which seat the tire on the rim, and serve as the foundation for the carcass. The chords are thin, high-modulus cables constructed of natural, synthetic, or metallic components, which attach the two beads together. They are surrounded by low modulus rubber, which forms the sidewalls of the tire, as well as the surface to which the tread will be attached.

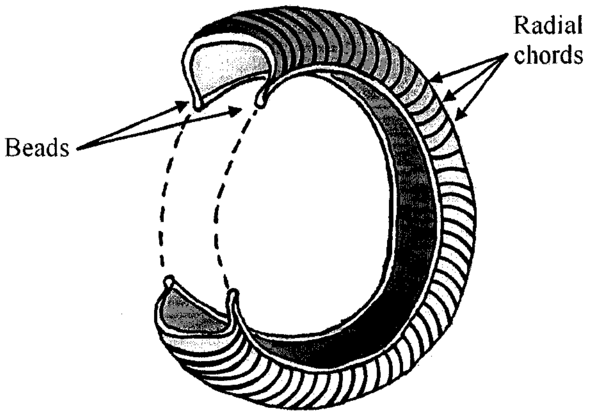

Figure 3.1: *Tire carcass (beads and radial chords).* The base component of the pneumatic tire is the carcass. The carcass is made up of two steel beads, connected by a series of chords.

The tread (Figure 3.2) is the component which actually contacts the road and generates grip. It is bonded to the outside of the carcass. The rubber compounds used in the tread can vary infinitely in order to achieve tradeoffs between adhesive properties, rolling resistance (hysteresis/damping effects), and resistance to abrasion, tears, and crack growth.

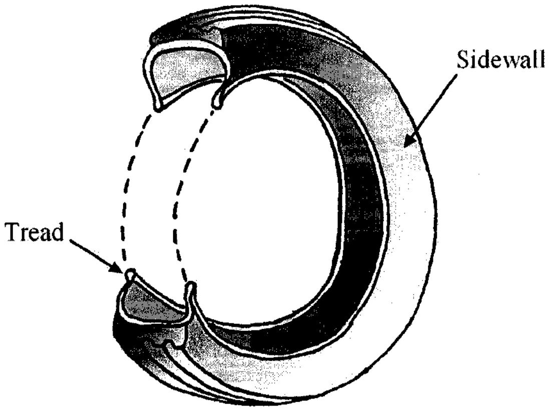

Figure 3.2: *Tire tread.* The tread is the component of the tire that actually contacts the road and creates grip. It is bonded to the carcass to create the complete tire.

The load is transferred from the vehicle into the tire through the wheel, or rim. The rim hangs on the bead of the tire, which loads the cords in the sidewall above the rim in tension. The presence of air pressure in the carcass transfers the load through the tread into the road.

Numberless variations in tire constructions have been used through the years. The angle at which the chords traverse from one bead across to the other, known as the crown angle, is different in different types of tires (Figure 3.3). A radial ply tire has a crown angle of 90° (i.e. the chords go directly around the carcass from one bead to the other). In a bias ply tire the chords crisscross at angles of approximately 40°. The radial ply tire is known as a belted tire, as a belt of chords at a crown angle of approximately 20° runs around the circumference of the tire, under the tread. The belt is necessary to strengthen the radial tire. Bias ply tires are still used in many applications, such as for motorcycles and agricultural machinery, although radial ply tires are now used almost exclusively on passenger cars and trucks.

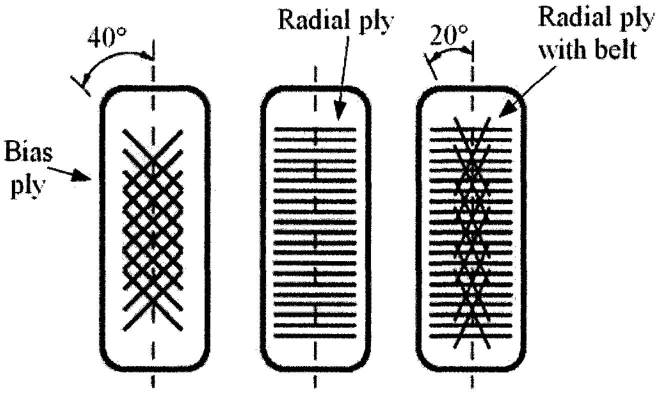

Figure 3.3: *Pneumatic tire - Chord (ply) angles.* The chords attaching the two beads of a tire can be assembled in different arrangements: bias ply, radial ply, and belted radial ply. The chord arrangement greatly influences the performance characteristics of the tire.

3.2 Slip

In order for a tire to create a certain amount of traction, tires must always experience a certain amount of *slip* in the tire-road contact patch. Stated differently, for any level of force transmitted by the tire, a certain amount of slip will exist as a consequence of that force. Thus, slip becomes a useful quantity with which to reference tire forces, and tire force versus tire slip curves are commonly used in automotive engineering (Figure 3.4).

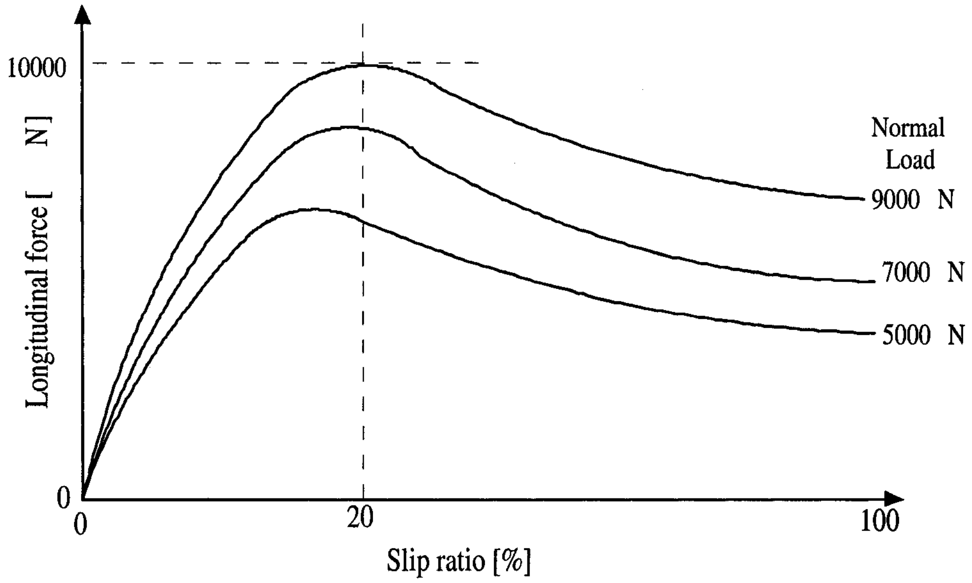

Figure 3.4: *Coefficient of friction vs. Slip ratio.* Example trends of longitudinal load versus tire slip ratio are shown. Note that the curve is different for each tire normal load, and the peak force occurs at a slip ratio in the area of 10 – 25%.

Slip exists because tire sidewalls and treads are flexible. When force is transmitted longitudinally, a moment is created between the bead and the tread on the tire (Figure 3.5). The moment causes the sidewall and tread to deform in shear. The sidewall deforms at the contact patch, but must return to its non-sheared orientation when it lifts off the ground at the rear of the contact patch. The length of contact patch between the deformed sidewall and the sidewall which has returned to its non-deformed shape must slip. As tire forces grow the deformation will increase until the entire contact patch slips, i.e. when the tires spin freely due to excess torque. This is known as 100% slip.

Slip ratio in the longitudinal direction is approximated as the percentage difference between the speed of the wheel / rim and the speed of the vehicle at the contact patch (Equation 3.2.1).

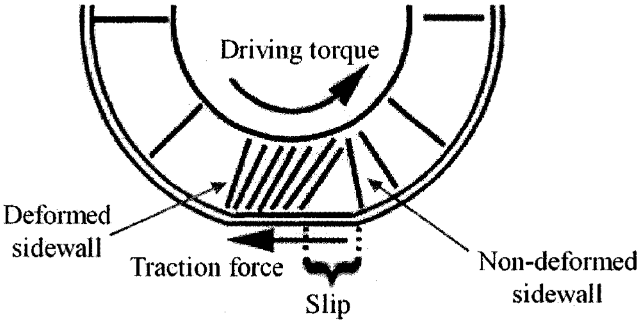

Figure 3.5: *Tire contact patch - Slip ratio.* During driving or braking, longitudinal forces at the tire contact patch cause deflection to occur in the flexible tire sidewall. At the end of the contact patch, where the deformed sidewall must spring back to its non-deformed shape, the contact patch will necessarily slip, by an amount known as the *slip ratio* [32]. The slip ratio consequently grows with growing tire forces, and is thus useful in characterizing tire force characteristics.

$$\begin{aligned} \text{Acceleration: } \% Slip &= \frac{V_{wheel} - V_{vehicle}}{V_{wheel}} \\ \text{Deceleration: } \% Slip &= \frac{V_{vehicle} - V_{wheel}}{V_{vehicle}} \end{aligned} \tag{3.2.1}$$

When a tire must generate lateral forces to cause a vehicle to accelerate laterally, the tire will experience *lateral slip* as it rolls. It is quantified as the difference between the steered angle of the wheel, and the actual rolling direction of the contact patch of the tire (Figure 3.6). Due to the lateral force and steering moments in the contact patch, the tire is deformed in shear and twisted. Therefore, the contact patch follows a path angle less than the steer angle. Similarly to slip ratio, tire lateral force increases with increasing slip angle, and slip angle is thus useful for quantifying tire lateral force characteristics.

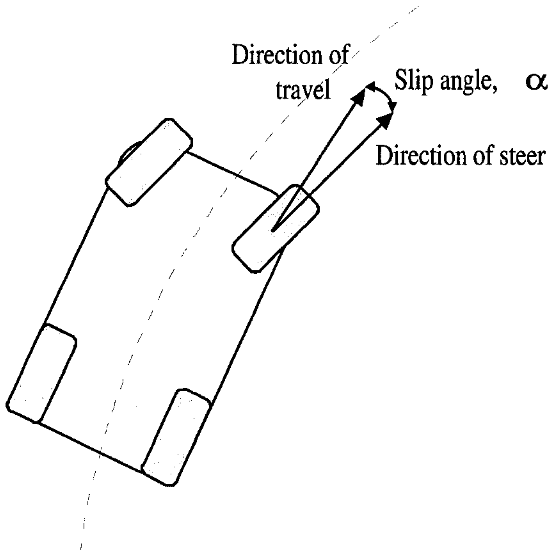
Direction of travel
Slip angle, α
Direction of steer

Figure 3.6: *Tire slip angle.* As a tire is steered, the actual angle of tire travel will be less than the steered angle. The difference between the steered angle and the angle of travel is the *slip angle.* The slip angle results from twisting deflection in the tire sidewall.

3.3 Load sensitivity

Figure 3.7 displays the lateral force versus slip angle trends for one tire at three different normal load cases. Based on the traditional definition of friction forces, $F_{friction} = \mu \cdot F_{normal}$, it may be reasonable to determine the quantity $\frac{F_y}{F_z}$ from the tire data in Figure 3.7.

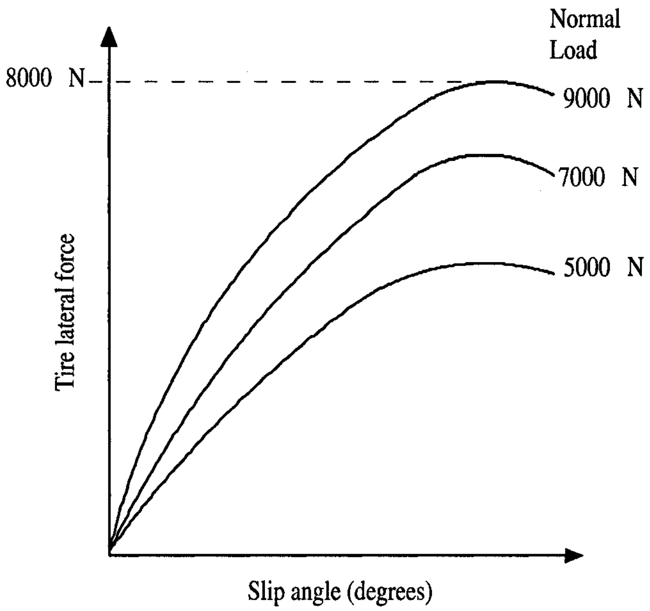

Figure 3.7: *Tire lateral force vs. slip angle for three normal load cases.* Three example trends of tire lateral force versus slip angle are shown. There is a different tire curve for each normal load.

Figure 3.8 displays the lateral force normalized by the normal force, for each of three normal forces. It should be observed that the *traction coefficient*, μ_{tire}, is not constant versus slip or for the different normal load cases.

For a given normal load, there exists a *peak* traction coefficient. And so, the peak traction coefficient itself is a function of normal load, and the coefficient "is normally higher for the lighter loads or, conversely, falls off as the load increases" [23]. In Figure 3.7, the peak force F_y increases with increasing normal load, but in Figure 3.8, the peak ratio decreases with increasing normal load. This effect is known as the load sensitivity of tires.

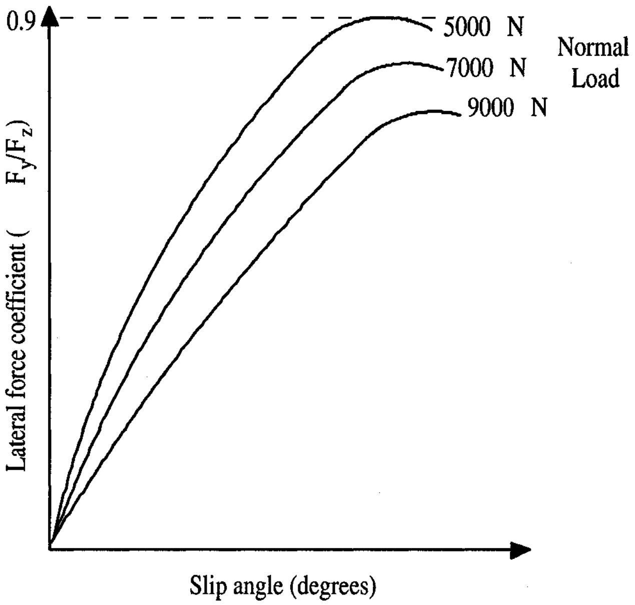

Figure 3.8: *Tire lateral force coefficient vs. slip angle for three normal load cases.* The three example tire trends from Figure 3.7 are plotted as weight-normalized coefficients. Note that the ratio of lateral force to normal force is not constant, as it would be for a conventional frictional mass, at any normal load. Rather, the coefficient follows a curve, unique to each normal load. The lightly loaded tire has the highest force coefficient, and hence generates forces *most efficiently.*

3.4 The Traction Circle

The contact patch of the tire must generate forces in both the longitudinal direction (driving and braking) and in the lateral direction (cornering) (Figure 3.9). As longitudinal and lateral vehicle dynamics are often treated independently, so too are the longitudinal and lateral tire forces.

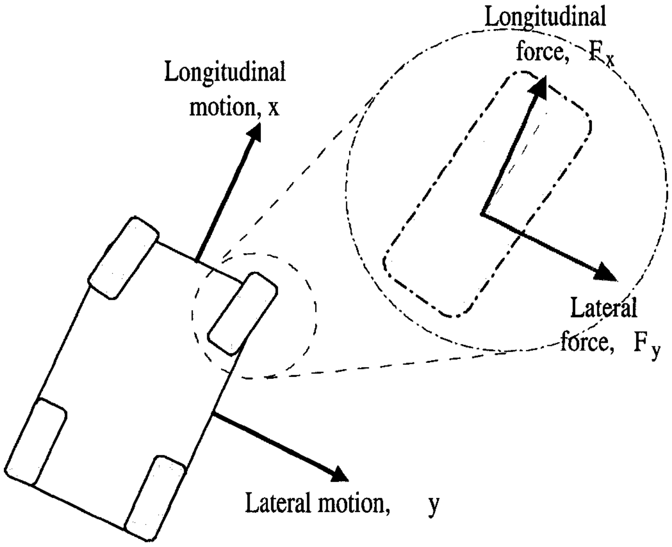

Figure 3.9: *Longitudinal and lateral tire forces.* Vehicle motion is most commonly expressed in the *body-fixed* coordinate system, using x to represent longitudinal motion, and y to represent lateral motion. The longitudinal and lateral forces on each tire are often considered independently, and use the same axis designations as for vehicle motion.

For any set of conditions (normal load, surface conditions, tire pressure, etc.), there is a maximum force which the tire can generate at the road. The force must be the resultant of both the longitudinal and lateral forces generated by the tires. The concept of longitudinal and lateral tire forces, their resultant, and the available total force at the tire are illustrated by the *traction circle* (Figure 3.10).

The traction circle itself can be used to represent the forces on an individual tire, or an entire vehicle. For a vehicle driving in a straight forward line, the traction utilized is purely longitudinal, and would be represented as a vertical arrow. Braking would be an identical

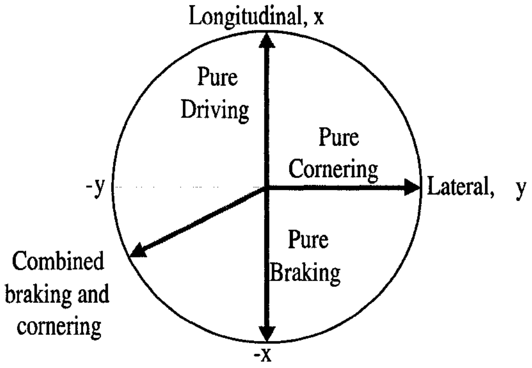

Figure 3.10: *Tire traction circle.* The traction circle is used to graphically represent the relationship between tire longitudinal and lateral forces, and the limits of traction. Any combination of longitudinal and lateral forces at the limits of traction must follow the circular perimeter of the traction circle. Moving outside the circle implies loss of traction.

arrow in the downward (opposite) direction. For a vehicle cornering with no longitudinal acceleration, the location on the traction circle would be somewhere in the horizontal axis, left or right, depending on the direction of the corner.

The circular perimeter of the traction circle represents the *limits* of tire adhesion. Therefore, a vehicle driving along the edge of the traction circle would be straddling the traction limits of the tires, and moving outside the circle implies a loss of traction, and likely stability. Normal everyday driving occurs within the traction circle.

If a vehicle is accelerating longitudinally at the longitudinal limit of the traction circle, it can generate no lateral forces. In order to accelerate laterally into a corner, the longitudinal forces will necessarily decrease, as the traction state moves along the traction circle in the lateral direction. In a combined cornering and driving (or braking) condition, the available traction is shared amongst the two directions. This is the important observation to be taken from the traction circle: longitudinal and lateral tire forces must share the available traction.

Furthermore, because the available traction changes as a function of many conditions, the traction circle can also be represented in three dimensions (or more) [32]. The third dimension could be vehicle speed (as aerodynamic and engine performance effects come into play), or normal load. The traction circle for an individual tire should be expected to expand nearly linearly outward with increasing tire normal load. Empirical data recorded from actual vehicles shows that the actual shape of the traction circle is more elliptical than circular. Hence, the traction circle may be interchangeably referred to as the traction ellipse, or friction ellipse.

3.5 Tire Modeling

Any attempt to model accurately the kinetics of a road-going vehicle system is of questionable value if care is not taken to accurately represent the behaviour of the pneumatic tire. All forces (excluding aerodynamic effects) enter the vehicle through the tires, in reality and in simulation. Thus, although a *vehicle* model may correctly replicate the behaviour of the vehicle given some input forces, without an accurate tire model those input forces will not match those seen in reality. Thus, correlation to experimental data would be impossible.

3.5.1 Tire models for ride and durability

The type of tire model used for a simulation will depend largely on the goals of the simulation. When the goal of modeling is to examine ride or vibration characteristics of the vehicle caused by irregularities and bumps in the road surface, the tire may be as simple as a vertical spring/damper (Figure 3.11). This analysis can be correlated to physical "four-post" test-rig testing.

For modeling the durability of vehicles which must negotiate rough terrain, the type of model would likely involve radial spoke type springs which can envelop irregularities in the track (Figure 3.12). This type of model best resembles the tires used on agricultural and off-road vehicles. It is important to note that model shown is only suitable to simulations of straight-line driving.

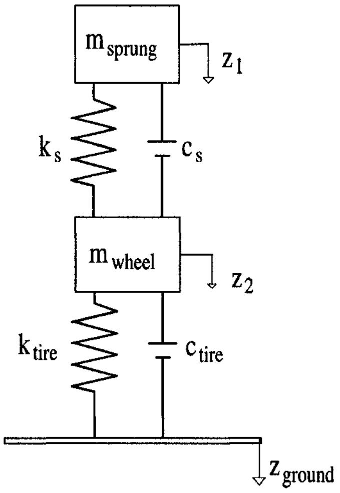

Figure 3.11: *Tire model - Vertical ride / vibration model (quarter-car).* For simulating the effects on ride quality of road irregularities and bumps, a vertical spring tire model may be adequate.

3.5.2 Tire models for handling

When the purpose of the modeling is extended to vehicle handling, the tire model must likewise be extended. The vehicle is entirely controlled by three forces (normal, lateral, and longitudinal) and three moments which the tire applies to the wheel (and in turn the suspension). The three moments generated in the contact patch are known as the overturning moment, M_x, the rolling resistance moment, M_y, and the aligning moment, M_z (Figure 3.13). A model intended to simulate vehicle handling must accurately reproduce some or all of these forces and moments.

The contact patch moments are generated due to the non-symmetric pressure distribution and tire deformation in the tire contact patch. The resultant forces in the contact patch rarely lie directly under the wheel centre; the distance between the contact patch forces and the projected wheel centre act as moment arms.

For a forward-rolling wheel the contact patch moves slightly forward of the wheel centre due to the deformation in the tread and sidewall. The resultant normal force lies in the positive x-axis, resulting in the rolling resistance moment about the wheel centre. The rubber in the tire has inherent damping properties, thus every time tread rubber is

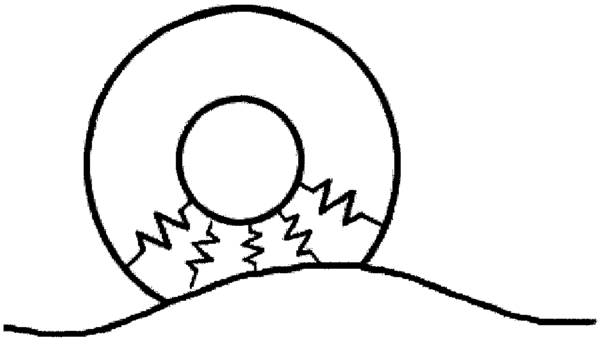

Figure 3.12: *Tire model - Radial spring model for rough terrain.* Tire model capable of large deformations, suitable for straight-line simulations of a vehicle traversing rough terrain.

loaded and unloaded (entering and leaving the contact patch) a proportion of the energy is converted into heat. This results in a rolling resistance force in the direction opposite the driving direction. The rolling resistance force opposes the motion of the vehicle, and creates a moment about the wheel centre equal and opposite of the moment created by the normal load.

While cornering, the shear stress distribution in the contact patch moves rearward by a distance known as the pneumatic trail. Thus, the resultant lateral force occurs behind the wheel centre, creating the self-aligning moment about the wheel centre. This moment provides feedback through the steering system to the driver, and helps steer the tires back to zero steer angle when the driver releases the steering wheel.

The overturning moment is caused by deformation in the contact patch which displaces the normal load laterally away from the wheel centre. This moment is most significant under large tire deflections, as seen in aircraft tires [1].

A tire handling model makes use of simple tire characteristics, extensive empirical data, or a combination of both to determine the forces in a tire. Many models of both types have been developed.

Two common parameter-based tire models are the UA-Tire Model, and the Fiala tire model. The UA-Tire Model was originally developed at the University of Arizona by

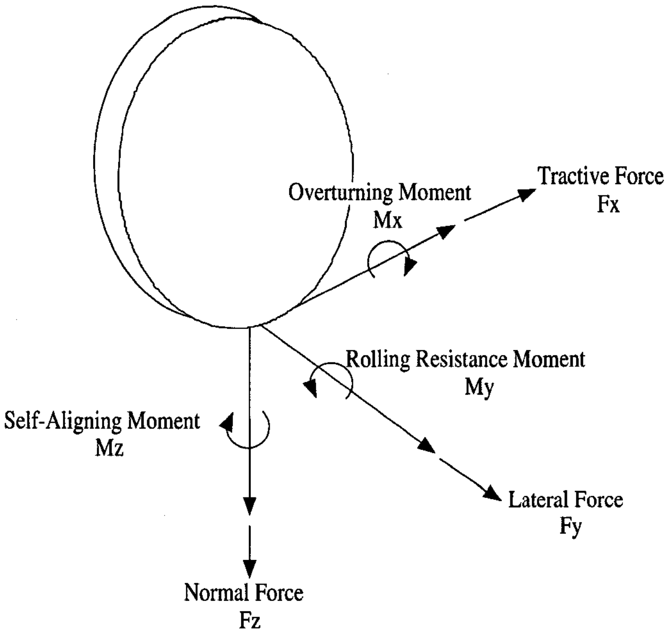
Overturning Moment
Mx
Tractive Force
Fx
Rolling Resistance Moment
My
Self-Aligning Moment
Mz
Lateral Force
Fy
Normal Force
Fz

Figure 3.13: *Tire forces - Contact patch forces.* The theoretical forces and moments acting on a tire act the contact patch are shown [31].

Dr. P.E. Nikravesh and Dr. G. Gim [9]. The model requires the following eleven input parameters, some of which are derived from tire geometry, and some of which must come from physical tire tests [20]:

- Unloaded tire radius
- Vertical stiffness
- Vertical damping ratio
- Rolling resistance parameter
- Longitudinal slip stiffness
- Cornering stiffness
- Camber stiffness
- Minimum friction coefficient
- Maximum friction coefficient
- Longitudinal relaxation length
- Lateral relaxation length

With the eleven tire parameters, the model is fully characterized, and for each calculation step the model requires the following inputs from the vehicle model [20]:

- Tire deflection and tire deflection rate
- Longitudinal tire slip
- Sideslip (slip angle)
- Camber angle

The equations in the model output the three contact patch forces, as well as the rolling resistance moment, M_y, and the self-aligning moment, M_z. The overturning moment is neglected.

Similar to the UA-Tire Model, the Fiala tire model requires nine parameters to calculate tire forces [20]:

- Unloaded tire radius
- Tire carcass radius
- Vertical stiffness
- Vertical damping ratio
- Longitudinal tire stiffness
- Lateral tire stiffness due to slip angle
- Rolling resistance moment coefficient ($C_r = \frac{M_Y}{F_Z}$)
- Static coefficient of friction
- Dynamic coefficient of friction

And for each calculation the model requires the following inputs from the vehicle model [20]:

- Tire deflection and tire deflection rate
- Longitudinal tire slip
- Sideslip (slip angle)

Some disadvantages of the Fiala model compared to the UA-Tire Model are that camber effects are ignored, and the model cannot represent combined driving and cornering, or combined braking and cornering.

Perhaps the most well known tire handling model is that based on the publications of Dr. Hans B. Pacejka et al. at the Delft University of Technology. The Pacejka '89 and Pacejka '94 tire models are derived from the publications of Dr. Pacejka [24]. The MF-Tire model, or Magic Formula model, is also based on the formulations of Dr. Pacejka, and is continuously developed and promoted by the Delft Vehicle Research Centre (DVR) at Delft University. There are still more models available which are variations on the same equations, all with similar behaviour. The general function of the Pacejka equations is to curve-fit empirical tire test data. With test data for a particular tire, coefficients can be derived which allow the model to accurately represent the quasi steady-state driving/braking, cornering, and combined-slip behaviour of the tire.

The basis of the Pacejka models is what is known as the Magic Formula (Equation 3.5.1) [24].

$$\begin{aligned} y(x) &= D \cdot \sin(C \cdot \arctan[Bx - E[Bx - \arctan(Bx)]]) \\ Y(x) &= y(x) + S_v \\ x &= X + S_h \end{aligned} \tag{3.5.1}$$

The result, $Y(X)$ can represent side (lateral) force, self-aligning torque, or brake force, depending on the choices of the variables B, C, D, and E. The independent variable, X, is taken as slip angle (α), or longitudinal slip (κ). The Pacejka models neglect both overturning moment and rolling resistance moment. The meanings of the four coefficients are as follows:

- B = stiffness factor
- C = shape factor
- D = peak factor (represents the peak value of the curve)
- E = curvature factor

- S_h = horizontal shift
- S_v = vertical shift

The coefficient D represents the peak value of the curve. The product BCD produces the slope (or stiffness) of the curve in the area just about the origin. The curvature factor E allows a stretch or compression of the curve without affecting either the peak magnitude or the slope. The shape factor (C), drastically alters the shape of the curve. The value of C is chosen depending on whether $Y(X)$ represents side force, brake force, or self-aligning moment. The shift coefficients S_h and S_v are used to apply the curve translations which result from camber, rolling resistance, conicity, and ply-steer effects. Each coefficient is associated with an equation which changes depending on the intended meaning of $Y(X)$.

The equations to solve for the coefficients B, C, D, and E are functions of vertical load (F_Z), camber angle (γ), and a further series of coefficients. For the Pacejka '89 model, side force calculations require coefficients $a_0 - a_{13}$, brake force calculations require coefficients $b_0 - b_{10}$, and self-aligning moment calculations require coefficients $c_0 - c_{17}$. Each of the 43 coefficients must be obtained from physical test data or known tire parameters, and many of the coefficients have clear physical meanings. The difference between the Pacejka '89, Pacejka '94, and MF-Tire models lie largely in the equations for B, C, D, and E, and the number of a, b, and c coefficients which are required.

Once the initial Magic Formula equations have been applied, the tire model can be extended to simulate combined slip conditions. The combined slip equations are a function of lateral and longitudinal tractive forces (F_Y and F_X), self-aligning moment (M_Z), and the slip speed vector and rolling speed vector of the tire. The total tractive force (longitudinally and laterally) that the model predicts for combined slip conditions will trace out the traction circle for the vehicle. Due to the combined slip capabilities and proven correlation with vehicle measurements, the Magic Formula based tire models are the most popular choice for vehicle handling simulations.

Chapter 4

Forming and Solving Equations of Motion

The basis of any mechanical system analysis is the formulation of equations describing the different bodies in the system and their the kinematical and kinetic relationships. Once the equations defining the behaviour of a system are known, they can be examined in the frequency domain or integrated in the time domain in order to extract the desired information. Furthermore, modern computer packages have made such formulation and analysis easier than ever before.

4.1 Newton's Equations and Eigen Analysis

There are several methods of formulating equations of motion for a system. The most basic is the straightforward application of Newton's second law (Equation 4.1.1).

$$\begin{aligned} \sum \vec{F} &= m\vec{a} \\ \sum \vec{T} &= I\vec{\alpha} \end{aligned} \tag{4.1.1}$$

Newton's second law defines the relationship between forces applied to rigid bodies in space and the resulting motion. Thus, the equations produced are known as the *equations of motion* of the system. Newton's Law is applied to each body or particle in a system separately and the resulting equations are combined to define the system as a whole: $\vec{F}_{1,x} = (m_{1,x})(\vec{a}_{1,x})$, $\vec{F}_{2,x} = (m_{2,x})(\vec{a}_{2,x})$, or in state space form:

$$\begin{Bmatrix} \vec{F}_{1,x} \\ \vec{F}_{2,x} \end{Bmatrix} = \begin{bmatrix} m_1 & 0 \\ 0 & m_2 \end{bmatrix} \begin{Bmatrix} \vec{a}_{1,x} \\ \vec{a}_{2,x} \end{Bmatrix} \tag{4.1.2}$$

The basic method of analysis of a body subjected to a force is to apply Newton's equations, and solve for the resulting acceleration of the body, *i.e* $\vec{a}_i = F_i/m_i$. The instantaneous acceleration can then be integrated to find the time domain response of the body.

The same applies to systems of bodies. Take, for example, a system with two bodies and including a spring (k) and damper (c) attaching them, with external forces (Figure 4.1). The spring and damper produce forces are functions of the state variables (x_1 and x_2):

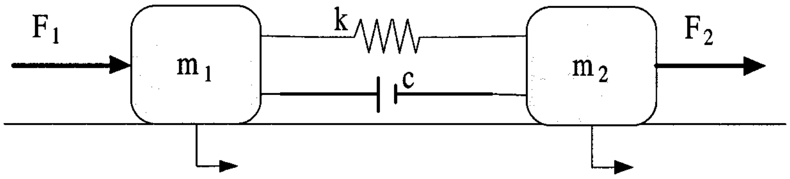

Figure 4.1: *Simple spring / mass / damper system.* A simple system of two bodies with external forces, connected by a spring and damper.

$$\begin{bmatrix} m_1 & 0 \\ 0 & m_2 \end{bmatrix} \begin{Bmatrix} \vec{a}_1 \\ \vec{a}_2 \end{Bmatrix} + \begin{bmatrix} -c & c \\ c & -c \end{bmatrix} \begin{Bmatrix} \vec{v}_1 \\ \vec{v}_2 \end{Bmatrix} + \begin{bmatrix} -k & k \\ k & -k \end{bmatrix} \begin{Bmatrix} \vec{x}_1 \\ \vec{x}_2 \end{Bmatrix} = \begin{Bmatrix} \sum \vec{F}_1 \\ \sum \vec{F}_2 \end{Bmatrix} \tag{4.1.3}$$

Which can be rewritten as:

$$\begin{bmatrix} M \end{bmatrix} \begin{Bmatrix} \vec{a}_1 \\ \vec{a}_2 \end{Bmatrix} + \begin{bmatrix} C \end{bmatrix} \begin{Bmatrix} \vec{v}_1 \\ \vec{v}_2 \end{Bmatrix} + \begin{bmatrix} K \end{bmatrix} \begin{Bmatrix} \vec{x}_1 \\ \vec{x}_2 \end{Bmatrix} = \begin{Bmatrix} \sum \vec{F}_1 \\ \sum \vec{F}_2 \end{Bmatrix} \tag{4.1.4}$$

where:

$[M]$ = mass matrix

$[K]$ = stiffness matrix

$[C]$ = damping matrix

Or:

$$\begin{Bmatrix} \vec{a}_1 \\ \vec{a}_2 \end{Bmatrix} = -\left[M\right]^{-1}\left[C\right]\begin{Bmatrix} \vec{v}_1 \\ \vec{v}_2 \end{Bmatrix} - \left[M\right]^{-1}\left[K\right]\begin{Bmatrix} \vec{x}_1 \\ \vec{x}_2 \end{Bmatrix} + \left[M\right]^{-1}\begin{Bmatrix} \sum \vec{F}_1 \\ \sum \vec{F}_2 \end{Bmatrix} \tag{4.1.5}$$

Equation 4.1.5 can likewise be integrated forward in time to find the time domain response of the system of bodies.

If the mass matrix, $[M]$, the stiffness matrix, $[K]$, and the damping matrix, $[C]$, all consist of only constant components (no terms contain the coordinates themselves) then the system is *linear.* It can be rewritten in first order form as in Equation 4.1.6.

$$\begin{Bmatrix} \vec{v}_1 \\ \vec{v}_2 \\ \vec{a}_1 \\ \vec{a}_2 \end{Bmatrix} = \begin{bmatrix} \left[0\right] & \left[I\right] \\ \left[-M^{-1}K\right] & \left[-M^{-1}C\right] \end{bmatrix}\begin{Bmatrix} \vec{x}_1 \\ \vec{x}_2 \\ \vec{v}_1 \\ \vec{v}_2 \end{Bmatrix} + \begin{bmatrix} \left[0\right] \\ \left[-M^{-1}\right] \end{bmatrix}\begin{Bmatrix} F_1 \\ F_2 \end{Bmatrix} \tag{4.1.6}$$

or

$$\left\{\dot{\vec{x}}\right\} = \left[A\right]\left\{\vec{x}\right\} \tag{4.1.7}$$

where:

$$\vec{x} = \text{state variable vector}$$

$$[A] = \text{system dynamic matrix}$$

If we neglect the forces on the system we can characterize the behaviour of the *unforced* system (Equation 4.1.7) to changes in initial condition. We first assume that the form of the solution for vector $\vec{x}$ will be a sinusoidal response (Equation 4.1.8).

$$\begin{aligned} \vec{x} &= Xe^{st} \\ \dot{\vec{x}} &= sXe^{st} \end{aligned} \tag{4.1.8}$$

By substituting Equations 4.1.8 into the equations of motion, it is possible to solve for the complex time coefficients $s = a + bi$, also known as the *eigenvalues* of the system. The eigenvalues define the response of the linear system. Clearly, from the form of the time domain solution (Equations 4.1.8) a positive real component of s will cause the solution to tend towards infinity with time. Thus, the sign of the real component of s is the indicator of system stability.

The true meaning of the eigenvalues is that they represent the square of the natural frequencies of the system (Equation 4.1.9).

$$s = \omega^2 \tag{4.1.9}$$

where:

ω = natural frequency

The natural, or *resonant*, frequencies of a system are those at which an exciting force would be able to cause a maximum resulting motion in the system. Knowing the collective eigenvalues of a system allows the investigator to perform a *frequency domain* vehicle analysis. The resulting knowledge of the frequency required to excite each component allows tuning for comfort under common road input frequencies and separation of rigid body motions which should not occur in combination.

The drawback of linear system analysis is that it is inherently difficult to obtain a system of linear equations to describe an interesting system. Even for a relatively simple system such as a double pendulum, one must make small-angle assumptions in order to linearize the equations of motion. The linear results and information gathered from the eigen analysis are already only applicable to the small range of motions surrounding the point of linearization. An additional benefit of possessing an accurate linear model of a system is that it opens the system up to the application of linear control theory principles, which are much more deterministic than their nonlinear counterparts.

When modeling is extended from small systems of bodies to large complicated systems such as vehicle suspensions or entire vehicle systems, the task of linearization becomes increasingly difficult. Tires are extremely nonlinear in many of their frequently encountered loading cases. Depending on the region of vehicle behaviour of interest the tires alone may rule out a linear analysis. Consider also the nonlinear effects of large suspension rotations, and other elastomeric components (*e.g. suspension bushings*), and it is obvious that many aspects of vehicle behaviour cannot be captured in a linear analysis. When the only useful model is a nonlinear representation, the investigator must rely on time-domain simulation results to extract information about the system.

4.2 Vehicle Dynamics and Linear Models

The simplest vehicle models are those intended to represent and investigate one particular type of behaviour. Efficient modeling calls for the inclusion of only as much detail as necessary to accurately model the effects of interest. Furthermore, the previous state of computers made it impractical and futile to model a vehicle with nonlinearities and *extra* details, which are present in some modern vehicle models. Thus, many linear vehicle models have been developed which can effectively, and concisely, represent an aspect of vehicle behaviour.

4.2.1 The Bicycle Model

The basic handling dynamics of a vehicle during cornering are often analyzed using the linear *bicycle model* (Figure 4.2) [23][8][25]. The model is named as such because it neglects the width of the car by assuming that the inside and outside tires have the same forward speed.

The vehicle is represented by the sprung mass or chassis (m), the track width (t), the distance from the CG to the front axle (a), the distance from the CG to the rear axle (b), the lateral force on the front tires (F_f), and the lateral force on the rear tires (F_r). The velocity of the centre of mass of the vehicle is represented in a *local* reference frame as $\vec{V} = u\hat{\imath} + v\hat{\jmath}$ and $\vec{\omega} = r\hat{k}$, where r is the *yaw rate* of the vehicle. Furthermore it is assumed that the forward speed of the vehicle is under the control of the driver and is thus constant (i.e. $\dot{u} = 0$). The two degrees of freedom of the bicycle model are then the yaw and lateral motions.

We can apply Newton's 2nd law (4.1.1) to form equations of motion:

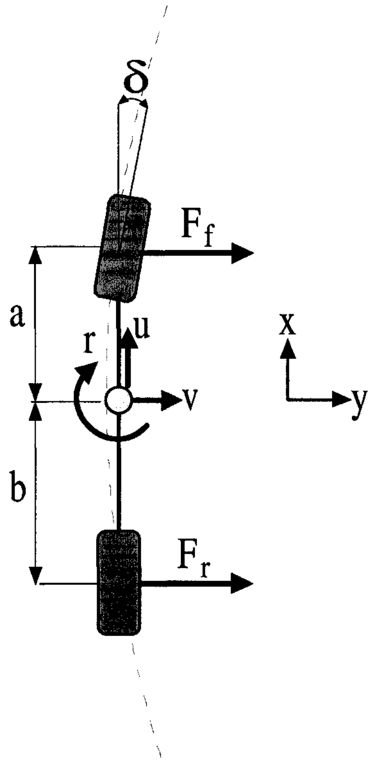

Figure 4.2: *Bicycle model vehicle representation.* The bicycle model can be used to model vehicles for the purpose of handling analysis. The vehicle is approximated as having no width, and thus the two front tires and two rear tires are simply represented as a single front and rear tire, at distances from the *CG* of a, and b, respectively. The forward speed is assumed constant (u) and lateral accelerations are a consequence of lateral forces F_f and F_r.

$$\begin{aligned}\sum \vec{F} &= m \cdot \frac{d\vec{V}}{dt} \\ \sum \vec{F} &= m \cdot (\dot{\vec{V}} + \vec{\omega} \times \vec{V}) \\ \sum \vec{F} &= m \cdot [\dot{u}\hat{\imath} + \dot{v}\hat{\jmath} + r\hat{k} \times (u\hat{\imath} + v\hat{\jmath}) \\ \sum \vec{F} &= m \cdot [(\dot{u} - r \cdot v)\hat{\imath} + (\dot{v} + r \cdot u)\hat{\jmath}]\end{aligned} \tag{4.2.1}$$

Lateral acceleration only: $F_f + F_r = m \cdot (\dot{v} + r \cdot u)$

$$\begin{aligned}\sum \vec{M} &= I \cdot \frac{d\vec{\omega}}{dt} \\ a \cdot F_f + b \cdot F_r &= I \cdot \dot{r}\end{aligned} \tag{4.2.2}$$

In order to complete the formulation of the model, assumptions must be made about the lateral tire forces F_f and F_r. In reality of course these are functions of normal load, temperature, tire pressure, slip angle, etc. For the purposes of the bicycle model it is assumed that the tires lie in the linear range of the *tire force versus slip angle* plot (Figure 3.7). The normal load on all tires is also assumed to be the same at the inner and outer tires, also a necessary assumption to retain linearity. In the initial, linear, region of the tire lateral force versus slip angle curve, the tire forces are directly proportional to the slip angle by Equation 4.2.3.

$$F_{lateral} = C_\alpha \cdot \alpha \tag{4.2.3}$$

where:

$$\alpha = \text{Tire slip angle}$$
$$C_\alpha = \text{Tire cornering stiffness}$$

Thus, the tire forces are linear functions of the tire slip angles (α_f and α_r).

The tire slip angles themselves are found to be functions of u, r, a, b, and *steer angle*, δ (Equations 4.2.4) [23].

$$\begin{aligned} F_f &= C_f \cdot \alpha_f \\ &= C_f \cdot \left(\frac{v + r \cdot u}{u} - \delta \right) \\ F_r &= C_r \cdot \alpha_f \\ &= C_r \cdot \left(\frac{v - r \cdot b}{u} \right) \end{aligned} \tag{4.2.4}$$

The system of equations defining the entire bicycle model can be written in matrix form (Equation 4.2.5).

$$\begin{bmatrix} m & 0 \\ 0 & I \end{bmatrix} \begin{Bmatrix} \dot{v} \\ \dot{r} \end{Bmatrix} + \begin{bmatrix} \frac{C_f + C_r}{u} & \frac{a \cdot C_f - b \cdot C_r}{u} + m \cdot u \\ \frac{a \cdot C_f - b \cdot C_r}{u} & \frac{a^2 \cdot C_f + b^2 \cdot C_r}{u} \end{bmatrix} \begin{Bmatrix} v \\ r \end{Bmatrix} = \delta \begin{Bmatrix} C_f \\ a \cdot C_f \end{Bmatrix} \tag{4.2.5}$$

The bicycle model is useful for investigating the effects of different steer inputs on a vehicle. For example, at different vehicle forward speeds the steer angle could attempt to drive the car through a slalom, and the maximum *body slip angle* ($\beta = \frac{v}{u}$) observed. By examining the $\frac{\beta}{\delta}$ ratio one can tell whether the vehicle is *oversteering, understeering, or neutral steering* during cornering. However one of the basic assumptions of the bicycle model is that the tire normal load is the same at the inner and outer tires. This implies that lateral weight transfer effects, which can drastically affect tire forces during cornering, are completely ignored.

4.2.2 Quarter-Car and Bounce/Pitch Models

The study of *ride* characteristics of a vehicle is concerned with the comfort of the passenger. Ride is fundamentally different from handling; the vertical tire forces and vertical suspension motions are of utmost importance as opposed to the lateral forces of interest for handling. The vertical *bump* accelerations experienced by the driver are studied rather than vehicle lateral accelerations.

The simplest model used to study ride is the *quarter-car model* (Figure 3.11). As would be suggested by the title, the quarter-car model studies one corner of the vehicle: one wheel and suspension. By simply applying Newton's 2nd equation (Equation (4.1.1)) the equations defining the simple quarter-car model shown in Figure 3.11 can be derived (see Equation 4.2.6). The equations of motion are shown in matrix form in Equation 4.2.7.

$$\begin{gathered}
m_{sprung}\ddot{\vec{z_1}} + c_s(\dot{\vec{z_1}} - \dot{\vec{z_2}}) + k_s(z_1 - z_2) = 0 \\
m_{wheel}\ddot{\vec{z_2}} + c_s(\dot{\vec{z_2}} - \dot{\vec{z_1}}) + k_s(\vec{z_2} - \vec{z_1}) + c_{tire}\dot{\vec{z_2}} + k_{tire}\vec{k_2} = c_{tire}\dot{\vec{z_0}} + k_{tire}\vec{z_0}
\end{gathered} \tag{4.2.6}$$

$$\begin{aligned}
\begin{bmatrix} m_{sprung} & 0 \\ 0 & m_{tire} \end{bmatrix} \begin{Bmatrix} \ddot{\vec{z_1}} \\ \ddot{\vec{z_2}} \end{Bmatrix} + \begin{bmatrix} c_s & -c_s \\ -c_s & c_s + c_{tire} \end{bmatrix} \begin{Bmatrix} \dot{\vec{z_1}} \\ \dot{\vec{z_2}} \end{Bmatrix} + \begin{bmatrix} k_s & -k_s \\ -k_s & k_s + k_{tire} \end{bmatrix} \begin{Bmatrix} z_1 \\ z_2 \end{Bmatrix} \dots \\
= \begin{bmatrix} 0 \\ k_{tire} \end{bmatrix} \vec{z_0} + \begin{bmatrix} 0 \\ c_{tire} \end{bmatrix} \dot{\vec{z_0}}
\end{aligned} \tag{4.2.7}$$

A ride model such as the quarter car model is very useful for studying the dynamics of a vehicle traversing bumps. Depending on the springing properties of the tire and suspension, the *frequency* effects of the road surface and vehicle speed can be investigated. Performing an eigenvector analysis, for instance, may reveal exaggerated sprung mass motion at a certain road input frequency. Such exaggerated motions would be felt by the passengers as large bumps. Knowledge of the frequencies in question allows the designer to take steps to prevent the discomfort from occurring.

When a quarter-car model is expanded to both the front and rear of the vehicle it produces a bounce / pitch model (Figure 4.3). The vehicle is allowed to pitch back and forth in addition to the bounce seen in the quarter-car model. The investigator can then determine which frequency of road excitation will cause bounce, pitching, or a combination thereof. Useful tuning information can be extracted, particularly for the required relative stiffness and damping of the front and rear suspensions.

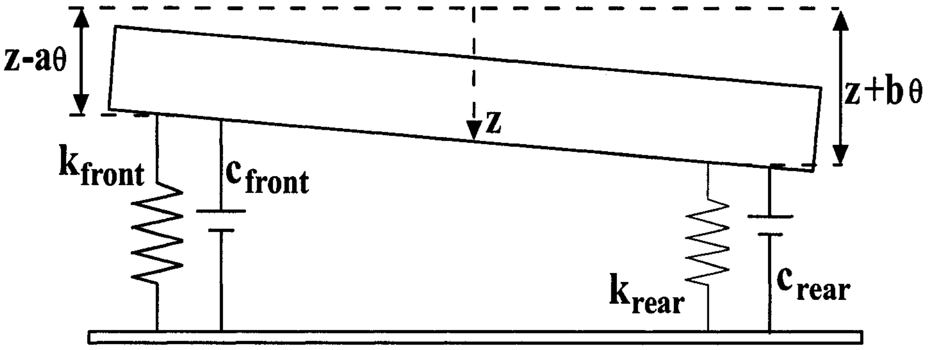

Figure 4.3: *Bounce-pitch model vehicle representation.* When the quarter-car model is extended to include the vehicle pitch angle, the analysis may be useful in determining relative suspension rates to improve ride quality.

4.3 Vehicle Modeling With CarSim

With the current state of computer technology, it is natural that a large portion of vehicle modeling and analysis takes the form of computer simulations. Purpose-written software packages automatically generate equations of motion based on user-defined mechanical systems. Furthermore, said packages are combined with time-domain integrators and post-processing packages to form mechanical analysis software suites. Two such generic software packages are MSC ADAMS and LMS DADS. Either package may be used to analyze any mechanical system the user is able to model. The user must accurately locate all the bodies with accurate mass and inertial properties, as well as all the joints (i.e. constraints) of the correct types at the correct locations.

More recently some software packages have been developed exclusively for use in vehicle simulation work. These packages, such as Mechanical Simulation Corp.'s CarSim, trade-off flexibility for the promise of accuracy and experimental data correlation. By using software with a pre-built and tested vehicle system, the burden of modeling is removed from the investigator, and the focus can be placed on model fine-tuning and designing useful experiments.

4.3.1 Model - General

The vehicle model in CarSim is defined by fully nonlinear equations of motion as derived using first principles. The equations are in the form of a system of ordinary differential equations (ODE's). In CarSim vernacular, the program contains several built-in *solvers*. A *solver* in CarSim represents a complete set of equations of motion defining a particular combination of front and rear suspension types and a trailer (if included). For instance, a truck simulation in CarSim would likely implement a different CarSim *solver* than a passenger car.

Depending on the vehicle setup options the system of equations contains roughly 14 multi-body degrees of freedom. The sprung mass has six degrees of freedom, each wheel has degrees of freedom for vertical motion, wheel spin, and steer, and further degrees of freedom are included for other physical coordinates and general properties of interest. For example, the fully independent suspension CarSim vehicle model is "represented mathematically by 83 ordinary differential equations that describe its kinematical and dynamical behaviour. It is composed of 21 bodies, has 14 multibody degrees of freedom, 30 multibody coordinates, 37 auxiliary coordinates, 14 multibody speeds, 2 auxiliary speeds, and has 57 active forces and 34 active moments" [21]. The vehicle models are solved with steering, throttle, and braking inputs, and riding on complex virtual road surfaces. The desired driving path is defined by a table of $X - Y$ coordinates. Vertical geometry of the driving surface is further specified as Z values as a function of distance along the driving path, and lateral distance from the path. This allows for non-symmetric vertical geometry and obstacles such as ditches and potholes. Friction coefficient, μ, of the road surface is also defined by a 2D table, allowing conditions of varying friction.

4.3.2 Suspension

Each wheel on the vehicle has vertical travel and rolling rotation as degrees of freedom. The front suspension is always modeled as fully independent, while rear suspensions may be independent, twist axle, or solid axle at the option of the user. Each suspension contains full compliance effects in lateral / longitudinal motion and angular motion, and friction (hysteresis) effects in the suspension springs.

All kinematics (camber, toe, etc.), spring stiffnesses, damping, and compliance can be defined by the user through lookup tables / curves, which can be fully nonlinear. For this reason, the suspension type need not be specified beyond "independent", as the solver uses kinematic curves (the consequence of whatever geometry may be present) rather than the geometry itself. The effects of roll and jacking forces are derived from the kinematic curves and the compliance effects, rather than as a consequence of conventional geometric analyses.

4.3.3 Aerodynamics

Aerodynamic effects on the vehicle are included. Three forces and three moments are applied to the sprung mass at a point known as the aerodynamic reference point. Users may define the aerodynamic properties of the vehicle model by inputting six coefficients of drag (as functions of aerodynamic slip angle), vehicle reference length, location of the aerodynamic reference point, and vehicle frontal area. The user may also define the wind amplitude, wind heading, and air density for a given simulation using nonlinear tabular data, as a function of time.

4.3.4 Steering

Complete vehicle steering mechanics are included in the CarSim model. The virtual driver can steer the steering wheel to any angle up to a user-definable maximum angle. The steer angle at the wheels is found by multiplying the steer angle through the steering rack ratio (user-defined tabular data). The actual angle at the wheel/tire is augmented by the angular effects of the compliance in the suspension. The compliance deflection is found as a result of the sum of moments in the suspension about the kingpin. Steering torque at the steering wheel is calculated by multiplying the total moment about the kingpin back through the steering system ratio.

The driver steer angle can be defined as an open-loop function of time in the form of tabular data, or can be controlled by a virtual driver. The virtual driver will always try to follow a user-defined driving path. A level of realism is added using a nominal response time lag, and a *preview time.* Preview time is the delay between when the driver sees an upcoming event, such as a curve in the road, and when the vehicle must react to it. A realistic value is said to be approximately 1.5 seconds[22].

4.3.5 Brakes

For the braking system in CarSim the input pressure (at the brake pedal) is controlled by either an open-loop control or the virtual driver. The pressure is proportioned to each brake by the master cylinder according to user-definable curves, which can be controlled independently for each wheel. Furthermore, the user can define braking torque as a function of pressure for each brake individually, allowing large amounts of flexibility in brake system control.

Dynamics in the hydraulic brake fluid are modeled by a first order transient lag and a constant time delay. Both the “fluid dynamics time constant” and the “transport delay” can be defined for each brake individually.

When the brakes are applied to a spinning wheel, the supplied torque causes the wheel to decelerate. This allows the braking torque to be calculated using Newton's second law. When the wheel locks up, however, the brake no longer does any work. Still, the braking torque does not go to zero, but rather supplies just enough torque to keep the wheel from spinning. These two braking situations represent two unique mathematical cases. Thus, when lockup is detected the solver will switch to a *locked-up* braking model. The brake system is replaced by a torsional spring and damper that winds up the wheel to resist the braking loads at the tire contact patch. The model switch occurs when the wheel reaches a rotation speed equivalent to a low user-defined forward speed, and will stay locked up until the torque in the torsional spring/damper is greater than the supplied braking torque.

4.3.6 Powertrain

CarSim uses a detailed powertrain model that includes engine torque output and fuel consumption, and detailed transmission effects. Torque and fuel consumption are both calculated as functions of engine RPM and throttle angle using user-defined tabular data. Torque is transmitted to either an automatic or a manual transmission that include the effects of the torque-converter or clutch, as well as efficiency and inertia that can be specified for each gear. Torque is transmitted to the driven wheels through the differential (final drive) ratio or alternatively, through an all-wheel drive system with user-defined front to rear torque-split.

As with steering and braking, the throttle, shifting, and clutch can be controlled by the end user as open-loop functions of time. Alternatively the clutch (if applicable) and shift timing can be controlled by a shift schedule, and the throttle controlled by the virtual driver model.

4.3.7 Tires

CarSim allows the user to model tire forces using a default internal model (with or without nonlinear camber and overturning moment effects), the Pacejka 5.2 Magic Formula model, or any external model that can be programmed in C code or Simulink.

The CarSim Internal Tire Model uses nonlinear tabular data of longitudinal force, lateral force, aligning moment, and overturning moment as functions of longitudinal slip, lateral slip angle, load, and camber angle. The required data represents typical quantities that are obtainable during experimental tire testing. The vertical load in the tire is found by treating the tire as a linear spring in the vertical direction, and so a stiffness coefficient must be supplied.

Tire models such as the Magic Formula model represent methods of curve-fitting tire test data. Thus, it is presumed that by inputting tire test data directly into CarSim (which is designed to interpret and use it directly) the results should compare well with those found using equation-based tire models.

4.3.8 Solver Method

The equations of motion of the CarSim vehicle system are in the form of a set of ODE's. The CarSim solver integrates the differential equations using a second-order implicit Runge-Kutta algorithm known as RK2. Second-order Runge-Kutta is best understood as a refinement of Euler's Method. Given the present value of the dependent variable $y(t)$, Euler's method calculates the derivative $k_1 = \left.\frac{dy}{dt}\right|_{t_0}$, and estimates the next value of $y(t)$ to be $y_{t+h} = y_t + h \cdot k_1$. It is therefore considered a linear one-step method. It is simple to implement, but accuracy is low, and the time step h must be made very small in order to increase accuracy.

Runge-Kutta integration methods sacrifice the linearity of Euler's method, but retain the one-step format. Other integration methods exist which retain linearity but move into a multi-step format. With second order Runge-Kutta (RK2), a second estimate of the derivative is used to increase the accuracy. Knowing y_t the derivative at the current time is found as $k_1 = \frac{dy}{dt}\Big|_t$. The derivative k_1 is used to make an initial estimate for y_{t+h} called y^*_{t+h} and the derivative at $t+h$ is estimated using y^*_{t+h} as $k_2 = \frac{dy}{dt}\Big|_{t+h}$. The new value for y, called $y^{\bar{*}}$, is found to be $y^{\bar{*}}_{t+h} = y_t + h\frac{(k_1+k_2)}{2}$. Thus, the average of the two estimated derivatives was used to estimate the new value of y. The RK2 method is summarized as Equation 4.3.1 and provides better results than the simplest form of Euler's method.

$$\begin{aligned} k_1 &= \frac{dy}{dt}\bigg|_t^y \cdot h \\ k_2 &= \frac{dy}{dt}\bigg|_{t+h}^{y+k_1\cdot h} \cdot h \\ y_{t+h} &= y + \left(\frac{k_1+k_2}{2}\right)\cdot h \end{aligned} \tag{4.3.1}$$

Because Runge-Kutta methods are future-looking and do not rely on information from previous time-steps, it is easy to adapt the size of the time-step to increase or decrease accuracy as required. However, CarSim implements a fixed time-step in order to facilitate co-simulation abilities with external software packages, compatibility with experimentally measured tabular data, and ability to match constant step size test data. As a consequence, the solver in CarSim has no internal error-checking, and the end user must be cautious. It is recommended that simulations are carried out at several time-steps to verify the insensitivity of the model to further time-step refinement[22].

Chapter 5

Braking Dynamics

When a vehicle decelerates due to braking forces, normal load is transferred off the rear tires, onto the front. The differences in tire normal load create differences in peak braking force capability. In order to design the braking system to utilize each tire in a manner suiting its braking capability, it is necessary to analyze the dynamics of a braking vehicle.

5.1 Braking Stability

The differences in vehicle behaviour when locking either the front or rear axle first during braking are dramatic, and may singly determine whether a vehicle stops safely or loses control. Thus, the main concern in braking force analysis and design has been whether the distribution of braking loads will cause front or rear axle lockup.

In order to investigate the effects of different lockup cases, a simple bicycle model can be used. During straight line driving and braking, tire loads theoretically exist only in the longitudinal direction. In reality, small lateral disturbances will exist during straight line braking, due to small steer angles, non-uniform road surfaces, and aerodynamic loads. The result is that even straight-line driven vehicles are required to supply lateral traction at the tires in order to remain moving straight.

The situation where the front tires of the vehicle lock up is represented in Figure 5.1. Subject to a yaw disturbance, the heading of the vehicle has rotated slightly, while the resultant path of vehicle travel is still directly forward, in the original direction. The

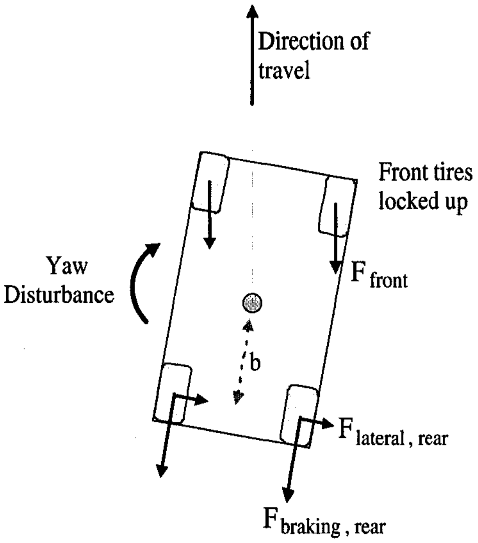

Figure 5.1: *Free body diagram of braking vehicle with front tires locked up.* On a vehicle subject to a yaw disturbance, with the front tires locked up, the rear tire lateral forces will act to reduce the yaw disturbance.

locked up front tires only create forces in a direction opposite the direction of motion. These forces create only a small yawing moment about the *CG*. The rear tires, which have not locked up, still generate significant lateral forces, perpendicular to the rear wheels. These forces act in a direction to oppose the yaw disturbance, and will restore the vehicle to the original heading.

The situation where the rear tires lock up first is represented in Figure 5.2. Subject to the same yaw disturbance, the vehicle is rotated slightly from the absolute direction of travel. The locked up rear tires generate forces only in a direction opposite the direction of vehicle motion. These forces create only a small yawing moment about the vehicle *CG*. The front tires, which remain rolling, generate lateral forces perpendicular to the wheels. The lateral forces at the front tires will create a yaw moment that *increases* the yaw disturbance. Thus, the vehicle will most likely spin out of control.

The net effect is that if the rear tires lock up first, the front lateral forces alone produce a vehicle that is unstable in yaw. The tire forces then tend to increase the effects of the disturbance and cause the vehicle to lose control. Conversely, the rear lateral forces acting

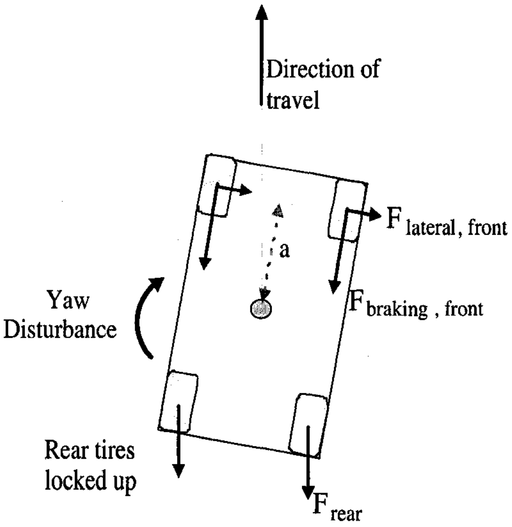

Figure 5.2: *Free body diagram of braking vehicle with rear tires locked up.* On a vehicle subject to a yaw disturbance, with the rear tires locked up, the front tire lateral forces will act to increase the yaw disturbance. Thus, the vehicle will be unstable.

alone produce a vehicle stable in yaw that tends to create yaw moments to reduce the disturbance. The phenomena itself is akin to that seen in caster wheels. If the caster wheel lies forward of its pivot it will always swing around to trail the pivot pin. A caster wheel lying ahead of its pivot resembles an unstable vehicle with its rear tires locked.

5.2 Static Vehicle Properties

The location of the *CG* is rarely equidistant between the front and rear axle on production vehicles. For that reason the static axle load on the front and rear tires can vary drastically. The ratio of static rear axle load to total vehicle load, Ψ (Equation 5.2.1), can commonly be as low as 35 – 40%, leaving 60 – 65% of the weight on the front tires (Equation 5.2.2).

$$\Psi = \frac{F_{zR,static}}{W} \tag{5.2.1}$$

where:

$F_{zR,static}$ = static rear axle load

W = vehicle weight

$$1 - \Psi = \frac{F_{zF,static}}{W} \tag{5.2.2}$$

where:

$$F_{zF,static} = \text{static front axle load}$$

By applying a moment balance about the front axle (Equation 5.2.3) the distances between the *CG* and the front axle (Equation 5.2.4), and between the *CG* and rear axle (Equation 5.2.5) can be solved.

$$W \cdot a = F_{zR,static} L \tag{5.2.3}$$

where:

$$L = \text{wheelbase}$$

$$a = \frac{F_{zR,static} L}{W} = \Psi L \tag{5.2.4}$$

$$b = (1 - \Psi) L \tag{5.2.5}$$

5.3 Dynamics and Load Transfer

When the vehicle undergoes acceleration, either positive or negative, the loads on the individual axles change. The weight transfer is a function of the *CG* height, the length of the wheelbase, and the level of acceleration. The dynamic front and rear axle loads determine the level of braking force generation possible at each axle. Equation 5.3.1 defines the dynamic axle loads in terms of vehicle geometry and deceleration a in g's.

$$\begin{aligned} F_{zF,dyn} &= F_{zF,static} + \frac{h}{L}(Wa) \\ F_{zR,dyn} &= F_{zR,static} - \frac{h}{L}(Wa) \end{aligned} \tag{5.3.1}$$

where:

$h = CG$ height

$a =$ longitudinal deceleration

By defining a dimensionless variable χ (Equation 5.3.2) the dynamic axle loads can be rewritten as in Equation 5.3.3 in terms of Ψ and χ.

$$\chi = \frac{h}{L} \tag{5.3.2}$$

$$\begin{aligned} F_{zF,dyn} &= (1 - \Psi + \chi a)W \\ F_{zR,dyn} &= (\Psi - \chi a)W \end{aligned} \tag{5.3.3}$$

Clearly the total normal load during acceleration does not change, but rather is redistributed between the tires. The transferred load is given by the term χaW, and from Equation 5.3.1 the loads are linear functions of acceleration, a.

5.4 Braking Forces

Recall from Section 2.1 that given the state of the dynamic normal load on an axle i, $F_{zi,dyn}$, and the actual level of braking force created, F_{xi}, the coefficient relating them is the *traction coefficient* (Equation 5.4.1).

$$\mu_{Ti} = \frac{F_{xi}}{F_{zi,dyn}} \tag{5.4.1}$$

Given the traction coefficient, dynamic braking forces can be calculated by multiplying the dynamic axle loads by the traction coefficient (Equation 5.4.2). The braking load at either axle is a function of the geometric properties, the deceleration level, and the traction coefficient.

$$\begin{aligned} F_{xF} &= F_{zF,dyn} \cdot \mu_{front} = (1 - \Psi + \chi a)W\mu_{front} \\ F_{xR} &= F_{zR,dyn} \cdot \mu_{rear} = (\Psi - \chi a)W\mu_{rear} \end{aligned} \tag{5.4.2}$$

As the braking forces applied are increased the deceleration a will also increase, thus increasing the dynamic load transfer. Adding Equations 5.4.2 together yields Equation 5.4.3.

$$\begin{aligned} F_{X,total} &= F_{XF} + F_{XR} \\ &= (1 - \Psi + \chi a) W \mu_{front} + (\Psi - \chi a) W \mu_{rear} \\ &= F_{ZF,dyn} \cdot \mu_{front} + F_{ZR,dyn} \cdot \mu_{rear} \end{aligned} \tag{5.4.3}$$

As both front and rear braking forces are increased, there will be a net increase in the traction utilization at each axle, until the traction coefficient of one or both axles equals the available tire-road friction. When either μ_{front} or μ_{rear} equals the tire-road friction coefficient, $\mu_{friction F}$ or $\mu_{friction R}$, respectively, the axle will lock up.

As braking increases both the front and rear traction coefficients increase until lockup occurs. If either front or rear axle reaches the limit of the friction coefficient first, that axle is said to be *overbraked.* The ideal, or optimum, braking occurs when neither the front or rear axle is overbraked, and thus both front and rear traction coefficients are equal. A braking force balance on the entire vehicle is shown in Equation 5.4.4:

$$\begin{aligned} \sum F_X &= ma \\ \sum F_X &= W(a\ [g]) \\ \frac{F_{XF}}{W} + \frac{F_{XR}}{W} &= a\ [g] \\ \frac{\mu_{front} F_{ZF,dyn}}{W} + \frac{\mu_{rear} F_{ZR,dyn}}{W} &= a\ [g] \\ \mu_{front} \frac{F_{ZF,static} + \frac{h}{L}(Wa)}{W} + \mu_{rear} \frac{F_{ZR,static} - \frac{h}{L}(Wa)}{W} &= a\ [g] \end{aligned} \tag{5.4.4}$$

It can be seen that by substituting the optimal condition of $\mu_{front} = \mu_{rear}$ into the above force balance equation (Equation 5.4.4) the optimal condition (Equation 5.4.5) is the solution.

$$\mu_{front} = \mu_{rear} = a\ [g] \tag{5.4.5}$$

To calculate the optimal braking forces for the front or rear brakes, the deceleration a only need be substituted into Equation 5.4.2 in place of the traction coefficients. The resulting optimal braking forces are given in Equation 5.4.6 and Equation 5.4.7

$$F_{xF,opt} = (1 - \Psi + \chi a)aW \tag{5.4.6}$$

$$F_{xR,opt} = (\Psi - \chi a)aW \tag{5.4.7}$$

The parametric Equations 5.4.6 and 5.4.7 can be plotted for increasing deceleration a to reveal the optimal brake force balance between front and rear axles (Figure 5.3). If the brakes were to be optimally proportioned between front and rear, the brake force would follow this curve as the brakes were progressively applied. If the actual proportioning lied on the upper/left of this curve, the front axle would be overbraked and the front brakes would lock up first as braking increased. Likewise, a proportioning curve on the lower/right of the optimal curve indicates that the rear brakes would lock up first.

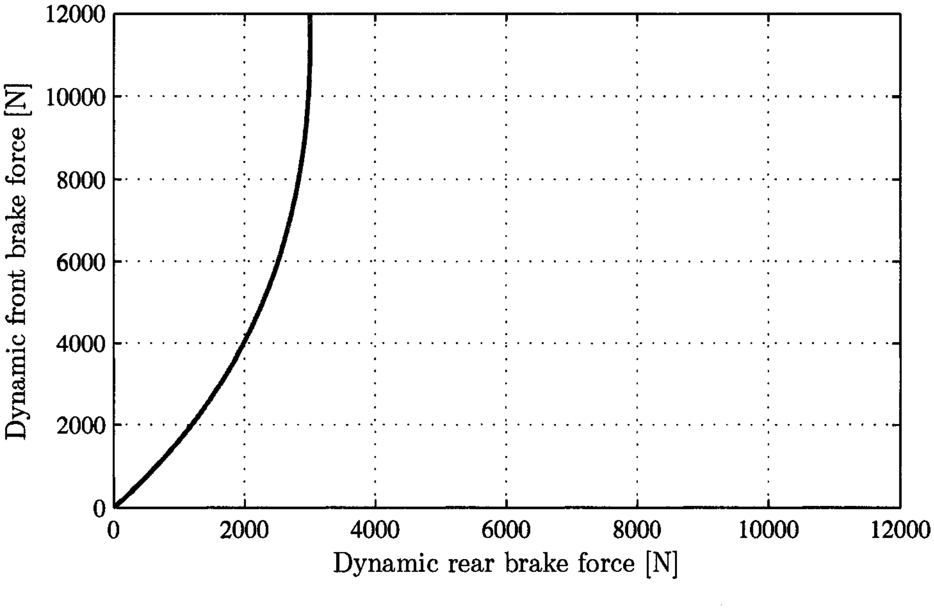

Figure 5.3: *Optimal braking force curve.* By setting the traction utilization at the front axle equal to that at the rear axle, it is possible to plot the braking force optimal curve. If the vehicle was braked following the front:rear ratio of the curve, all tires would lock simultaneously at the limits of traction. (h = 0.542 m, L = 2.690 m, W = 14980 N, $F_{zR,static}$ = 5644.8 N).

If the optimal braking force equations are divided by vehicle weight, the result is *weight normalized* dynamic braking forces (Equation 5.4.8).

$$\begin{aligned} \frac{F_{xF}}{W}|_{opt} &= (1 - \Psi + \chi a)a \\ \frac{F_{xR}}{W}|_{opt} &= (\Psi - \chi a)a \end{aligned} \tag{5.4.8}$$

Plotting the normalized dynamic brake forces serves to scale the axes in a useful way. Lines of constant deceleration form 45° angles. The reason for this is clear from a force balance on the vehicle (Equation 5.4.9). In terms of the weight normalized braking force $\frac{F_X}{W}$, the equation forms a straight line between intercepts equal to the deceleration in $g's$ (Figure 5.4). Following the normalized dynamic brake force plot as braking forces increase, it is easy to observe the deceleration level of the vehicle.

$$\begin{aligned} \sum F_X &= ma \\ \sum \frac{F_X}{W} &= a \;\; [g] \\ \frac{F_{xF}}{W} + \frac{F_{xR}}{W} &= a \\ &\text{Straight line equation:} \\ \frac{F_{xF}}{W} &= a - \frac{F_{xR}}{W} \end{aligned} \tag{5.4.9}$$

The parametric equations for the optimal braking forces can be rearranged to eliminate the a term. The resulting parabola equation (Equation 5.4.10) describes a curve through all longitudinal accelerations (positive and negative) at which the front and rear tires lock up at the same time (Figure 5.5).

$$\frac{F_{xR}}{W}|_{opt} = \sqrt{\frac{(1-\Psi)^2}{4\chi^2} + \left(\frac{1}{\chi}\right)\left(\frac{F_{xF}}{W}\right)} - \frac{1-\Psi}{2\chi} - \frac{F_{xF}}{W} \tag{5.4.10}$$

5.5 Lines of Constant Friction Coefficient

From Figure 5.5 it can be seen that at extreme decelerations the weight transfer to the front tires increases until the point where there is no load on the rear tires. At this point the braking force on the rear axle is zero regardless of tire-road friction coefficient. Likewise,

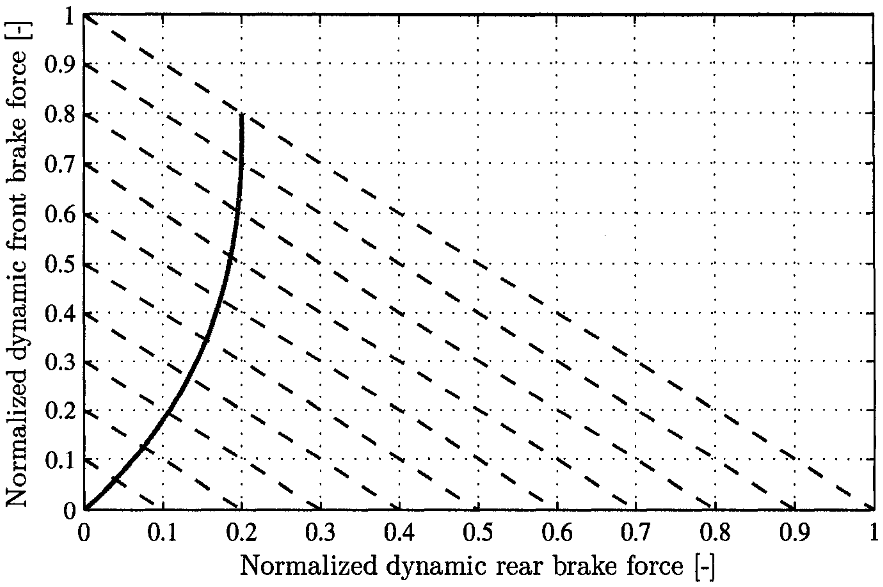

Figure 5.4: *Normalized optimal brake force parabola.* The weight-normalized front axle braking force is plotted against weight-normalized rear axle braking force, for the optimal case where $\mu_{front} = \mu_{rear} = a$. The dashed lines are lines of constant vehicle deceleration ($h = 0.542\ m$, $L = 2.690\ m$, $W = 14980\ N$, $F_{zR,static} = 5644.8\ N$).

during extreme accelerations it can be seen the front axle tractive force is zero regardless of tire-road friction coefficient.

Each point on the optimal curve implies that $\mu_{{friction}^F} = \mu_{{friction}^R} = \mu_{front} = \mu_{rear} = a$, and at each zero point the force is zero for any μ. The result is that straight lines joining the zero-force points to any acceleration level on the optimum curve represent lines of constant friction coefficient, with $\mu_{Ti} = a$.

The straight lines of constant friction coefficient are solved by substituting Equations 5.4.9 into Equations 5.4.2 to eliminate the acceleration term, and substituting in the desired coefficient of friction. For the front axle, substituting $\frac{F_{xF}}{W} + \frac{F_{xR}}{W} = a\ into\ \frac{F_{xF}}{W} = (1 - \Psi + \chi a)\mu_{front}$ yields Equation 5.5.1. For the rear axle, substituting $\frac{F_{xF}}{W} + \frac{F_{xR}}{W} = a\ into\ (\Psi - \chi a)\mu_{rear}$ yields Equation 5.5.2.

$$\frac{F_{xF}}{W} = \frac{\left(1 - \Psi + \chi\left(\frac{F_{xR}}{W}\right)\right)\mu_{front}}{1 - \chi * \mu_{front}} \tag{5.5.1}$$

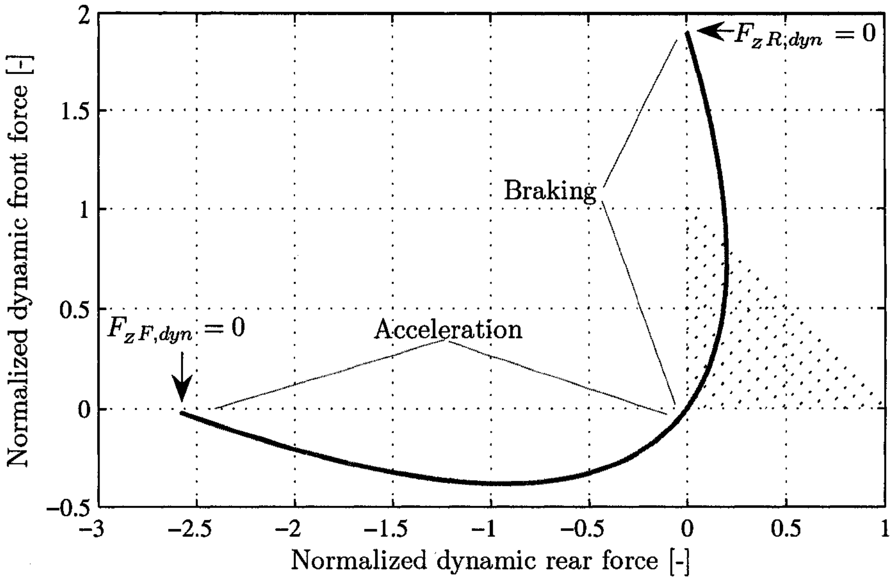

Figure 5.5: *Normalized optimal brake forces showing acceleration and deceleration region.* If the optimal braking parabola is extended throughout the ±a range, it shows the full range of load transfer effects. At extreme decelerations there is no weight on the rear axle, and it will lock up regardless of tire-road friction coefficient; likewise for the front axle during extreme accelerations ($h = 0.542\ m$, $L = 2.690\ m$, $W = 14980\ N$, $F_{zR,static} = 5644.8\ N$).

$$\frac{F_{xR}}{W} = \frac{\left(\Psi - \chi\left(\frac{F_{xF}}{W}\right)\right)\mu_{rear}}{1 + \chi\mu_{rear}} \tag{5.5.2}$$

The lines of constant friction coefficient (Figure 5.6) are extremely useful in braking dynamics analysis. Because the brakes actually installed on a conventional vehicle cannot straddle the optimum curve, the actual braking forces lie elsewhere on the $F_{xF} vs. F_{xR}$ plot. In the braking region the constant friction coefficient lines form a boundary at which lockup will occur. If the tire-road coefficient of friction is 0.5, then lockup will occur when the braking forces cross either the optimal point or either constant $\mu_{Ti} = 0.5$ line (Figure 5.7).

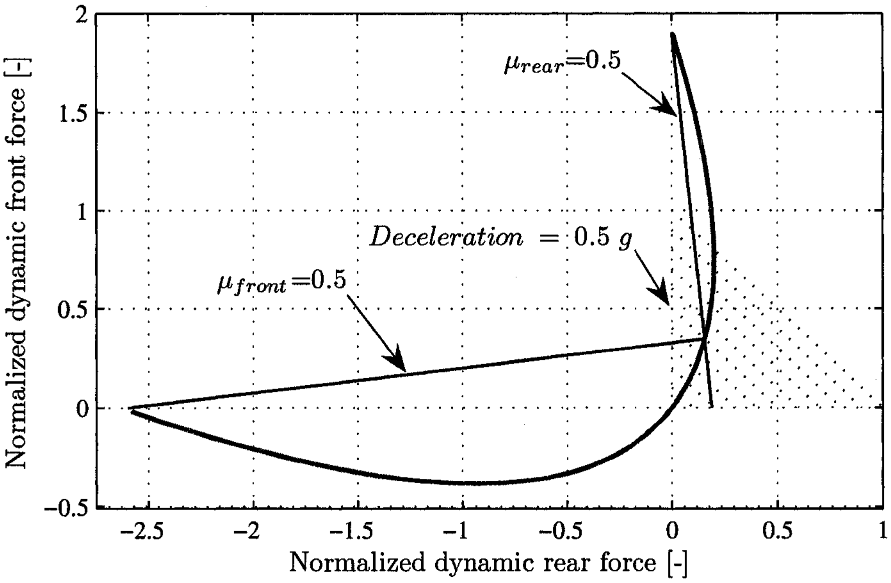

Figure 5.6: *Normalized optimal brake force parabola with lines of constant friction coefficient.* By extending lines from the extreme ends of the parabola to where the 0.5 g constant deceleration line meets the parabola, lines of constant friction coefficient of 0.5 can be created ($h = 0.542\ m$, $L = 2.690\ m$, $W = 14980\ N$, $F_{zR,static} = 5644.8\ N$).

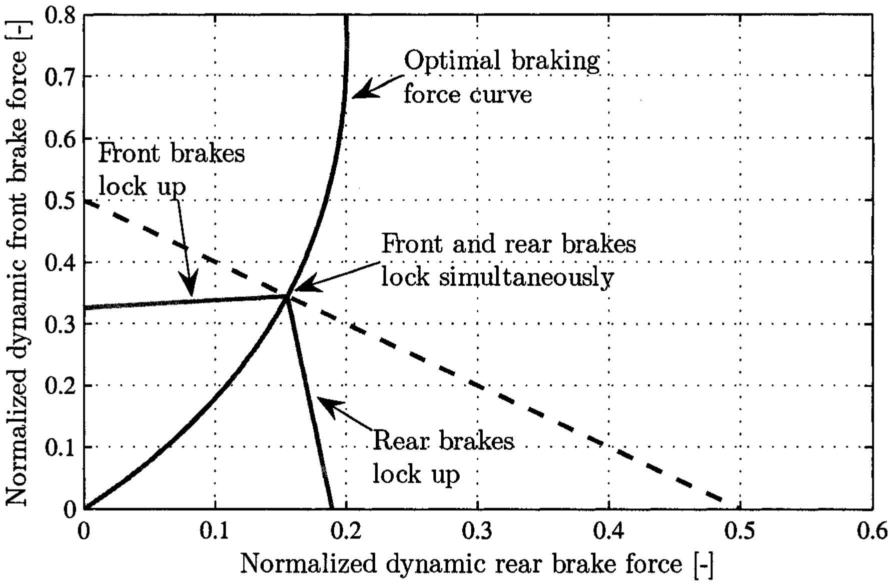

Figure 5.7: *Normalized optimal brake force parabola with constant friction lines.* Weight-normalized front axle braking force is plotted against weight-normalized rear axle braking force, for the condition of $\mu_{friction} = 0.5$. The line of $0.5g$ deceleration is highlighted, as well as the two $\mu_{Ti} = 0.5$ lines of constant coefficient of friction, $\mu_{front} = 0.5$ (labeled *front brakes lock up*) and $\mu_{rear} = 0.5$ (labeled *rear brakes lock up*). Vehicle parameters are ($h = 0.542\,m$, $L = 2.690\,m$, $W = 14980\,N$, $F_{zR,static} = 5644.8\,N$).

5.6 Static Brake Proportioning

The installed brake system on any actual vehicle has a built in front-to-rear brake proportioning system, such that the front and rear do not receive equal braking force. Figure 5.8 and Figure 5.9 each show an example constant *brake proportioning* line, as it lies on the normalized brake force plot. The brake proportioning, Φ, is defined as the percentage of the total braking which is applied to the rear brakes (Equation 5.6.1). For Figure 5.8 and Figure 5.9 the limit of tire-road friction is assumed to be $\mu_{friction} = 0.8$.

$$\Phi = \frac{F_{xR}}{F_{xR} + F_{xF}} \tag{5.6.1}$$

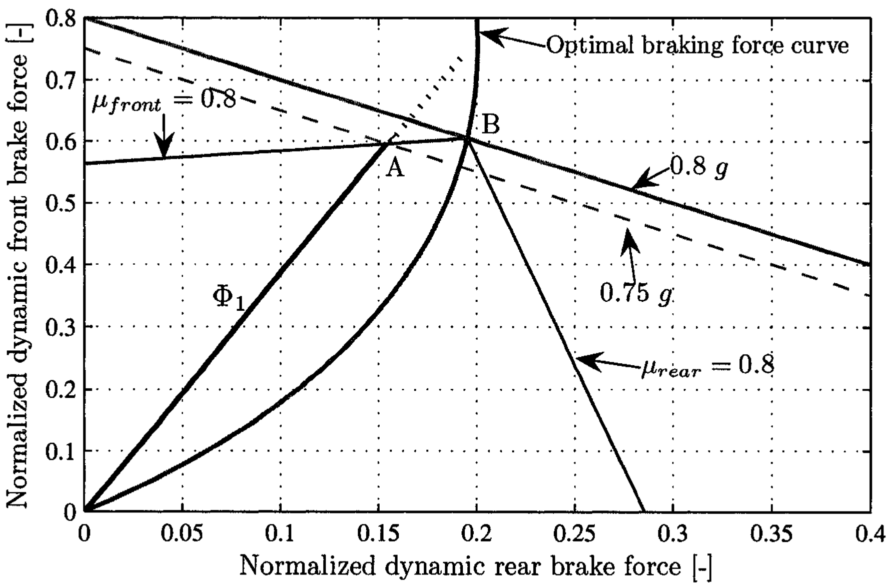

Figure 5.8: *Optimal brake force parabola with stable static brake proportioning line.* Weight-normalized front braking force is plotted against weight-normalized rear braking force, for the condition of $\mu_{friction} = 0.8$. The line of 0.8 g deceleration is highlighted, as well as the $\mu_{front} = 0.8$ and $\mu_{rear} = 0.8$ lines. The path of a stable static brake proportioning ratio, Φ_1, is plotted ($h = 0.542m$, $L = 2.690m$, $W = 14975N$,$F_{zR,static} = 5644.8N$).

Figure 5.8 displays the optimal braking parabola, as well as a static proportioning line, Φ_1. As pedal force is increasingly applied, the resulting brake force will move along the Φ_1 line towards point A. At point A, $\mu_{front} = \mu_{friction}$ and thus the front tires will lock up. If no further braking force is requested the vehicle will continue to decelerate at 0.75 g with the front tires locked. If the pedal is further depressed, no more force can be generated at the front tires, so the braking force will move along the constant $\mu_{front} = 0.8$ line towards point B. When the force reaches point B, the rear tires will lock up and the vehicle will decelerate at 0.8 g. Any further increase in brake pressure will produce no increase in braking force or deceleration.

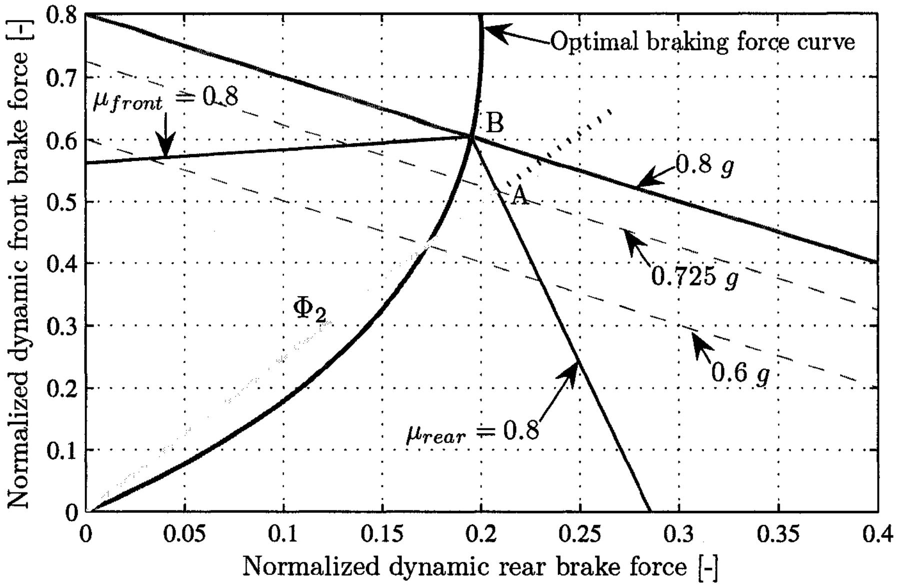

Figure 5.9: *Optimal brake force parabola with unstable static brake proportioning line.* Weight-normalized front braking force is plotted against weight-normalized rear braking force, for the condition of $\mu_{friction} = 0.8$. The line of 0.8 g deceleration is highlighted, as well as the $\mu_{front} = 0.8$ and $\mu_{rear} = 0.8$ lines. Static brake force distribution Φ_2 becomes *unstable* at decelerations greater 0.6g ($h = 0.542m$, $L = 2.690m$, $W = 14975N$,$F_{zR,static} = 5644.8N$).

Figure 5.9 displays the optimal braking parabola, as well as a second static proportioning line, Φ_2. With proportioning line Φ_2, the braking force line crosses the optimal curve at $\sim 0.6\,g$. As braking continues to increase, the rear wheels will first lock up at point A. The vehicle will then decelerate at 0.725 g with the rear tires locked up. If more braking force is required the braking will move along the $\mu_{rear} = 0.8$ line to point B. At point B the front tires will also lock up, and the vehicle will decelerate at 0.8g with all tires locked.

For Φ_2, at any deceleration greater than 0.6 g, the rear brakes will always lock before the front. This deceleration is known as the *critical deceleration*, and should be near 1 g for modern passenger cars [17]. As discussed in Section 5.1, the rear axle locking before the front will lead to vehicle instability. It can be said that Φ_2 is *unstable* beyond 0.6 g.

It is important to observe that the optimal force curves presented in Figures 5.3 to 5.9 only represent the vehicle in question for one *load case*. For instance, if the back seat were heavily loaded with passengers the static weight distribution, Ψ, as well as the CG height (and thus χ) would change. This results in a different optimal braking force curve altogether (Figure 5.10). Therefore, the optimal braking force distribution is load-dependant.

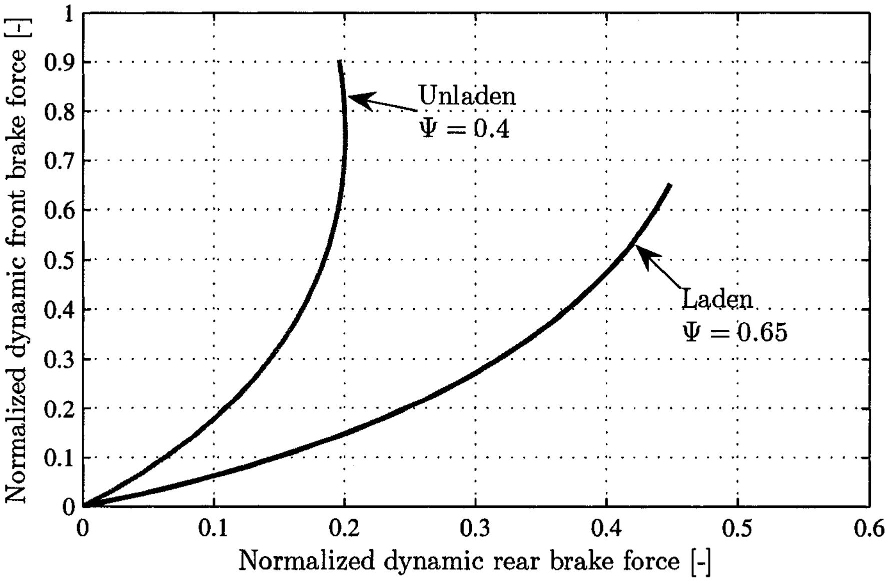

Figure 5.10: *Weight normalized optimal brake forces for two different rear load cases.* The loading of a vehicle may change the weight, static weight distribution, and CG height, resulting in fundamentally different optimal brake force curves.

5.7 Design of Static Brake Proportioning

5.7.1 Braking Efficiency

From Figure 5.11 it is clear that for any proportioning that does not lie on the optimal curve, a less than optimal acceleration level will be achieved before either the front or

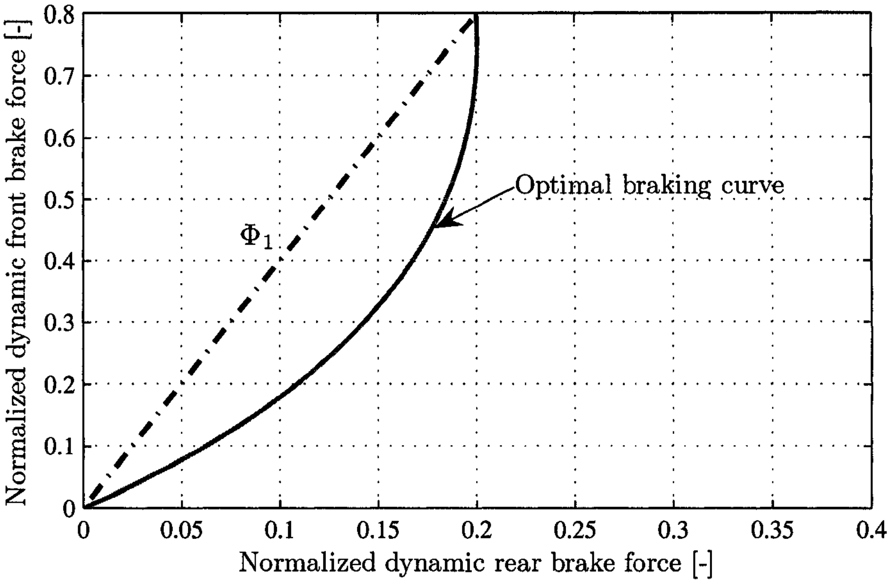

Figure 5.11: *Limitations of linear static brake proportioning.* The curve shows an optimal braking curve, and a basic static brake proportioning curve. The Φ line is far on the left side of the optimal curve, meaning the front axle will lock first. The area between Φ and the optimal curve represents unused rear braking ability.

rear tires lock up. The *braking efficiency* (Equations 5.7.1) is defined as "the ratio of maximum wheels-unlocked vehicle deceleration to tire-road friction coefficient" [17]. The braking efficiency indicates how closely the chosen proportioning, Φ, lies to the optimal path.

$$\begin{aligned} E_F &= \frac{a}{\mu_{front}} = \frac{1-\Psi}{1-\Phi-\mu_{front}\chi} \\ E_R &= \frac{a}{\mu_{rear}} = \frac{\Psi}{(\Phi+\mu_{rear}\chi)} \end{aligned} \tag{5.7.1}$$

If the brake proportioning lies directly on the optimal path, the wheels unlocked deceleration will approach $a = \mu_{friction}$ at the optimal point, and hence $E_F = E_R = 1$. For either the front axle overbraked or rear axle overbraked case, the axle in question will have a braking efficiency less than unity, indicating that it will be the first to lock up. If the braking efficiency is less than unity at one axle it will be greater than unity at the opposite axle. Greater than unity efficiency is meaningless and only indicates that the other axle will reach the traction limit first [17].

5.7.2 Design of Variable Brake Proportioning

Specialized brake pressure valves may be implemented to limit some or all additional pressure to the rear brakes above a certain pressure level. This allows the designer to create a bi-linear brake proportioning curve, and achieve higher braking efficiencies overall. The bilinear curve can be shaped to approximate the optimal braking curve.

5.7.2.1 Brake pressure limiting valve

A brake pressure limiting valve can be installed inline with the rear brake lines. At a chosen brake pressure level (intended to correspond to a pre-designed critical deceleration) the limiting valve allows no additional pressure to pass to the rear brakes (Figure 5.12). Generally the baseline first segment of the proportioning curve is chosen so that it would intercept the optimal curve at a deceleration of $0.5g$ [17].

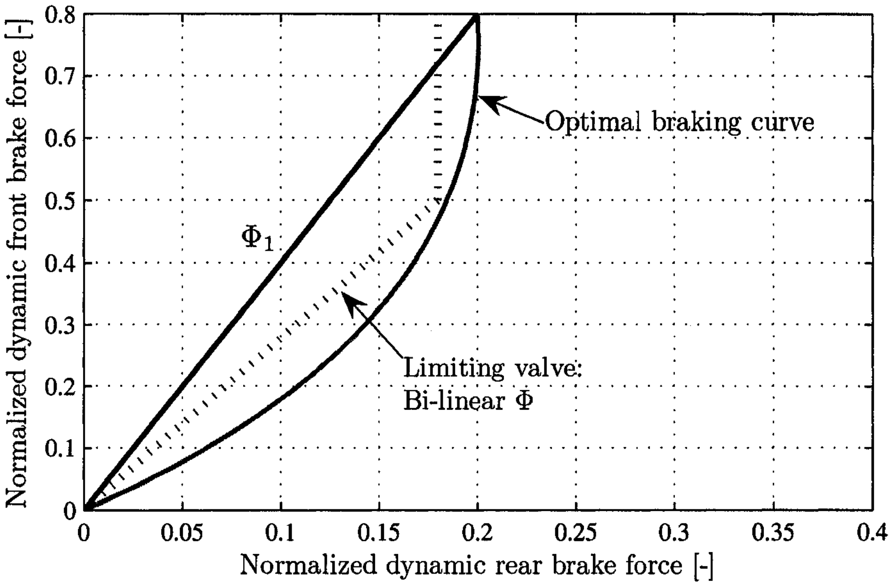

Figure 5.12: *Bi-linear brake force proportioning curve using limiter valve.* The use of a pressure limiter valve prevents the rear pressure from increasing beyond a set pressure. The bi-linear Φ curve may be designed closer to the optimal curve.

5.7.2.2 Brake pressure reducer valve

The use of a brake pressure reducer valve is similar to that of the limiter valve except that the designer now has freedom to choose the proportioning for both linear segments of the bi-linear proportioning curve, rather than just selecting a limit pressure (Figure 5.13). The advantage of the brake pressure reducer system is that it enables a closer approximation of the optimal curve (this is clear in the differences between Figures 5.12 and 5.13).

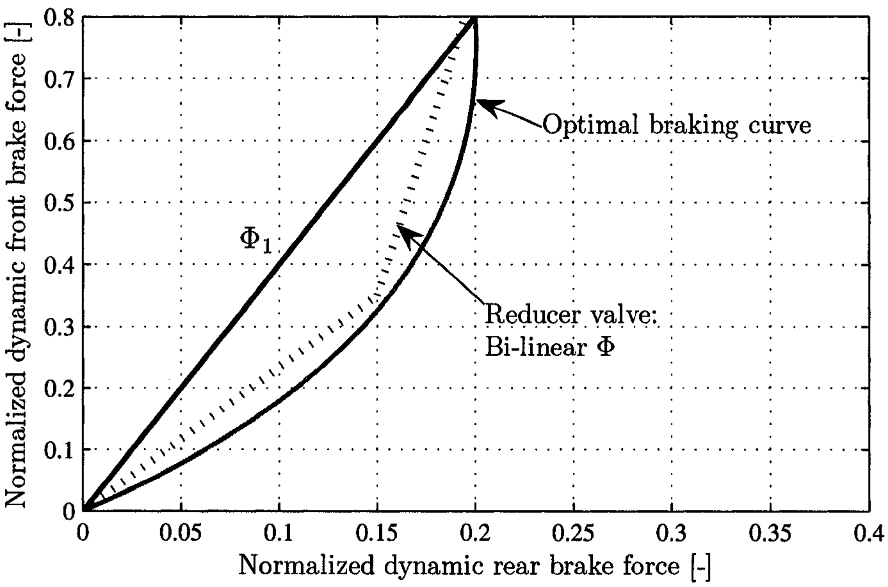

Figure 5.13: *Bi-linear brake force proportioning curve using reducer valve.* The implementation of a rear brake pressure *reducer* valve allows the design of a better bi-linear Φ curve than can be designed with a *limiter* valve (Figure 5.12).

5.7.2.3 Load-sensitive valving

Many modern vehicles further incorporate pressure limiter or reducer valves which also change the proportioning based on rear axle load. This is a necessity to accommodate the sometimes large loading changes (and hence optimal braking curve changes) between the unloaded and loaded cases. Vehicles frequently use a linear or bi-linear proportioning curve which can adjust for the laden case to remain close to the optimal force curve, and thus maintain acceptable braking efficiencies and deceleration levels.

Chapter 6

Brake Control Development

It is desired to develop an algorithm to control the output from electronic braking hardware such that optimal braking is achieved, subject to a general acceleration vector acting on the vehicle. The control algorithm will be programmed in MATLAB Simulink in order to perform computer simulations. The chosen method of control is open-loop, or may be considered predictive, rather than reactive. The system does not use feedback control to control the vehicle to a desired state. Rather, the controls constantly measure the dynamics of the vehicle, predict the braking ability of each tire, and apply the brake pressures, if desired, in the proper proportions. The system will be referred to as *Active Brake Proportioning* (*ABP*).

If it were desired to model a particular type of braking hardware, to assess its ability to achieve these desired pressures, a system model would be required. The system model of the hardware would then be used with feedback control to assess the controllability. Similarly, if it was desired to reactively eliminate a disturbance from the vehicle's motion, a vehicle model and feedback control could be used.

The control method of this project is observe the dynamic state of the vehicle, and calculate the appropriate brake proportioning at all times. Then, upon the need for braking, the brakes are applied correctly. The method is almost akin to feed-forward control, in that the controller may be aware of the disturbance (accelerations) before the control action (braking) needs to be initiated. However, the end state of the vehicle is not observed or actively controlled.

In order to determine the braking capability at each tire, the normal load must be computed based on the dynamic conditions. If the *at rest* vehicle properties are known, and the accelerations can be measured, the dynamic normal loads may be predicted.

6.1 Longitudinal Load Transfer

It is desired to measure the longitudinal vehicle acceleration, and use the measurement to accurately predict the rear-to-front load transfer. It is prudent to assess the suitability of the basic load transfer equation (Equations 5.3.1/ 6.1.1) in order to determine if more detailed equations are necessary. The theoretical equation for longitudinal weight transfer (Equation 6.1.1) utilizes only the vehicle weight, CG height, and wheelbase.

$$\Delta L = \frac{W \cdot a \cdot h}{L} \tag{6.1.1}$$

Many assumptions are required in order to make Equation 6.1.1 hold true. The equation assumes a constant CG height, constant wheelbase, and represents the entire vehicle as a sliding mass. In order to achieve more accurate normal load prediction in the brake controller, a more detailed load transfer analysis should be performed.

6.1.1 Equivalent Mass

This simplified load transfer equation (Equation 6.1.1) is derived for the simple case of a rigid sliding body (Figure 6.1). When performing a dynamic analysis on the vehicle, the entire vehicle is represented as a sliding object of mass m_{total}. Thus, the kinetic energy of the vehicle would calculated using Equation 6.1.2.

$$E = \frac{1}{2} m_{total} u^2 \tag{6.1.2}$$

In reality, there are vehicle components which move linearly in space as well as components which rotate (Figure 6.2). Energy calculations for the vehicle with rotating components must take into account masses as well as mass moments of inertia.

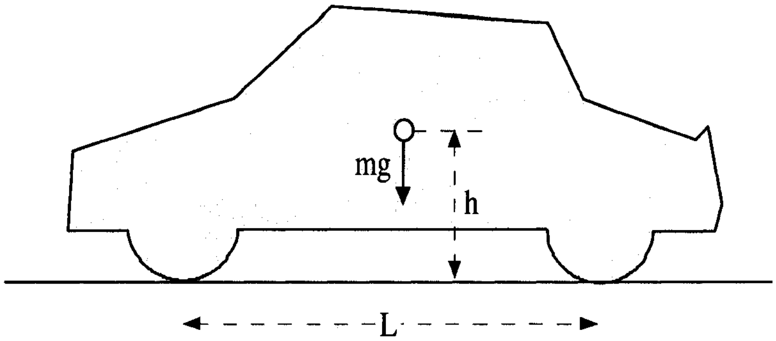

Figure 6.1: *Sliding mass representation of a braking vehicle.* Vehicle representation which ignores the inertial effects of rotating vehicle components. The most basic load transfer calculation (Equation 6.1.1) assumes this type of vehicle representation.

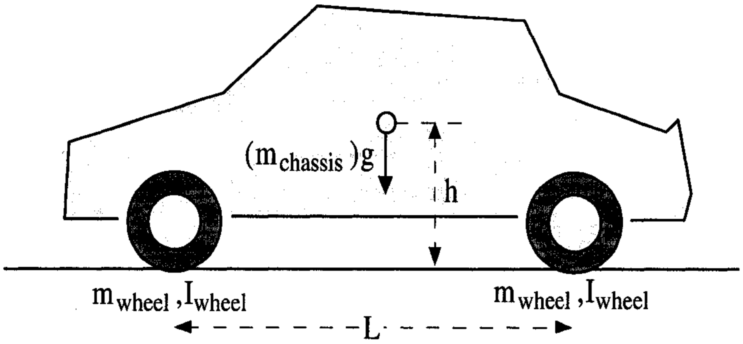

Figure 6.2: *Sliding and rolling mass representation of a braking vehicle.* A more detailed vehicle representation, relative to Figure 6.1. The sprung mass (chassis) and rotating wheels are treated as separate bodies, and thus rotational inertial effects are included in any load transfer analysis.

If the mass of the chassis is $m_{chassis}$, and each wheel possesses mass m_{wheel} and mass moment of inertia I_{wheel}, then the energy of the vehicle at a certain speed, u, would be calculated as in Equation 6.1.3. The rotational velocity of the rotating components is related to the vehicle speed by the tire rolling radius in accordance with Equation 6.1.4.

$$E = \frac{1}{2}\, m_{chassis}\, u^2 + \frac{1}{2}\, m_{wheel}\, u^2 + \frac{1}{2}\, I_{wheel}\, \omega^2 \tag{6.1.3}$$

$$\omega = \frac{u}{r_{tire}} \tag{6.1.4}$$

where:

$$r_{tire} = \text{tire rolling radius}$$

By replacing the rotational velocity, ω, in Equation 6.1.3 using Equation 6.1.4, the equation can be simplified to resemble the energy equation for the simple vehicle model (Equation 6.1.2), resulting in Equation 6.1.5. The difference is that the total vehicle mass is effectively increased by the amounts related to the rotational inertia of the rotating components.

$$\begin{aligned} E &= \frac{1}{2}\left(m_{chassis} + m_{wheel} + \frac{I_{wheel}}{r_{tire}^2}\right)u^2 \\ &= \frac{1}{2}\, m_{effective}\, u^2 \end{aligned} \tag{6.1.5}$$

where:

$$m_{effective} = \text{Effective mass of vehicle including inertial effects}$$

The equation of motion for the entire vehicle is usually computed in the form of Equation 6.1.6. This equation also assumes that the vehicle takes the form of a rigid sliding mass, and ignores the rotating inertia effects.

$$\Sigma F = m_{total} \cdot a \tag{6.1.6}$$

In order to find the actual force required to accelerate the body linearly forward as well as accelerate the rotating bodies, the effective mass from Equation 6.1.5 should be utilized (Equation 6.1.7).

$$\Sigma F = m_{effective} \cdot a \tag{6.1.7}$$

When performing dynamic vehicle analyses it is important to include the effects of rotating inertia. Using only mass to calculate the force required to accelerate the vehicle will underestimate the required force, as the true *effective mass* is larger. The inertial effects should also be included in the dynamic analysis to find normal load changes under acceleration.

In order to determine the load transferred between tires as a result of an acceleration on a vehicle, force and moment balances are performed. The load transfer calculations will be different if the vehicle is represented as a rigid mass as in Figure 6.1 or as a multi-body system as in Figure 6.2. A simple moment balance on the rigid sliding system yields the typical weight transfer equation (Equation 6.1.1).

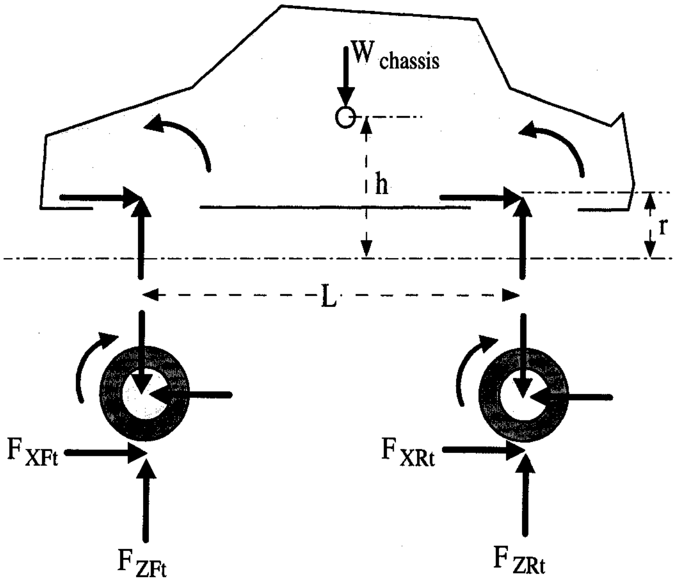

Figure 6.3: *Detailed vehicle longitudinal load transfer free body diagram.* In order to derive a more advanced equation for longitudinal load transfer during deceleration, the rotation of the wheel bodies must be considered. Brake torques are applied to the spinning wheels and load transfer as a function of the resulting deceleration can be derived. The free body diagram displays all forces in the analysis. Internal force pairs are not labeled.

Figure 6.3 shows a vehicle broken up into the chassis mass and the rotating masses. Braking torques, normal loads, and braking tire loads are applied to each wheel, and equally opposed at the chassis body. It can be shown that a force and moment balance on this vehicle model produces a new, more detailed, load transfer equation (Equation 6.1.8).

$$\Delta F_Z = \frac{m_{chassis}\, h\, a}{L} + \frac{\left[m_{front} + m_{rear} + \frac{I_{front}}{r_{tire}^2} + \frac{I_{rear}}{r_{tire}^2}\right] r a}{L} \qquad (6.1.8)$$

where:

m_{front} = mass of the front rotational components

I_{front} = mass moment of inertia of the front rotational components

m_{rear} = mass of the rear rotational components

I_{rear} = mass moment of inertia of the rear rotational components

This load transfer equation is fundamentally different, and more detailed, than the simpler form in Equation 6.1.1. In the simple equation, the mass of the rotating components were lumped together with the chassis mass at the *CG* height, h_G. In the detailed equation, the rotating components act at their actual height, the effective rolling radius of the tire. Furthermore, the mass of the rotating components includes the inertia of the rotating components. Thus, it could be considered an *effective mass* acting at the tire radii.

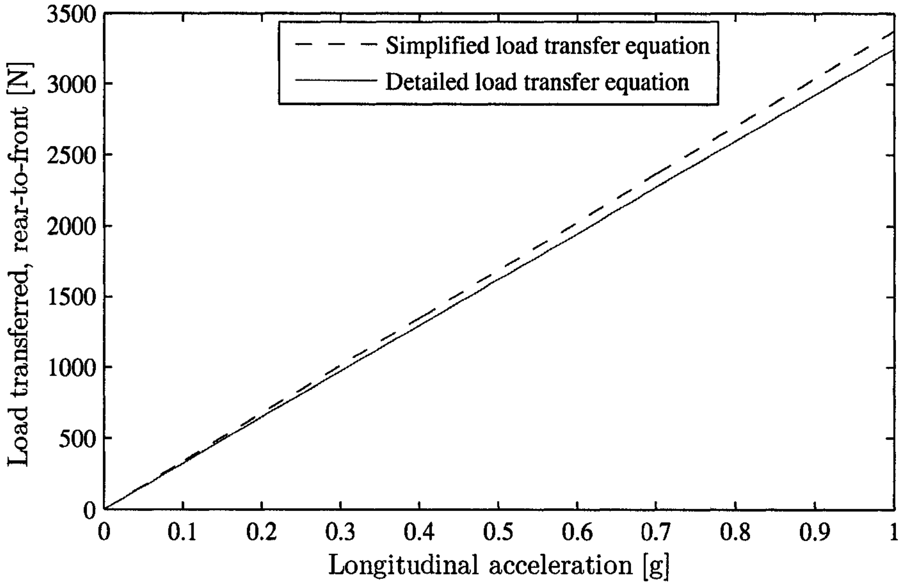

Figure 6.4: *Longitudinal load transfer vs. acceleration for simplified and detailed equations.* Normal load transferred from rear-to-front is displayed as a function of vehicle acceleration, for both the lumped mass vehicle equation and the multi-body vehicle equation. For the parameters of this vehicle the difference between the curves is 4.65%.

6.1.2 Kinematics

The equations for change in tire normal load during longitudinal acceleration depend on the *CG* height and wheelbase of the vehicle. The basic normal load transfer equation (Equation 6.1.1) assumes that no suspension deflection occurs, and hence the vehicle dimensions are constant. In reality the *CG* height may change during deceleration as a consequence of chassis pitch and jounce / rebound (vertical) motions. The wheelbase may also change as a consequence of suspension kinematics.

The *sprung mass* of a vehicle is the component of the vehicle that is supported by suspension springs (Figure 6.5). The *unsprung mass* is then the remainder, namely the wheels, tires, and the outer halves of the solid suspension linkages. The majority of vehicle mass is obviously sprung, thus the location of the sprung mass largely determines the location of the vehicle *CG*. The manner in which the sprung mass moves during changes in normal load is a complicated matter involving the full vehicle's suspension kinematics.

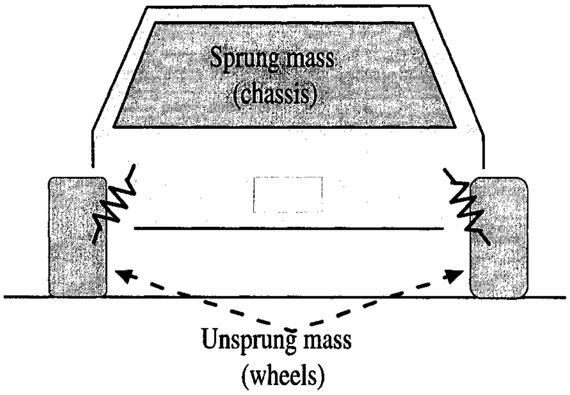

Figure 6.5: *Vehicle sprung vs. unsprung mass.* The components of a vehicle which are held up by the suspension are referred to as the sprung mass, while the remainder of the vehicle is unsprung. The sprung mass is usually taken to include the entire body/chassis as well as the inner half of all suspension components.

6.1.2.1 Effects of kinematics

Just as a vehicle rolls during cornering, it will *pitch* during longitudinal accelerations. Pitch is a result of the normal load change between the front and rear axles. When load increases at the front axle, the front springs compress, lowering the front of the vehicle. Likewise when load is transferred off the rear axle the springs expand, raising the rear. The angular motion of the sprung mass is the pitch.

Furthermore, depending on the relative spring compression and expansion of the front and rear of the vehicle, the entire chassis will lift (rebound) or droop (jounce) during accelerations.

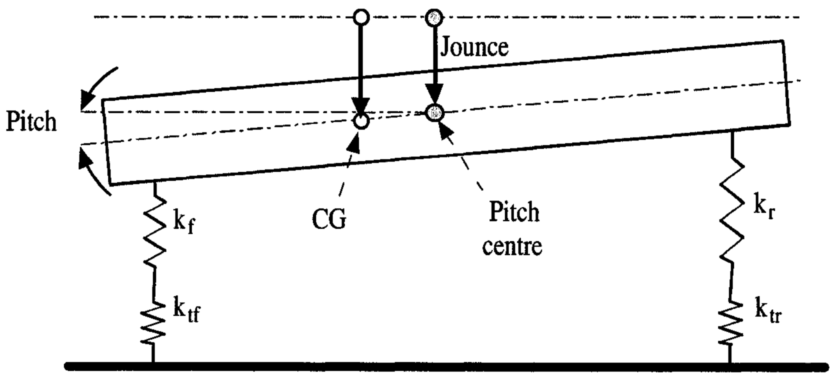

Figure 6.6: *Suspension motion during longitudinal deceleration.* During deceleration the chassis may rise or sink, as well as pitch. The *CG* will likely move to a new location through a combined vertical chassis movement plus angular rotation. If the *CG* lie directly above or below the *pitch centre* the vertical motion due to pitch angle will be negligible.

The point about which the sprung mass of the vehicle pitches when subjected to a pure pitching moment is the *instantaneous centre or pitch*, or the pitch centre. The pitch centre can be further defined as *the point through which the axis of rotation of the vehicle must pass, such that no longitudinal motion occurs at the point of contact of either tire on the road.* Following from the definition, a longitudinal force applied to the sprung mass directly at the pitch centre will cause *zero* body pitch. It is important to note that pitch angle does not affect the amount of load transferred, unless other vehicle parameters such as *CG* height are changed as a consequence of the pitch.

The location of the pitch centre relative to the *CG* influences the amount of pitch. In reality, however, as the tires are free to move longitudinally, the chassis is not constrained to pitch about the pitch centre. The actual motion of the chassis is a combination of pitching and lifting. The combined path means that the chassis actually pitches about a moving point in space. The complex motion of the chassis under longitudinal accelerations (Figure 6.6) may significantly change the *CG* height.

In order to determine the importance of including dynamic changes in *CG* height in load transfer prediction, preliminary simulations were performed with the large sedan CarSim model (Table B.1) to examine the changes. For a straight line braking simulation in which the vehicle decelerated at $\sim 0.7g$, it was observed that the *CG* height changed only $2-3\%$ (Figure 6.7). Because the load transfer equation is largely a linear function *CG* height (Equation 6.1.8), the error induced by neglecting *CG* height changes should be equal to $2-3\%$ or less. Relative to other sources of error, such as unknown conditions of the tires, conditions of the tire-road interface, and the static loading of the vehicle (passengers and luggage), it was determined that the error induced by assuming a constant *CG* height during longitudinal deceleration was acceptable.

6.1.3 Longitudinal load transfer results

It was decided to use Equation 6.1.8 in order to predict longitudinal load transfer for the brake controller. The equations were implemented into a Simulink brake control module (Figure 6.8). Figures 6.9 and 6.10 show preliminary normal load prediction results using Equation 6.1.8 with a front wheel drive sedan model. The simulations were carried out in CarSim with load prediction carried out in MATLAB Simulink. The inputs to the load prediction algorithm were static vehicle properties (weight, weight distribution, wheelbase, *CG* height, etc.), as well as vehicle acceleration values from CarSim. The results show close agreement between the tire normal loads in CarSim and those predicted by Simulink.

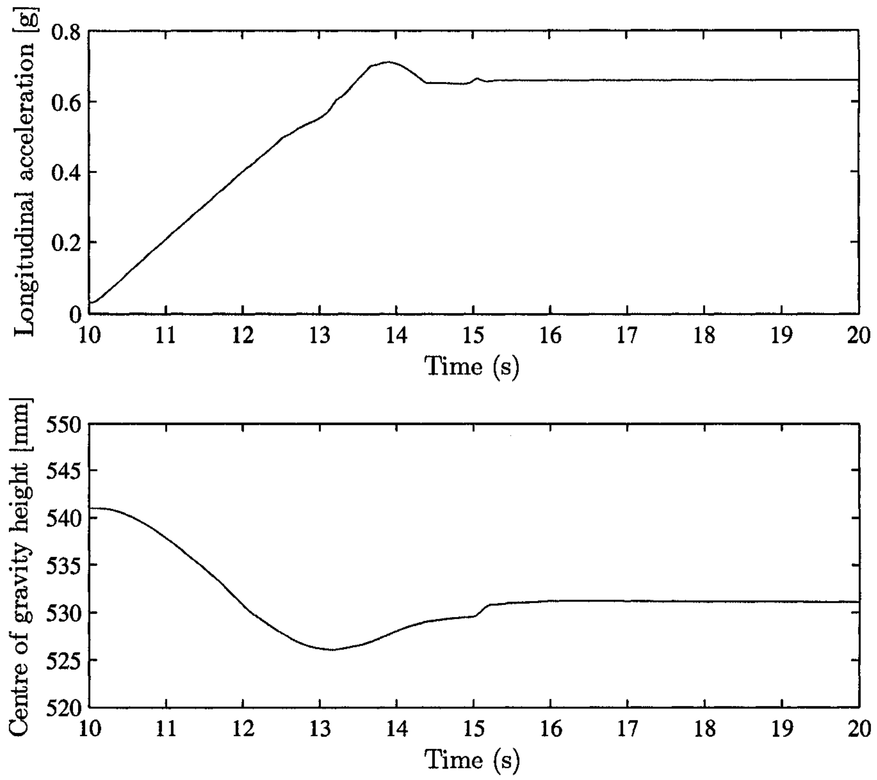

Figure 6.7: *Change in CG height and longitudinal deceleration vs. time.* For an example straight line braking simulation under which the vehicle reached a deceleration of ~ 0.7 g, the *CG* height changed ~ 2.7%. The vehicle was cruising steady-state from time 0 to 10 s. The brakes were applied at time 10 s, and the steady-state coasting period from 0 – 10 s is not shown.

As the tires on the vehicle lock up, there are transient effects which cannot be easily modeled in the load transfer predictor algorithm. The brake proportioning controller is concerned primarily with the vehicle dynamics *up to* the point of tire lockup, so inaccuracies during lockup should not adversely affect the system performance. The error during the longitudinal braking maneuver reached a peak of ~ 6% before the onset of lockup. During the transient behaviour of the tire lockup event, the error reaches ~ 12%.

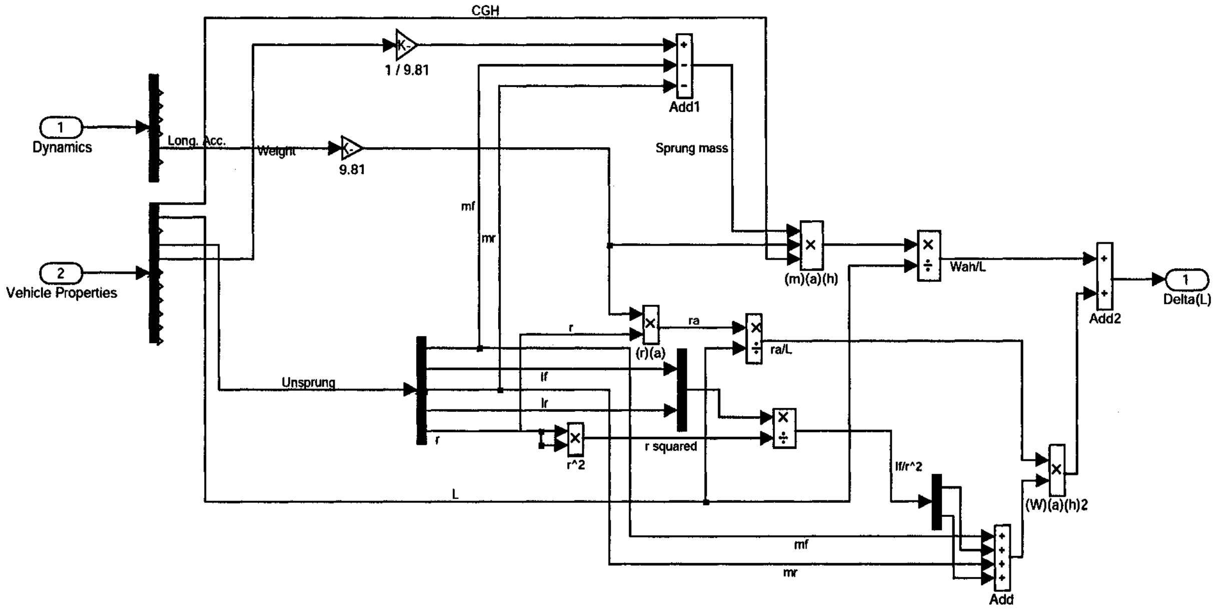
CGH
1 / 9.81
Add1
1
Dynamics
Long. Acc.
Weight
9.81
Sprung mass
mf
mr
(m)(a)(h)
Wan/L
Add2
1
Delta(L)
2
Vehicle Properties
r
ra
(r)(a)
ra/L
lf
lr
Unsprung
r
r^2
r squared
lf/r^2
L
(W)(a)(h)2
mf
mr
Add

Figure 6.8: *Simulink block diagram for longitudinal load transfer prediction.*

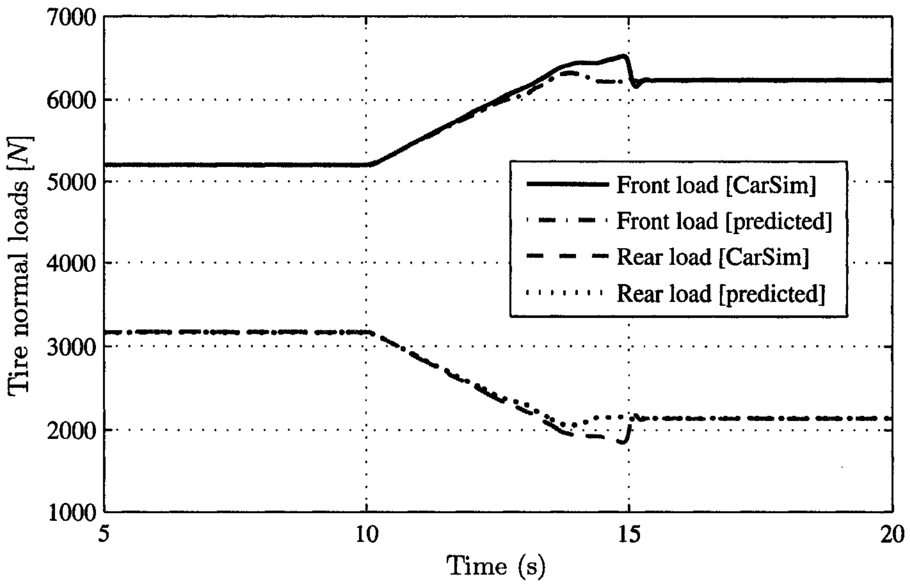

Figure 6.9: *Normal loads during longitudinal deceleration (CarSim and predicted).* The basic sedan vehicle model underwent deceleration in a straight line, beginning at time 10s. Tire lockup occurred at time 14s. Actual tire normal loads from CarSim and predicted tire loads using Equation 6.1.8 are shown to be in close agreement.

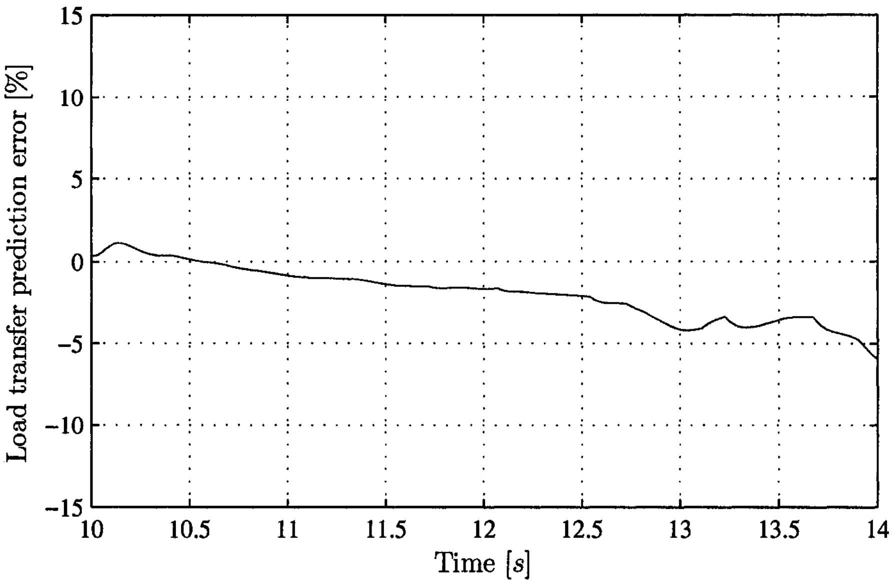

Figure 6.10: *Percent error in normal load prediction during longitudinal deceleration.* For the longitudinal deceleration simulation also shown in Figure 6.7 the % error in transferred tire normal load is plotted. The time frame displayed is from brake application at 10s until tire lockup at 14s. After time 14s transient effects produced a maximum error of 12%. The period of interest for brake proportioning is leading up to tire lockup. The peak error before tire lockup occurred was $\sim$ 6%.

6.2 Lateral Load Transfer

In order to accurately distribute braking pressures during cornering events, the load transfer in the vehicle due to lateral acceleration must be predicted. The simplest form of the equation for predicting lateral load transfer is found by modifying Equation 6.1.1. Lateral acceleration is substituted for longitudinal deceleration, and track width is substituted for wheelbase (Equation 6.2.1).

$$\Delta L = \frac{W \cdot a_{lateral} \cdot h}{T} \tag{6.2.1}$$

For longitudinal load transfer, the transfer effect is equal on the left and right sides of the vehicle, because the suspension is symmetrical. However, for lateral load transfer this is not the case. The front and rear suspensions commonly have very different properties. Though the total lateral load transfer may be given by Equation 6.2.1, a detailed analysis is required to determine the load transferred at each axle.

6.2.1 Roll Force analysis

When load is transferred to the outside tires, the outer springs compress. Likewise, the load relief on the inside springs during cornering causes those springs to expand. The net result is that the sprung mass rolls outwards, and may also jounce or rebound.

The point about which the sprung mass of the vehicle rolls when subjected to a pure roll moment is the *instantaneous centre of roll*, or the roll centre [8]. The roll centre can be further defined as *the point through which the axis of rotation of the vehicle must pass, such that no lateral motion occurs at the point of contact of either tire on the road.* It is important to note that in reality the vehicle is not constrained to roll about the roll centre, as the wheels are free to move laterally at the road. Still, roll centres are extremely valuable in approximating the roll properties of a vehicle.

It follows from the definition of the roll centre that a lateral force applied to the sprung mass directly at the roll centre will cause no body roll. This is akin to applying a force to a wheel, pointed directly at the axis of rotation of the wheel; the force creates no moment about the axis of rotation, and hence causes no rotation.

Because the actual forces acting on the vehicle sprung mass can be resolved to the CG location, the distance between the CG and the roll centre determines the amount of body roll that will result from lateral forces. If the roll centre and CG coincided, no body roll would occur. Likewise the further the roll centre lies above or below the CG, the more roll will occur.

When the roll centre is at a distance from the CG, so that lateral forces do indeed cause roll, the lateral forces are transferred through the *sprung path.* That is, the lateral force at the CG is reacted at the suspension by resisting forces in the springs, causing compression and expansion, and thus roll. When the roll centre is close to or coincident with the CG, little or no roll occurs due to lateral forces. In this case, the forces are transmitted through the rigid components of the suspension, such as the control arms and suspension linkages.

When body roll occurs, each axle creates a moment to oppose the roll. Because the front and rear suspension stiffnesses differ, the load transferred through the springs to resist the roll angle will be different. It is important to note that roll angle does affect the total amount of load transferred, unless other vehicle parameters such as CG height are changed as a consequence of the roll.

In order to determine the amount of roll for a given lateral force, the roll stiffness of the suspension must be determined. The vertical stiffness of the tire and the stiffness of the suspension spring were assumed to act as springs in series (Figure 6.11). Thus, the vertical stiffness at each corner was calculated using Equation 6.2.2.

$$K_{suspension} = \frac{1}{\frac{1}{k_{spring}} + \frac{1}{k_{tire}}} \tag{6.2.2}$$

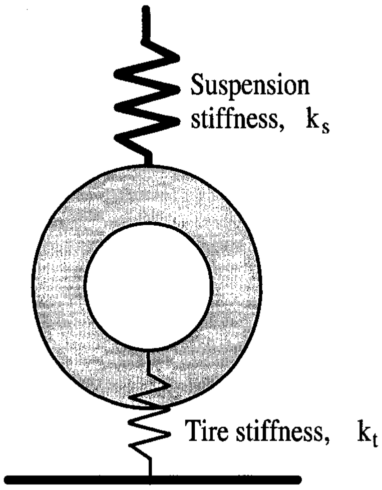

Figure 6.11: *Suspension and tire stiffnesses in series.* In order to calculate the roll stiffness of the vehicle, the suspension stiffness and tire vertical stiffness at each corner of the vehicle were treated as springs in series. Each was assumed to act as a linear spring in the range of interest.

Where

$K_{suspension}$ = total vertical stiffness

k_{spring} = coil spring vertical stiffness

k_{tire} = tire vertical stiffness

In addition to coil springs or leaf springs at each wheel, most vehicle incorporate *anti-roll bars.* The the anti-roll acts as a spring that creates a moment in reaction to any roll of the vehicle chassis. By utilizing vertical springs at the corners of the vehicles and separate springs that only act in roll, the vehicle designer is able to partially *decouple* the roll and jounce stiffnesses of the vehicle. When computing the roll stiffness of the suspension the anti-roll bar acts in parallel with the vertical corner stiffness (Figure 6.12).

Performing a moment balance about the roll centre in Figure 6.12 yields the following equation:

$$Wa\left(h_{cg} - h_{rc}\right)\cos\phi + W\left(h_{cg} - h_{rc}\right)\sin\phi = F_{inner}\cdot\frac{T}{2} + F_{outer}\cdot\frac{T}{2} + M_{arb} \qquad (6.2.3)$$

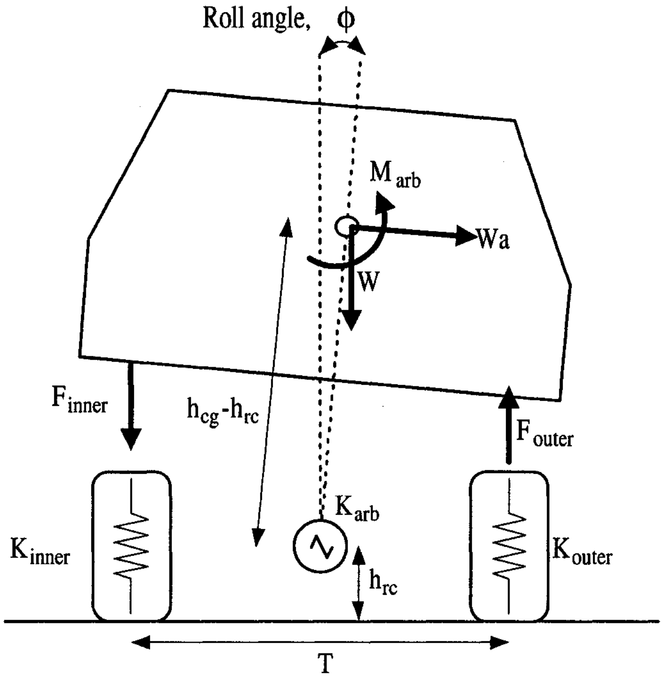

Figure 6.12: *Free body diagram for roll stiffness calculation.* A free body diagram of a vehicle undergoing a roll angle, ϕ, is shown. The anti-roll bar stiffness is shown at the roll centre, with a value of K_{arb}. The combined stiffness at the inner and outer corners are shown as K_{inner} and K_{outer}, respectively. The height of the roll centre and CG are h_{rc} and h_{cg}, respectively.

where:

ϕ = vehicle roll angle

h_{rc} = vehicle roll centre height

h_{cg} = vehicle CG height

The equation is simplified and further developed by defining $(h_{cg} - h_{rc})$ as h_s, and substituting in $F = K\Delta z$ for the coil springs, and $M_{arb} = K_{arb} \cdot \phi$ for the anti-roll bar.

$$Wah_s \cos\phi + Wh_s \sin\phi = (K_{inner} \cdot \Delta z) \cdot \frac{T}{2} + (K_{outer} \cdot \Delta z) \cdot \frac{T}{2} + K_{arb} \cdot \phi \qquad (6.2.4)$$

where:

h_s = height of CG above roll centre

The vertical expansion or compression at the tires can be found from geometry to be $\frac{T}{2} \cdot \sin\phi$.

$$Wah_s \cos\phi + Wh_s \sin\phi = \left(K_{inner} \cdot \frac{T}{2} \cdot \sin\phi\right) \cdot \frac{T}{2} + \left(K_{outer} \cdot \frac{T}{2} \cdot \sin\phi\right) \cdot \frac{T}{2} + K_{arb} \cdot \phi \tag{6.2.5}$$

Because the left and right side suspensions are identical, $K_{inner} = K_{outer}$.

$$Wah_s \cos\phi + Wh_s \sin\phi = \left(K_{wheel} \cdot \frac{T^2}{2} \cdot \sin\phi\right) \cdot + K_{arb} \cdot \phi \tag{6.2.6}$$

For normal or near limit driving in a typical passenger sedan or sport utility vehicle, roll angles will always fall in a single-digit range. Thus, trigonometric simplifications can be made. It will be assumed that $\sin\phi \approx \phi$, and $\cos\phi \approx 1$.

$$\begin{aligned} Wah_s + Wh_s\phi &= K_{wheel} \cdot \frac{T^2}{2} \cdot \phi + K_{arb} \cdot \phi \\ &= \left(K_{wheel} \cdot \frac{T^2}{2} + K_{arb}\right) \cdot \phi \end{aligned} \tag{6.2.7}$$

Therefore, the roll stiffness of the suspension is the bracketed term on the right side of the equation (Equation 6.2.8), where the suspension stiffness K_{wheel} is defined in Equation 6.2.2.

$$K_{roll} = K_{wheel} \cdot \frac{T^2}{2} + K_{arb} \tag{6.2.8}$$

The roll angle for the sprung mass subjected to a lateral acceleration, a, can then be determined (Equation 6.2.9).

$$\phi = \frac{Wah}{K_{roll} - Wh} \tag{6.2.9}$$

6.2.2 Load transfer analysis

With a known roll angle for a given value of lateral acceleration (Equation 6.2.9), it is desired to determine the load transferred to the outside wheels as a consequence of the lateral acceleration. Unlike in the case of longitudinal accelerations, the load transferred laterally is not simply distributed 50% per suspension. In order to determine the distribution of transferred load between the front and rear axle, it is necessary to analyze the vehicle as a whole. It is assumed that the front and rear suspensions are constrained to have the same roll angle (flexure of the chassis is negligible), and hence the vehicle roll angle is calculated using Equation 6.2.10.

$$\phi = \frac{Wah_s}{K_{roll_{front}} + K_{roll_{rear}} - Wh_s} \tag{6.2.10}$$

where:

$K_{roll_{front}}$ = roll stiffness of the front suspension

$K_{roll_{rear}}$ = roll stiffness of the rear suspension

The entire sprung mass rotates about the roll axis of the vehicle, which is a line connecting the front and rear roll centres (Figure 6.13). The height of the roll centre under the vehicle CG is calculated using Equation 6.2.11. It is calculated based on the static front and rear weight distribution, as is the longitudinal location of the CG.

$$h_{rc} = h_{rc,rear} + \left(h_{rc,front} - h_{rc,rear}\right)\left(\frac{F_{zF,static}}{W}\right) \tag{6.2.11}$$

Given the roll angle of the vehicle about the roll axis from Equation 6.2.10, and knowing

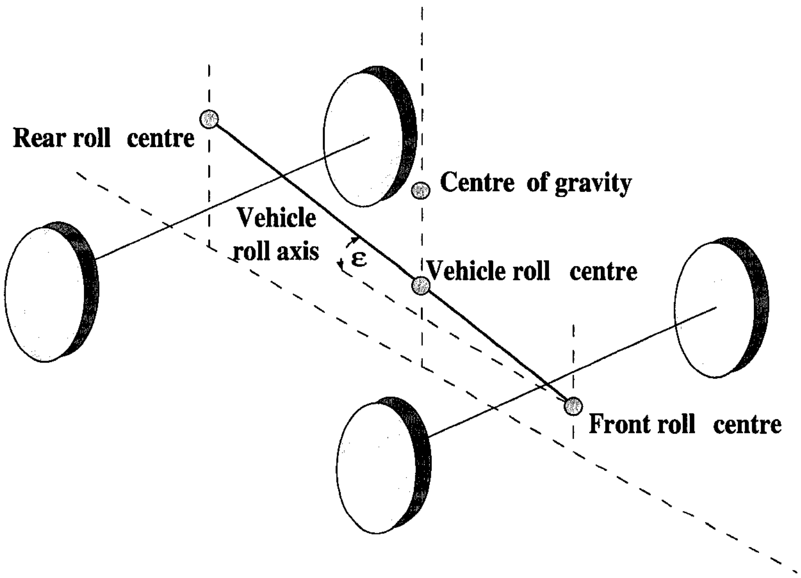

Figure 6.13: *Vehicle roll centres and roll axis.* The line drawn between the roll centres of the front and rear suspensions forms the vehicle roll axis. The roll centre considered in full vehicle sprung mass analyses is the point on the roll axis below the vehicle CG.

the roll stiffness of each suspension from Equation 6.2.8, the moment at the front and rear can be calculated (Equation 6.2.12).

$$M_{\phi,i} = K_{roll,i}\left(\frac{Wah_s}{K_{roll,front} + K_{roll,rear} - Wh_s}\right) \tag{6.2.12}$$

where:

i = represents either the front or rear axle

$M_{\phi,i}$ = moment about the ith axle caused by roll

K_{roll_i} = roll stiffness of the ith suspension

While Equation 6.2.12 represents the roll moment caused by sprung mass roll, there is also a load transfer moment caused by transmission of load through the rigid path of the suspension. As the roll load is proportional to the distance from the roll centre to the CG, the rigid transferred load is proportional to the distance from the ground to the roll centre (Equation 6.2.13).

$$M_{rigid,i} = F_{zi,static}h_{rc,i}a \tag{6.2.13}$$

where:

$M_{rigid,i}$ = moment caused by lateral load transferred through rigid path

$F_{zi,static}$ = weight on ith axle

$h_{rc,i}$ = roll centre height at ith axle

For a moment about the vehicle, in whole or at either axle, the force across the axle can be found using Equation 6.2.14.

$$M = \Delta F \cdot T \tag{6.2.14}$$

where:

M = moment on the vehicle or axle

ΔF = change in load at tires to react moment

T = track width of the vehicle or axle

Combining Equations 6.2.12, 6.2.13, and 6.2.14, the lateral load transfer due to cornering lateral acceleration is found to be Equation 6.2.15.

$$\Delta F_{z,i} = \left(K_{roll,i}\frac{Wah_s}{K_{roll,front} + K_{roll,rear} - Wh_s}\right)\left(\frac{1}{T}\right) + \frac{F_{zi,static}h_{rc,i}a}{T} \tag{6.2.15}$$

6.2.3 Kinematics

As in the case of longitudinal deceleration, the motion of the sprung mass due to suspension kinematics can change the location of the vehicle *CG* during lateral accelerations. It is necessary to investigate the order of magnitude of the changes, and the possible effects on accuracy

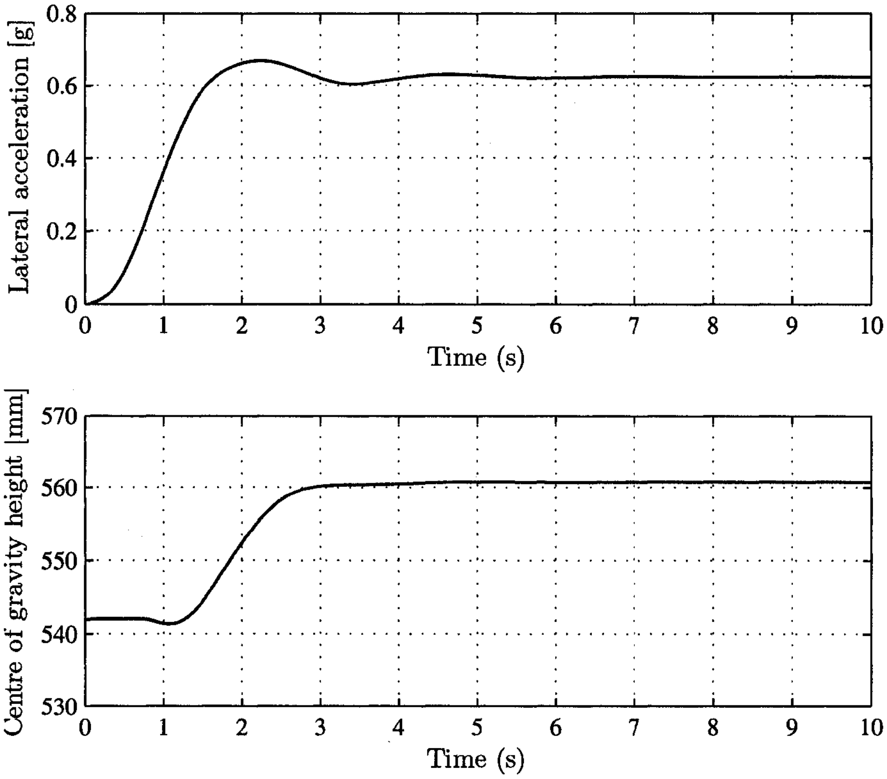

Figure 6.14: *CG height change as vehicle undergoes lateral acceleration.* For a cornering maneuver on the CarSim large sedan vehicle model, the *CG* height was only found to change ~ 3%.

A cornering maneuver was carried out on the large sedan CarSim model (Table B.1), and *CG* height was observed (Figure 6.14). It was seen that for the typical sedan simulations, the *CG* height changed only 3.3% subject to a lateral acceleration of more than 0.6 g.

Considering all other sources of inaccuracy and measurement uncertainties, this error was deemed acceptable.

The lateral load transfer analysis requires knowledge of the roll centre properties of the front and rear suspensions. Roll centre locations are usually referenced as a *roll centre height*, but in reality the roll centre migrates both vertically and laterally during suspension motions. As the vehicle suspension jounces or rebounds, and the suspensions remain symmetrical, the roll centre will migrate up and down.

When the vehicle rolls, the inside and outside suspensions are in very different states, and as a consequence the roll centre will move in the lateral direction. It becomes complicated to try to predict the roll centre height through all ranges of suspension motion, and it was decided to assume a constant *CG* height at the vehicle centre plane.

6.2.4 Lateral load transfer results

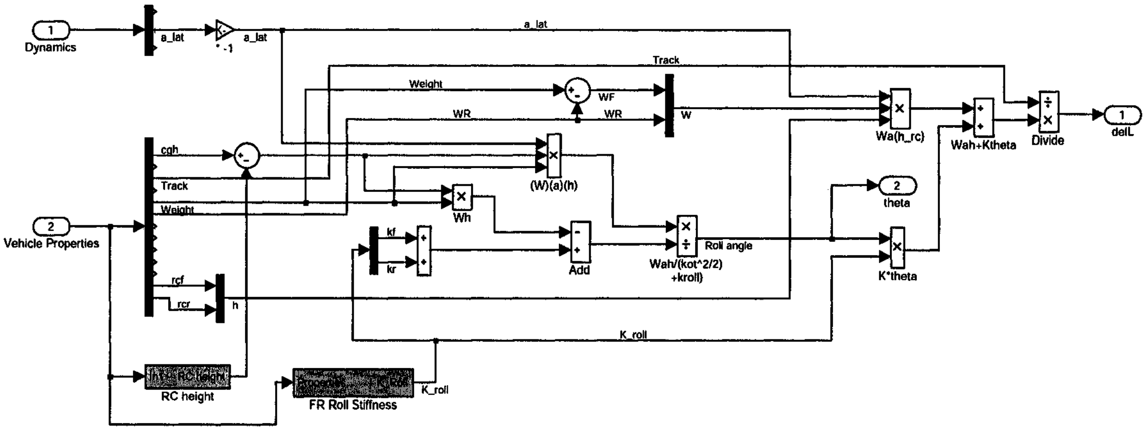
1
Dynamics
a_lat
* -1
a_lat
a_lat
Track
Weight
WF
WR
WR
W
Wa(h_rc)
Wah+Ktheta
Divide
1
delL
cgh
Track
Weight
(W)(a)(h)
Wh
2
Vehicle Properties
kf
kr
Add
Roll angle
Wah/(kot^2/2)
+kroll)
2
theta
K*theta
rcf
rcr
h
K_roll
RC height
FR Roll Stiffness
K_roll

Figure 6.15: *Simulink block diagram for lateral load transfer prediction.*

It was decided to use Equation 6.2.15 to predict the lateral tire load transfer. The equation, as well as Equations 6.2.2, 6.2.8, 6.2.10, 6.2.11, were implemented in a Simulink load prediction module Figure 6.15).

A cornering maneuver was carried out using the CarSim large sedan vehicle model. The vehicle entered a corner at 110 $\frac{km}{h}$, held the steady state corner from $4 - 10$ seconds,

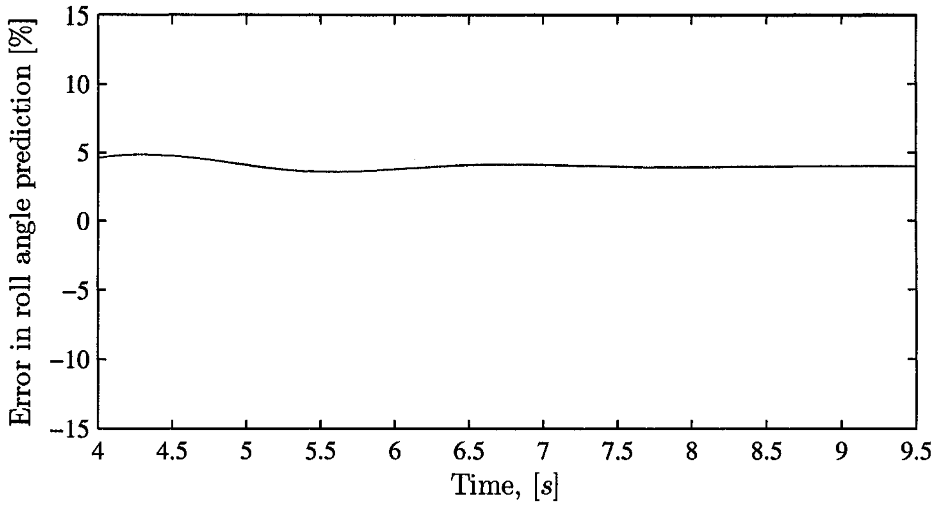

Figure 6.16: *Steady state cornering error in roll angle prediction.* For the cornering maneuver on the CarSim large sedan vehicle model, the actual and predicted roll angle were observed. During steady state cornering, the error was found to be ~ 5%.

and subsequently braked until the end of the simulation. Figure 6.16 displays the error in roll angle prediction during steady state cornering. The percent difference was observed to be approximately 5 percent.

The Simulink model was used to predict the lateral load transfer at the front and rear axles, and hence the normal load on each tire. The tire loads are presented in Figure 6.17. The predicted tire loads clearly show close agreement both in trends and magnitudes. Furthermore, the percent errors in tire load prediction during steady-state cornering are presented in Figure 6.18. Throughout the steady-state cornering the errors remain less than ±5%.

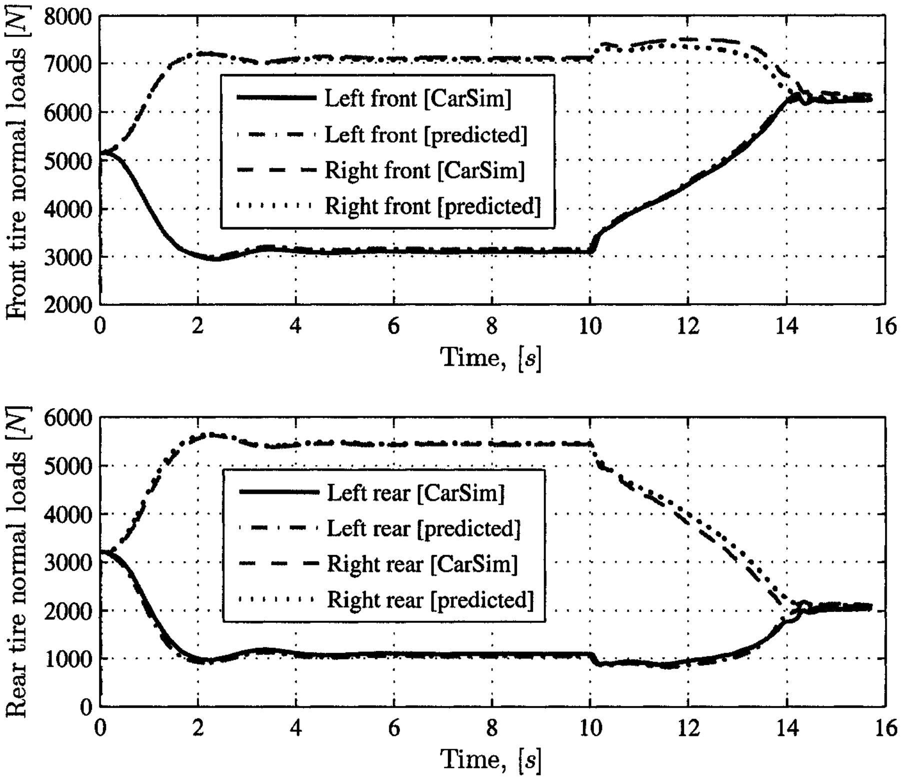

Figure 6.17: *Tire loads during cornering maneuver.* During a cornering maneuver simulation using the CarSim large sedan vehicle model, the actual and predicted tire normal loads were observed. The predicted loads from Simulink show close agreement with those from CarSim.

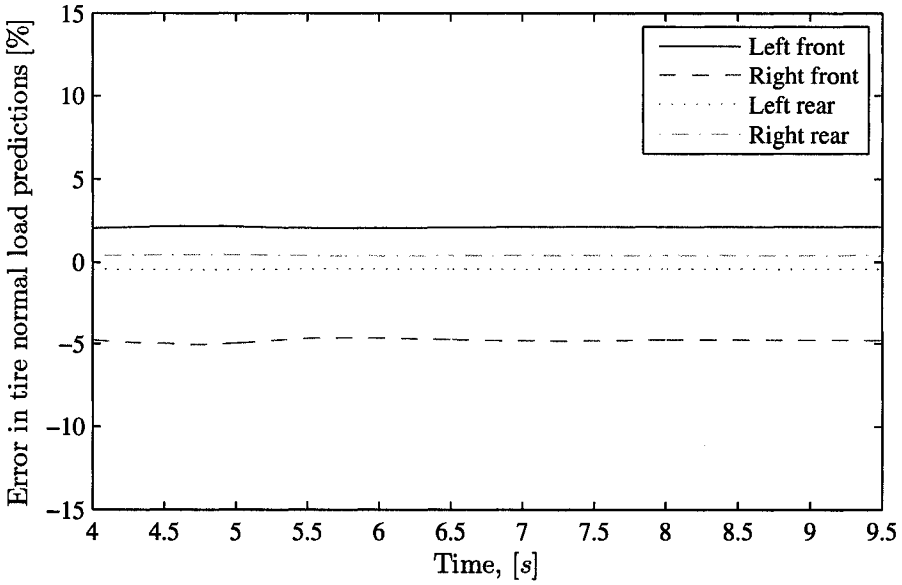

Figure 6.18: *Error in tire normal load prediction during steady state cornering.* During a cornering maneuver simulation using the CarSim large sedan vehicle model, the actual and predicted tire normal loads were observed. The error in each of the tires during steady state cornering was less than | 5% |.

6.3 Combined Longitudinal and Lateral Load Transfer

It is necessary to predict tire normal loads in situations of combined braking and cornering. Therefore, the results of the longitudinal and lateral load transfer prediction algorithms must be combined. For a longitudinal load transfer value $\Delta F_{z,long}$, front lateral load transfer value $\Delta F_{z,lat,front}$, and rear lateral load transfer value $\Delta F_{z,lat,rear}$, the load on each of the four tires is calculated by Equation 6.3.1. Equation 6.3.1 was implemented in a Simulink control algorithm (Figure 6.19). The section of the results displayed in Figure 6.17 from 10 seconds to 14 seconds represents combined lateral acceleration and longitudinal deceleration.

$$\begin{aligned}
F_{z,front,right} &= \frac{1}{2}\left(W_{front} + \Delta F_{z,long}\right) + \Delta F_{z,lat,front} \\
F_{z,front,left} &= \frac{1}{2}\left(W_{front} + \Delta F_{z,long}\right) - \Delta F_{z,lat,front} \\
F_{z,rear,right} &= \frac{1}{2}\left(W_{rear} - \Delta F_{z,long}\right) + \Delta F_{z,lat,rear} \\
F_{z,rear,right} &= \frac{1}{2}\left(W_{rear} - \Delta F_{z,long}\right) - \Delta F_{z,lat,rear}
\end{aligned} \tag{6.3.1}$$

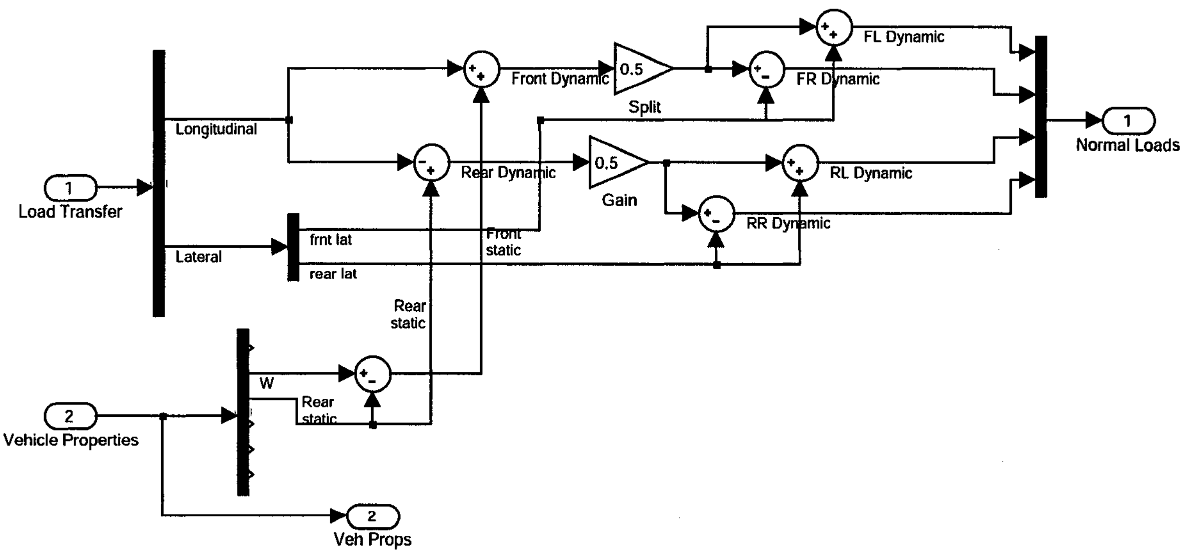
1
Load Transfer
Longitudinal
Lateral
frnt lat
rear lat
Front Dynamic
Rear Dynamic
0.5
Split
0.5
Gain
Front static
Rear static
FL Dynamic
FR Dynamic
RL Dynamic
RR Dynamic
1
Normal Loads
2
Vehicle Properties
W
Rear static
2
Veh Props

Figure 6.19: *Simulink module for longitudinal and lateral combined load transfer.*

6.4 Tractive Capabilities Prediction

By predicting the load transfer caused by vehicle accelerations, the normal loads at each tire have been found. In order to apply the brakes most effectively, the value of interest is not necessarily tire normal load, but *tractive ability.* Because tire tractive ability sees diminishing returns with increased normal load, it is not adequate to apply the brakes in direct proportion to the normal loads.

The load sensitivity of tires, as described in Section 3.3, has a profound effect on vehicle behaviour near the limits of traction. The braking force analyses performed in Chapter 5 neglected load sensitivity. Figure 6.20 displays the peak lateral load as a function of tire normal load, for a typical tire. If the line were perfectly linear, it would take the form $F_y = k \cdot F_z$, where k would be the traditional definition of *coefficient of friction.*

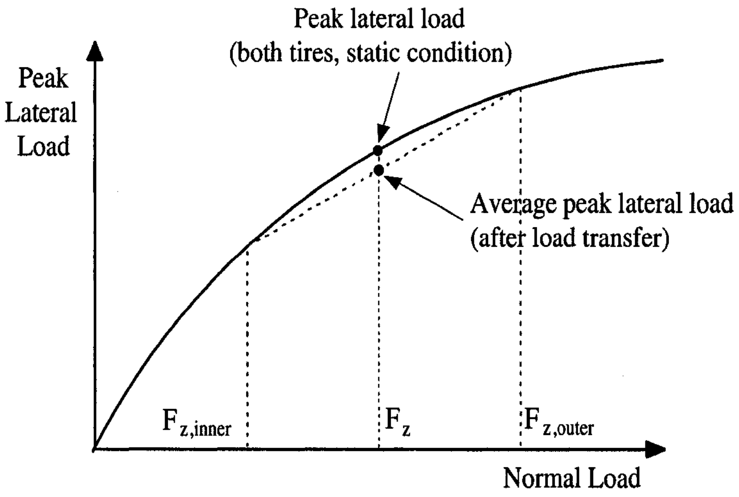

Figure 6.20: *Tire lateral load capabilities vs. normal load.* As normal load increases, the peak lateral load capability of a pneumatic tire increases with a decreasing rate. Were it traction coefficient, μ, plotted, the trend would be identical.

For pneumatic tires, the peak traction coefficient is not a constant, but rather *decreases* with increasing normal load. At any normal load, the tire shown in Figure 6.20 could produce the lateral load on the curve, or a lower value of lateral load. The normal operating range of a tire is the full area below the curve. Thus, the curve represents the peak traction capability, or the lateral force at which tire lockup will occur, for any given normal load.

For the purpose of predicting the tractive capability of the tires on the vehicle to be controlled, it is important to consider the load sensitivity. If the controller was programmed with the exact data for the tires on the vehicle, it could lookup the maximum capability for the current normal load for each tire. However, this strategy is doomed for failure, as the curve itself could be completely different for any number of reasons, including but not limited to, wet or dry road conditions, the wear / age of the tire, whether the vehicle owner has fitted it with non-OEM replacement tires, and the tire temperature.

It must suffice, then, to summarize the effects of tire load sensitivity as a *rule of thumb.* Gillespie [8] states that the traction coefficients for both lateral and longitudinal forces "will decrease on the order of 0.01 for a 10% increase in load" [8].

It was found that if the peak traction coefficient, μ, is defined as a linear function of % change in tire normal load, above or below a nominal, or reference, load (Figure 6.21), that the resulting peak lateral force versus normal force curve follows a reducing rate trend.

The μ and tractive ability curves are plotted for two cases, in Figures 6.21 and 6.22. Figure 6.21 displays the curves for an exaggerated μ relationship. 6000 N is defined as the nominal static tire load, and $\mu = 1$ is defined as the nominal *normal* value for traction coefficient. The μ curve is clearly linear with *%change* as normal load varies above and below 6000 N, and the tractive force capability curve clearly displays the expected *decreasing rate* trend.

Figure 6.21 displays the same linear μ curve and decreasing rate tire force curve, for a more realistic μ equation following the trend given by Gillespie [8]. The value of μ in this case decreases 0.01 for each 10% increase above the *nominal* load. Likewise μ increases 0.01 for each 10% below the nominal load.

The choice of nominal normal load determines when the nominal μ will equal 1. Thus, the curve is scaled in order to intersect at the $\mu = 1$ equality of $F_{lateral} = F_{normal}$. Depending on the choice of nominal normal load and the choice of slope for the μ curve, the

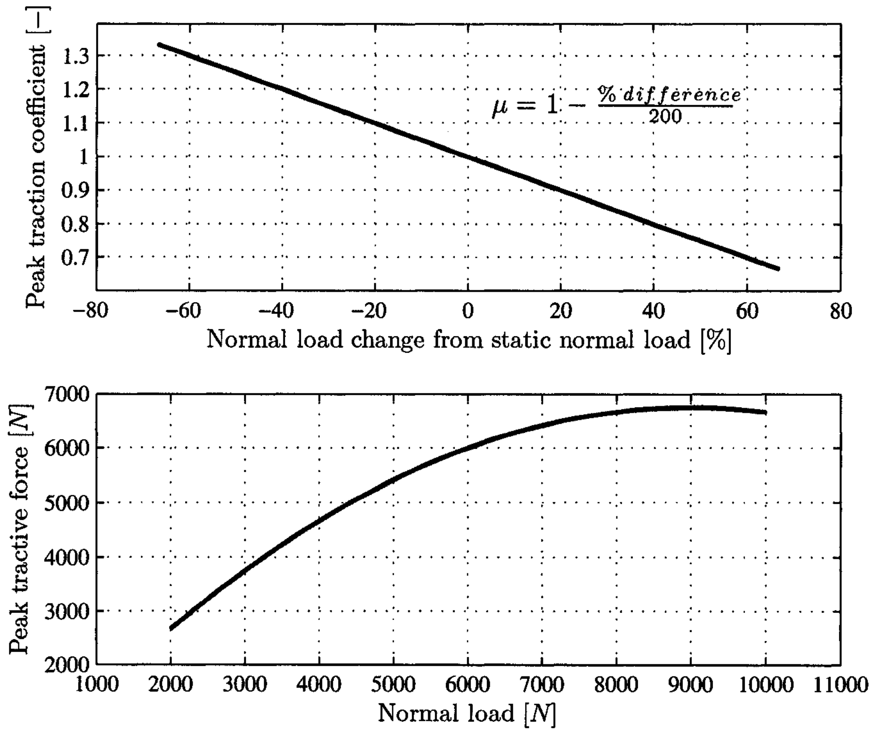

Figure 6.21: *Tire load sensitivity: μ trend and peak tractive load trend (exaggerated values).* The μ curve displays the predicted trend, that traction coefficient decreases linearly with percentage change above a nominal tire load. The resulting change in tractive force capability is also shown.

resulting trend will change. There is no way to create a universal trend based on percentage change in normal load, which will scale perfectly to all tires.

For the CarSim large sedan vehicle model, the static normal load on each front tire is 5155 N, and the static normal load on each rear tire is 3214 N. The nominal normal load was chosen to be the average normal load, 4185 N. The tire load sensitivity was programmed into a Simulink module. The module compares the percentage difference between each tire load and the nominal load. Then a μ value is assigned to each tire based on the trend described above.

6.5 Tire Slip Correction

All vehicles equipped with anti-lock braking will have *wheel speed sensors*, which constantly relay the rotational speed of each wheel to the vehicle computer. Knowledge of the relative

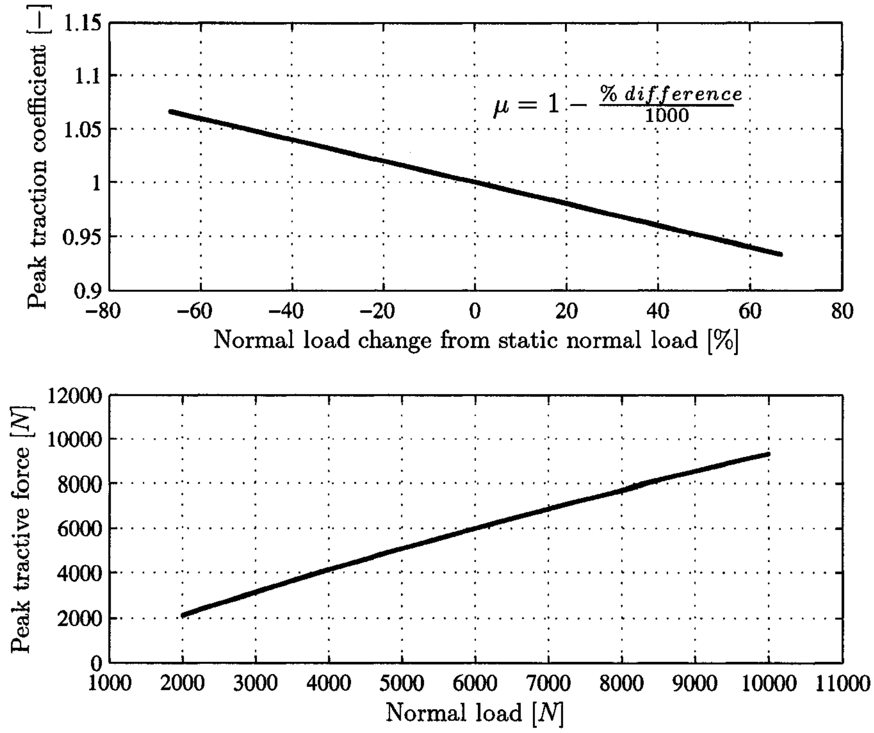

Figure 6.22: *Tire load sensitivity: μ trend and peak tractive load trend (realistic values).* The μ curve displays the predicted trend, that traction coefficient decreases linearly with percentage change above a nominal tire load. The resulting change in tractive force capability is also shown. μ in this case decreases in accordance with the values described by Gillespie [8].

speed of each wheel is extremely useful when operating the vehicle near the limits of traction. During acceleration, a driven wheel that accelerates to a speed much greater than the non-driven wheels is clearly spinning, and power may be reduced to accomplish *traction control.* For an ABS vehicle, a wheel that slows to a stop while the others are still spinning must be *locked up.* Hence, the brake pressure should be cycled off for said wheel, to allow it to spin back up to a useful slip ratio.

Though the *ABP* system should proportion the application of brakes *correctly* for the dynamic state of the vehicle, there are transient effects, and environmental effects, that cannot be predicted by the vehicle computer. Indeed, the number of passengers in the vehicle, relative tire pressures, road conditions, tire wear properties, and other factors can all effect the accuracy of the system. The wheel speed sensor inputs, therefore, may still be used to assist the system.

Rather than measuring wheel speeds after the brakes have been applied incorrectly, and using the feedback to correct what has already become a problem, the brake control system may be programmed to utilize the wheel speeds to constantly augment the proportioning.

For instance, if a vehicle enters a corner and attempts to brake, the system may apply the brakes in what it believes is the *correct* proportions. However, one wheel may slip onto the gravel road shoulder, and have a peak traction coefficient much lower than that predicted by the system. If that wheel speed is observed to slow down (towards lockup), the control system should use the information to correct its original prediction, and decrease braking to the wheel.

A simple *slip correction* algorithm has been written for the brake control module (Equation 6.5.1). If the vehicle is braking only ($throttle = 0$, $brake > 0$), the system reads the wheel speeds, and makes note of the fastest spinning wheel. The pressure to each wheel brake is then scaled up or down relative to its speed difference with the fastest wheel.

$$P_{brake,new,i} = P_{brake,old,i} \cdot \frac{\omega_{wheel,i}}{\omega_{wheel,max}} \tag{6.5.1}$$

where:

$P_{brake,new,i}$ = Augmented brake pressure for wheel i

$P_{brake,old,i}$ = Original controlled brake pressure for wheel i

$\omega_{wheel,i}$ = Rotational speed of wheel i

$\omega_{wheel,max}$ = Rotational speed of fastest wheel

Equation 6.5.1 will yield a 1 for the fastest spinning wheel, and a number less than 1 for each other wheel. The brake proportions are scaled by these percentages, with the pressure to the fastest not changing. Then, all four pressures are re-scaled to produce the same total pressure as before, resulting in an increase in pressure to the fastest wheel.

6.5.1 Offset for front-locking

As stated in Section 5.1, it is imperative to lock the front tires before the rears while braking. Theoretically, the ideal braking situation is to lock all four tires at the same time. In reality, as lockup approaches, one tire will lockup first, followed by another, and so on. To prevent momentary instability, the proportioning should slightly favour the front brakes, to ensure that they still lock up first.

An algorithm to slightly favour the front brakes can easily be programmed into the tire slip correction controller. By offsetting the rear wheel speeds before the values enter the wheel speed controller, the controller may be "tricked". The wheel speeds are reduced, in this instance, by 5 $\frac{km}{h}$. The result is that while the controller attempts to keep all wheels at the same speed, it truly keeps the two rear tires rolling during braking 5 $\frac{km}{h}$ *faster* than the front tires.

This effect may be useful in overcoming some unpredictable situations. While the factor of safety in a typical static brake system, which favours heavily the front brakes, is a burden in normal braking, it also leaves much room for error if the rear tires were to face a sudden reduction in tractive ability. With the brakes closely straddling the optimum distribution, as all four tires approach lockup an unpredicted change in rear tire behaviour could cause them to lock quickly before the computer and hardware can react. The slight front braking offset may help lessen the chance of this situation occurring, by maintaining a slight factor of safety.

6.6 Results: Tire slip correction

It is desired to verify the effectiveness of the slip correction control algorithm presented in Section 6.5. The purpose of the system is twofold. Firstly, by constantly measuring wheel speeds and adjusting the brake pressure away from the slowest tires, the slip correction algorithm will compensate for unforeseeable conditions. Secondly, the slip correction system utilizes knowledge of wheel speeds to ensure that the front tires lock up before the rears. Although the active proportioning system should theoretically use traction equally at each tire, causing simultaneous lockup, in reality tires will lock one at a time. It is desired to ensure that the front tires always lock first.

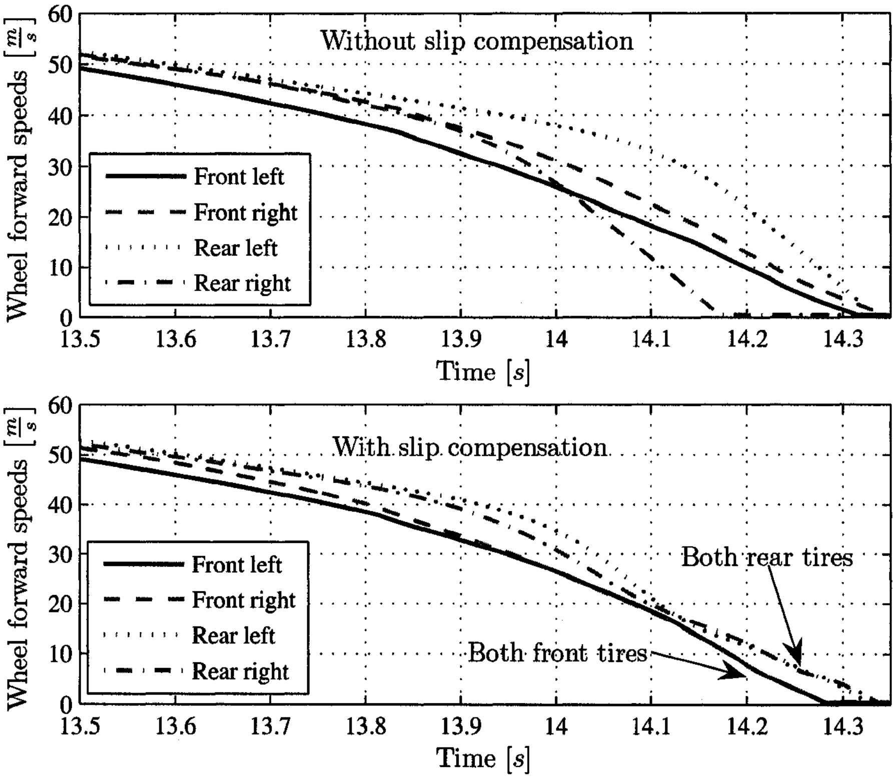

Figure 6.23: *Tire lockup order during braking, vehicle with slip compensation vs. vehicle without slip compensation.* The addition of the slip compensation algorithm ensures that no individual tire is overbraked, in the event of an unforeseen loss of traction. Further addition of the front brake offset ensures that the front tires lock slightly prior to the rear tires.

The results displayed in Figure 6.23 are for a combined cornering and braking event. The large sedan vehicle model is braked during a corner, to a full stop. The upper plot shows the order of tire lockup (as wheel speeds go to zero) for the controlled (*ABP*) vehicle, with *no slip compensation control.* The lower plot displays the same event for the *ABP* vehicle with the slip compensation control.

As the four wheels slow down towards zero, it is observed that one rear tire actually locks first for the *ABP* vehicle without slip control. The order of locking is *rear right, front left, rear left, front right.* Although the time between lockups is quite small, it is still

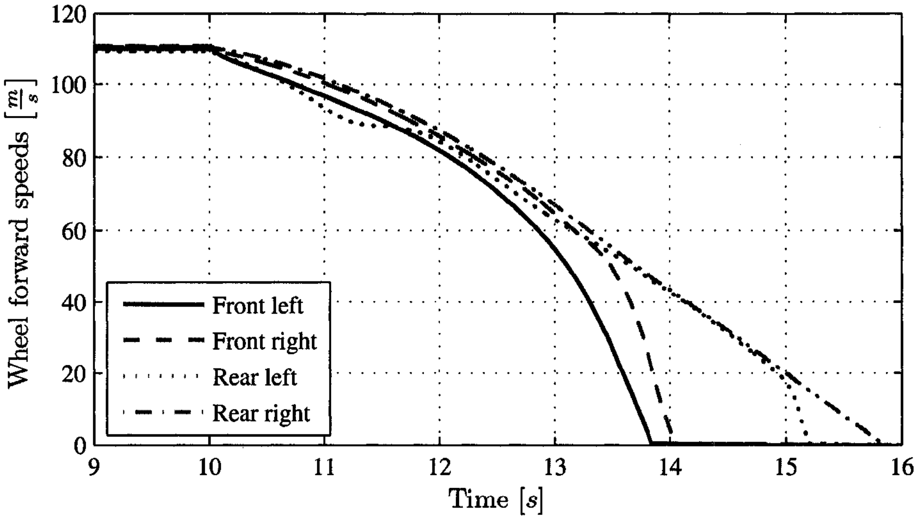

Figure 6.24: *Tire lockup order during braking, baseline vehicle.* The baseline vehicle undergoes the same braking maneuver as the *ABP* vehicles in Figure 6.23. For the baseline vehicle, individual wheels lock up as early as 13.8 *s*.

desirable that the front tires lock first. For the slip controlled vehicle, it is shown that both front tires lock simultaneously, momentarily before both rear tires lock. It is important to note that the plot displays results for two versions of the *ABP* vehicle. For the baseline vehicle in the same simulation, individual wheels lock up as early as 13.8 *s* (Figure 6.24).

The methodology of ensuring front tire lockup was to trick the slip compensation controller by slightly decreasing the measured values of rear tire velocities in the controller. As a consequence, throughout the braking event shown in the plot, it is seen that the rear tires are kept at a speed slightly higher than the front tires.

6.7 Brake control system operation overview

The control design described in this chapter can be considered a *true optimal* predictive brake proportioning system. The forces to brake the vehicle are applied in proportions directly appropriate to the tractive ability of each tire.

An overview of the control system algorithm is presented:

1. Vehicle properties

- The control system must be programmed with nominal (expected or average) values for many vehicle properties:
    - Vehicle mass
    - Vehicle track width and wheelbase
    - Wheel mass and rotational mass moment of inertia
    - Tire radius
    - Tire vertical stiffness
    - Front / rear coil spring stiffness and anti-roll bar stiffness
    - Front / rear weight distribution
    - Vehicle CG height
    - Front / rear static roll centre heights

2. Sensor inputs
    - One lateral accelerometer and one longitudinal accelerometer continually measure the vehicle's accelerations.
3. Tire load prediction
    - Use acceleration values and vehicle properties to estimate vertical load on each tire
4. Braking capability prediction
    - Use expected trend in tire load sensitivity to predict tractive ability of each tire, based on normal load
5. Apply brake forces in proportion to predicted braking capability
6. Correct for tire slip
    - Observe measured tire speeds, to ensure that each tire is approaching lockup at the same time
    - An unforeseen loss of traction on some wheels, such as a small patch of ice, would be detected
    - Decrease braking to locking-up tires, and increase to free-rolling tires

Chapter 7

Steering effects of brake control

Modern vehicle stability control and path control systems distribute tire forces by braking or driving the wheels, in order to control the path of the vehicle. In an emergency braking situation, however, the primary goal must be stopping the vehicle as quickly and safely as possible. If brake forces or driving forces are being modulated to correct the vehicle path, they may not be optimally applied for slowing the vehicle. Thus, in order to ensure optimal braking, the brake forces should be distributed according to the optimal brake force distribution, and all available traction should be used for braking. Consequently, it must be investigated what effects the brake forces may have on the path of the vehicle. If braking forces are to be applied without reservation, it must be verified that the proportioning of the forces will not adversely affect the ability of a driver to keep the vehicle on the road.

7.1 Forces on a cornering vehicle

The forces at the tire-road interface are wholly responsible for accelerating the vehicle: longitudinal forces for driving and braking accelerations, and lateral forces for accelerating in a corner. Recalling the Bicycle Model (Figure 4.2) representation derived in Section 4.2.1, the lateral acceleration of a vehicle is given by Equation 7.1.1.

$$a_{lateral} = \dot{v} + r \cdot u \tag{7.1.1}$$

where:

$$\dot{v} = \text{Rate of change of vehicle lateral velocity } \left[\frac{m}{s^2}\right]$$
$$r = \text{Vehicle yaw rate } \left[\frac{rad}{s}\right]$$
$$u = \text{Vehicle forward speed } \left[\frac{m}{s}\right]$$

Thus, the lateral acceleration expressed in body-fixed coordinates is the result of both lateral sliding speed (caused by lateral tire forces) and the vehicle yaw rate (caused by yaw moments). Any tire lateral forces will generate an acceleration by Equation 7.1.2, made up of some proportions of lateral sliding acceleration and yaw rate.

$$\sum F_{lateral} = F_{lateral,\, front} + F_{lateral,\, rear} = m \cdot a_{\,lateral} = m\,(\dot{v} + r \cdot u) \qquad (7.1.2)$$

Any longitudinal or lateral tire forces acting at a distance from, and not directed at, the CG, will create a yaw moment (Equation 7.1.3), which will in turn develop a vehicle yaw rate, which contributes to the lateral acceleration according to Equation 7.1.1.

$$\begin{aligned}\sum M_{yaw} =& F_{lateral,\, front} \cdot a - F_{lateral,\, rear} \cdot b \\ & + F_{longitudinal,\, left} \cdot \frac{T}{2} - F_{longitudinal,\, right} \cdot \frac{T}{2} \\ =& I_{yaw} \cdot \dot{r}\end{aligned} \qquad (7.1.3)$$

where:

$$\sum M_{yaw} = \text{Yaw moments on the vehicle}$$

It is the intention of this chapter to examine how the proposed active brake proportioning system may contribute to the forces and moments which cause vehicle lateral acceleration, and how any resulting lateral accelerations may affect vehicle drivability.

7.2 Steer by steered wheels

Whenever a tire is required to create lateral forces under cornering conditions, the tire contact patch will experience a slip angle as it rolls. Recall from Section 3.2 that slip angle is the difference between the steered angle of a wheel and the actual direction of travel of its tire.

In the linear region of the tire lateral force versus slip angle curve (Figure 3.7), the lateral tire force can be approximated as a linear function of tire slip angle (Equation 7.2.1) [8].

$$F_{lateral} = C_{\alpha} \cdot \alpha \tag{7.2.1}$$

where:

C_{α} = tire cornering stiffness

α = tire slip angle

7.2.1 Steering forces in steady-state cornering

Considering the bicycle model representation of a vehicle, cornering at steady-state (no transient effects), an analysis can reveal the effects of the driver steering inputs.

For a vehicle cornering on a turn of constant radius, R, and at forward velocity, u, the lateral acceleration is given by Equation 7.2.2 [12].

$$a_{lateral} = \frac{u^2}{R} \tag{7.2.2}$$

where:

R = turn radius

For steady-state cornering, the force balance equation is the same as given in Equation 7.1.2, but because the yaw rate is constant, the moment balance must sum to zero (Equation 7.2.3).

$$\sum M_{yaw} = F_{lateral,\ front} \cdot a - F_{lateral,\ rear} \cdot b = 0 \tag{7.2.3}$$

The slip angles of the tires can be solved by rearranging Equations 7.2.2, 7.2.1 and 7.1.2 [8]:

$$\alpha_f = \frac{u^2 \cdot W_f}{C_{\alpha,f}\; g\; R} \qquad\qquad (7.2.4)$$
$$\alpha_r = \frac{u^2 \cdot W_r}{C_{\alpha,r}\; g\; R}$$

where:

W_f = static weight on front axle

W_r = static weight on rear axle

From Figure 7.1 it can be derived that the steer angle is related to the wheelbase, cornering radius, and tire slip angles by Equation 7.2.5.

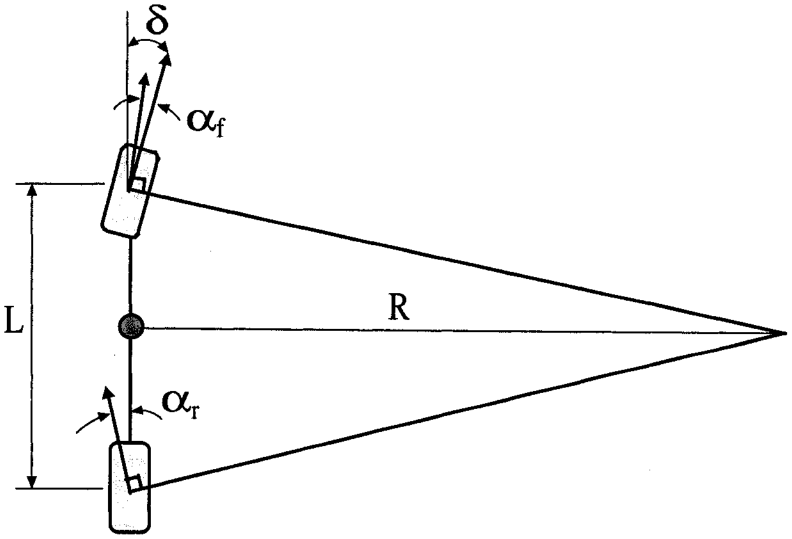

Figure 7.1: *Cornering bicycle model: steer angle and tire slip angles.* For a bicycle model vehicle representation undergoing steady-state cornering, the steer angle and tire slip angles are shown.

$$\text{Steer angle } = \delta = \frac{L}{R} + \alpha_f - \alpha_r, \;\; [rad] \qquad (7.2.5)$$

Combining Equations 7.2.4 and 7.2.5, the final steady-state steer angle equation can be derived (Equation 7.2.6).

$$\delta = \left(\frac{180}{\pi}\right)\frac{L}{R} + \left(\frac{W_f}{C_{\alpha,f}} - \frac{W_r}{C_{\alpha,r}}\right)\frac{u^2}{g\,R}, \;\; [deg] \qquad (7.2.6)$$

The steer angle equation can be conveniently plotted in 3D contour form (Figure 7.2). Assuming constant tire properties, the steer angle is a function of both cornering radius and forward speed. At a constant forward speed, a changing road radius will require a change in steer angle. Likewise, with a constant radius, changing the vehicle speed (i.e. braking) will require a change in steer angle.

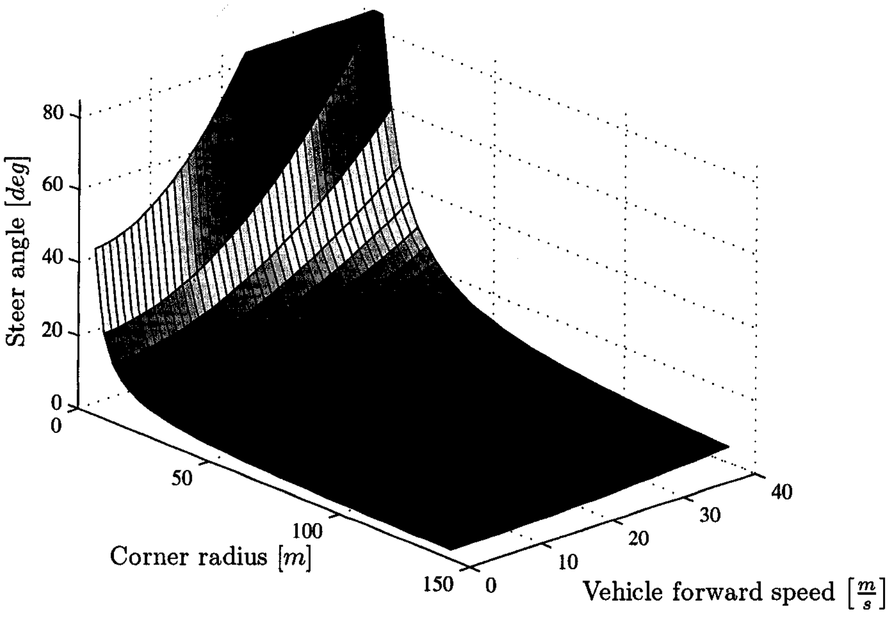

Figure 7.2: *Steer angle versus vehicle forward speed and corner radius.* The equation for steady state steer angle can be plotted versus changes in both vehicle speed and turn radius. The 3D contour plot clearly shows that increasing steer angle is required for tighter radius turns, or faster vehicle speeds.

These equations reveal that for a given vehicle, the steer angle is expected to consistently change during cornering, based on cornering radius and forward speed. Furthermore, the prediction of the steering angles or steering relies on knowledge of tire cornering stiffnesses.

The changes required in steering angle on a vehicle undergoing changes in cornering radii and forward speeds are not disturbing to drivers, but rather are an unnoticed aspect of everyday driving. If the steering requirements of the *ABD*-equipped vehicle lie in the same range of steer angles and steering wheel rates that drivers are known to be capable of dealing with in normal vehicles, it can be concluded that the *ABD* system does not create unsafe steering effects.

7.3 Steer by laterally uneven brake forces

For the case of a typical vehicle undergoing braking (Figure 7.3, case A), the braking forces on the inside and outside of the vehicle contribute only longitudinal forces (ignoring the small lateral components of the braking forces on the steered wheels). Any moment created by the inside brakes is equally opposed by the moment created by the outside brakes. For the case of actively proportioned brakes (Figure 7.3, case B), the braking forces on the outside tires are larger. The forces, acting at a distance of half the track width, create a resultant yaw moment (M_{brake}) about the vehicle *CG*.

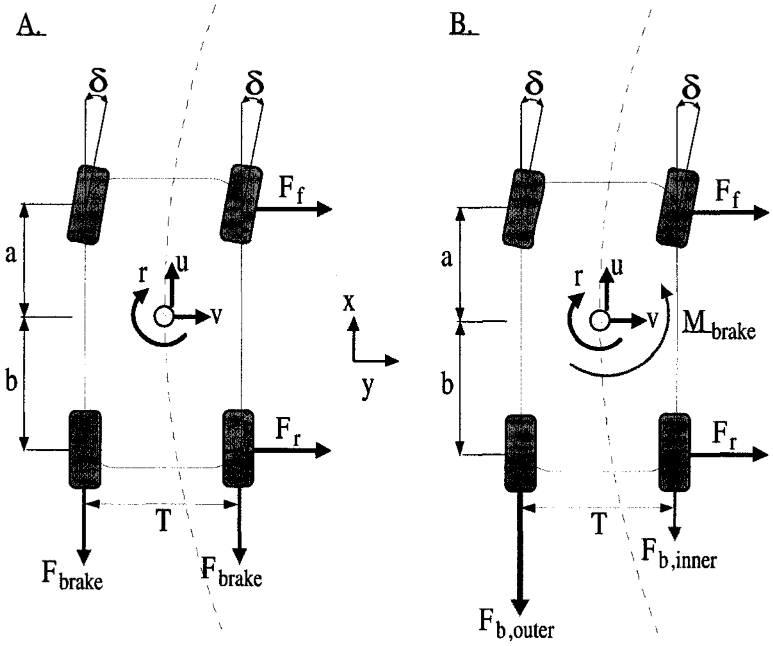

Figure 7.3: *Braking and cornering forces with (A) and without (B) ABP.* The braking forces on a cornering vehicle are displayed, for both baseline and *ABP* vehicles. A vehicle yaw moment M_{brake} is created by the laterally uneven braking forces on the *ABP* vehicle.

To verify the yawing effect of laterally proportioned braking forces, a simulation was performed. The CarSim large sedan vehicle model braking in a straight line was programmed to apply the brakes such that twice the braking force was applied to one side of the vehicle. Figure 7.4 clearly shows the steering effect of the uneven braking force. The straight forward direction is the vertical axis, and lateral offset from the straight forward path is the horizontal axis. The vehicle undergoing braking steers continually laterally away from the forward direction throughout the simulation.

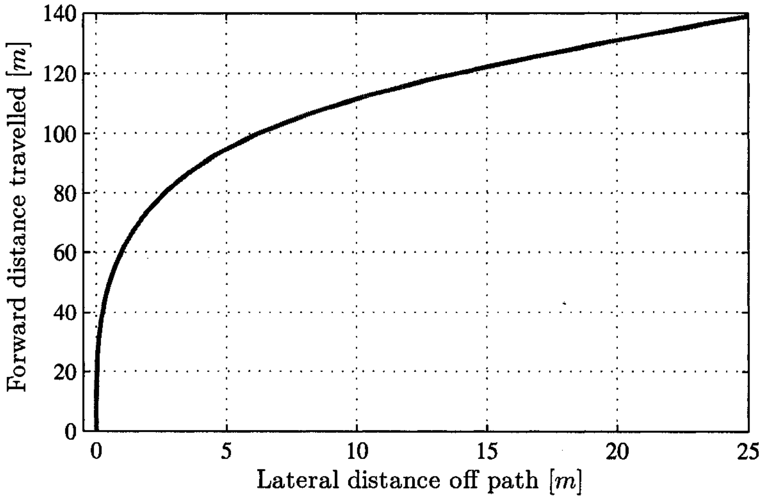

Figure 7.4: *Simulation of steering effect of laterally proportioned braking forces.* Straight line braking results for the large sedan vehicle model, with uneven braking forces on each side of the vehicle. The laterally proportioned braking forces create a yawing moment which steers the vehicle off the path.

Lateral brake proportioning will always act to increase the braking forces on the outside tires during cornering. Therefore, the yaw moment created by lateral brake force proportioning will always act as an *understeering* yaw moment (Figure 7.5). That is, the moment will turn the car as if to straighten out the vehicle's path, or cause the vehicle to drive straight through a corner. This moment will oppose the moment created by the steering efforts of the driver, which serve to increase the vehicle *turn-in.* The understeering moments due to lateral brake proportioning will increase the required steering wheel angle during combined braking and cornering, relative to a typically braked vehicle.

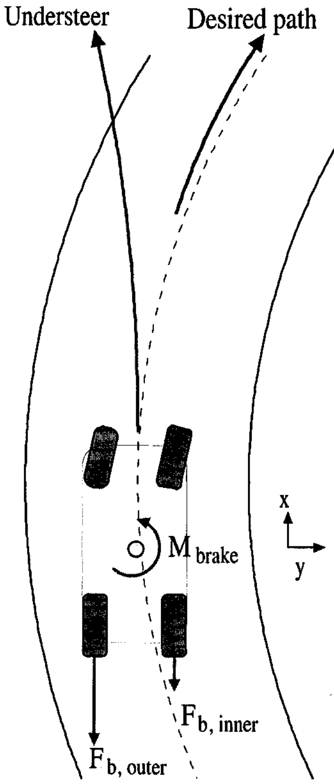
Understeer
Desired path
x
y
M brake
F b, inner
F b, outer

Figure 7.5: *Vehicle path change caused by laterally proportioned brake forces.* The load transfer during cornering implies that more braking force (with actively proportioned braking system) will always be applied to the outside tires. The resulting yaw moment on the vehicle will always cause the vehicle to *understeer.*

7.4 Steering effect simulations

In order to investigate the change in driving experience, and driver steering requirements, due to actively proportioned braking forces, a series of simulations were carried out. The simulations were performed on the CarSim large sedan vehicle model, undergoing combined cornering and braking.

For each simulation, the built-in CarSim driver model is allowed to control the steering wheel input to the vehicle. The driver model, as described in Section 4.3.4, attempts at all times to keep the vehicle directly on the prescribed path. Realism is provided by means of a response delay time, and a limited look-ahead distance.

7.4.1 Cornering and braking to a full stop

For the first simulation the vehicle undergoes steady-state cornering at 110 $\frac{km}{h}$ on a curve of radius 152 m. During the steady-state cornering, the vehicle experiences a lateral acceleration of 0.625 g. After 10 seconds of cornering, the brakes are applied, with a tri-linear ramping master cylinder brake pressure of approximately 1.5 $\frac{MPa}{s}$ (Figure 7.6).

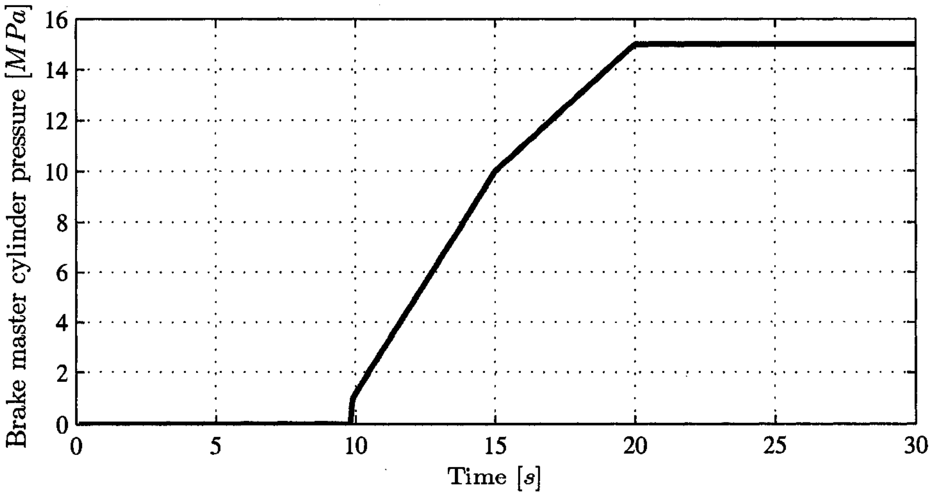

Figure 7.6: *Master cylinder brake pressure for brake-steer simulations.* The master cylinder brake pressure is applied during the steady-state cornering maneuver. The pressure is distributed based on static proportioning for the baseline vehicle, or active proportioning for the *ABP* vehicle.

The master cylinder pressure is applied with static proportions (70% front, 30% rear) on the baseline vehicle. On the *ABP* vehicle, the pressure is distributed actively based on the dynamic state of the vehicle.

7.4.1.1 Results - steering wheel angle

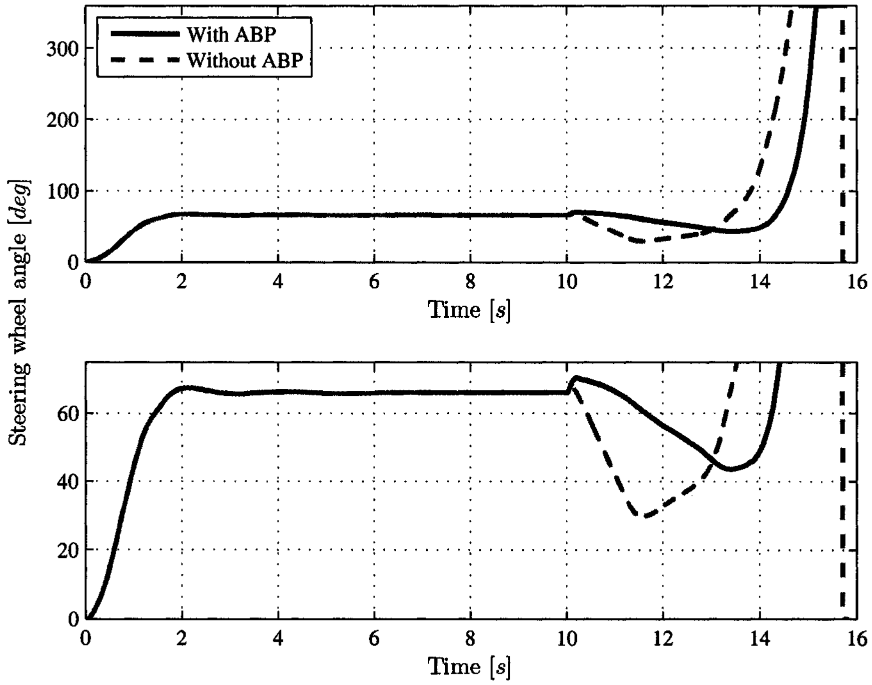

Figure 7.7: *Steering wheel angle - baseline versus ABP vehicle.* The difference in steering wheel angle required by the driver model to keep the vehicle on the specified path is displayed, for a typical vehicle and a vehicle with active brake control. The upper plot displays the full range of wheel angle, including when tire lockup occurs. The lower plot is zoomed in for detail.

Figure 7.7 displays the steering wheel angle, as controlled by the driver model, for the first braking simulation. The upper plot displays the full range of steering wheel angle, including when the steered tires lock up and the steer angle goes to 360 degrees. The lower plot is zoomed in to more clearly show the steering wheel angle as the brakes are applied.

For the baseline vehicle, the driver is required to begin decreasing the steer angle as soon as the brakes are applied, at time 10*s*. This can be explained by the relationship detailed in Section 7.2. As vehicle speed decreases, so too must steering wheel angle.

For the *ABP* vehicle, the brakes are applied immediately with more brake force on the outside tires. The understeering yaw moment must be corrected initially by a positive (into the turn) increase in steering wheel angle. The increase in steer angle, relative to the baseline vehicle, represents an offset required to counteract the yaw moment caused by the braking forces. Throughout the remainder of the pre-lockup deceleration ($10 - 12\,sec$), the steer angle for the active system is greater by an offset appropriate to counteract the braking moment. Braking pressure (and likewise the magnitude of the braking moment) increases throughout the braking period according to Figure 7.6, hence the offset grows.

7.4.1.2 Results - steering wheel torque

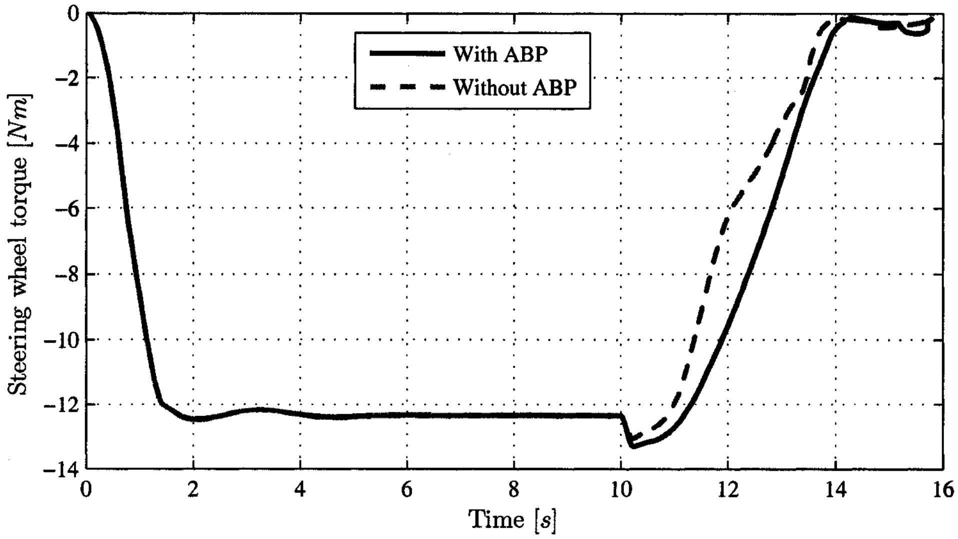

Figure 7.8: *Steering wheel torque - baseline versus ABP vehicle.* The difference in steering wheel torque required by the driver model to keep the vehicle on the specified path is displayed, for a typical vehicle and a vehicle with active brake control.

An investigation of the torque which the driver must supply at the steering wheel (Figure 7.8), reveals only small differences between the baseline and *ABP* vehicles. For both vehicles, a small torque spike occurs when braking begins. Through the remainder of the braking maneuver, the magnitudes of the torques required by the driver are similar, with a slightly larger torque required for the larger steer angle of the ABP vehicle. The torque curve throughout the deceleration remains nearly linear for the ABP vehicle, while the baseline vehicle shows some oscillation.

7.4.1.3 Discussion

It has been shown that for a typical vehicle undergoing braking while cornering, the steering effects due to laterally uneven braking forces produce moderate changes in steer angle requirements. Simulations were also performed with lower cornering speeds, lower brake application pressures, and with a rear-weight biased vehicle. Under all examined circumstances, the results showed similar or lesser differences between the ABP vehicle and the baseline vehicle.

7.4.2 Cornering at 110 $\frac{km}{h}$ and braking to 80 $\frac{km}{h}$

The results for for the baseline vehicle in the first simulation imply that the steering wheel angle decreases as the vehicle speed decreases, in agreement with the steady state steering angle calculations (Equation 7.2.6). The steering wheel angle for the ABP vehicle is at all times larger, presumably to compensate for the braking force yaw moment. In the absence of braking moments then, it is suspected that the steering angle for the ABP vehicle is inappropriately large for the radius of curvature and forward velocity of the vehicle. The braking moment offsets the extra steering forces, and keeps the vehicle on the path. However, the driver is free at any time to remove his foot from the brake pedal, and consequently eliminate the brake forces and moment. With a sudden absence of braking moments, the steering angle may be too large for the vehicle path and speed, and result in a sudden oversteering acceleration.

To investigate the possibility that removing brake pressure during a braking and cornering maneuver may cause steering instabilities, a further set of simulations were performed. The vehicle again undergoes steady-state cornering at 110 $\frac{km}{h}$ on a curve of radius 152 m (lateral acceleration of 0.625 g). After 10 seconds of cornering, the brakes are applied, with a tri-linear ramping master cylinder brake pressure of approximately 1.5 $\frac{MPa}{s}$ (Figure 7.6).

After 12.3 seconds, the brake pressure is set to zero, to simulate a driver quickly removing all effort from the brake pedal.

7.4.2.1 Results - steering wheel angle

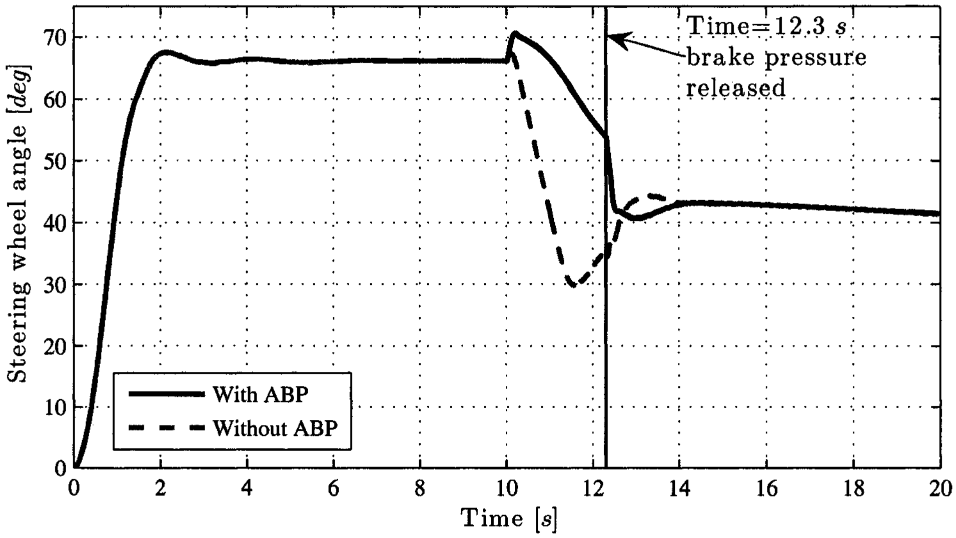

Figure 7.9: *Steering wheel angle - baseline versus ABP vehicle: Braking* 110 $\frac{km}{h}$ *to* 80 $\frac{km}{h}$. The difference in steering wheel angle required by the driver model to keep the vehicle on the specified path is displayed, for a typical vehicle and a vehicle with active brake control.

Figure 7.9 displays the steering wheel angle results for the baseline and ABP vehicles, for the partial braking maneuver. The suspected result was that the steering wheel angle of the ABP vehicle would be poorly prepared for the cornering conditions of the vehicle when the brakes were released. However, the results show that both vehicles differ from the steady-state steer angle by approximately the same amount.

The brake pressure is set to zero at 12.3 seconds, and both vehicles settle on the same steady-state steer angle, $\sim 43\ deg$, by 14 seconds. Before the brakes are released, the ABP vehicle's steer angle is $\sim 10°$ larger than the steady-state steer angle, while the non-ABP vehicle's steer angle is $\sim 10°$ smaller than the steady-state steer angle.

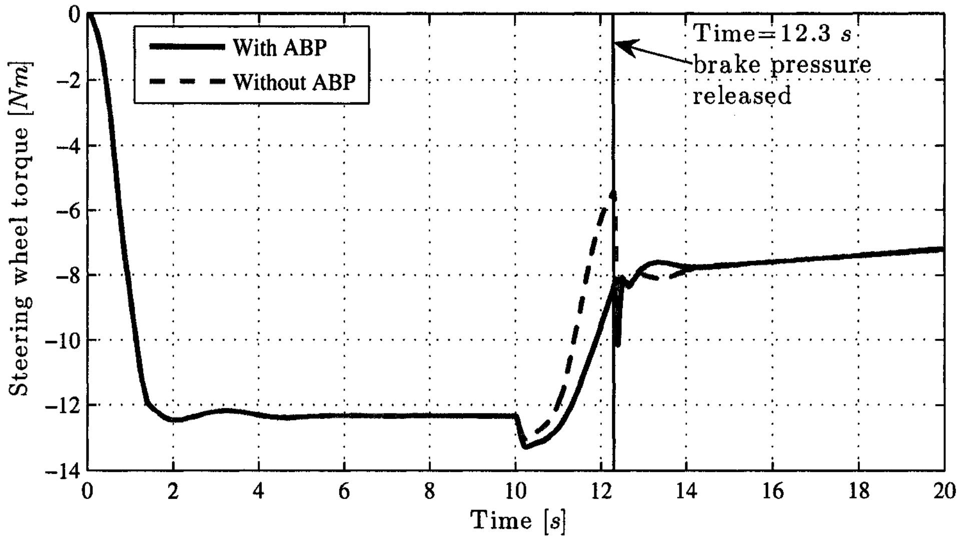

Figure 7.10: *Steering wheel torque - baseline versus ABP vehicle, braking* 110 $\frac{km}{h}$ *to* 80 $\frac{km}{h}$. The difference in steering wheel torque required by the driver model to keep the vehicle on the specified path is displayed, for a typical vehicle and a vehicle with active brake control. The peak torque is larger for the *ABP* vehicle, but the peak required rate of change of torque is largest for the baseline vehicle.

7.4.2.2 Results - steering wheel torque

An investigation of the torque required by the driver at the steering wheel (Figure 7.10) again shows only moderate differences between the baseline and *ABP* vehicles. When braking begins at time 10 seconds, both steering wheel torques experience a small spike, though the *ABP* vehicle shows the largest torque. When the brake pressure is released at 12.3 *s*, the steering wheel angle must be quickly adjusted to a new steer angle, resulting in a steering wheel torque spike. This spike is considerably smaller for the *ABP* vehicle.

The torque spike was larger for the non-*ABP* vehicle, because the torque before 12.3 *s* was significantly larger for the non-*ABP* vehicle. This was likely because the steering wheel was being turned (i.e. had a rate of change) at that time. On the *ABP* vehicle, the steering wheel was only being held steady, and so had a smaller torque value, closer to the steady-state value.

7.4.2.3 Discussion

Based on the steady-state steer angle after the brakes are released, it can be concluded that for the baseline vehicle, the steer angle is *smaller* at each speed than would be expected during steady-state cornering. Likewise, for the *ABP* vehicle, the steer angle is *larger* at each speed than would be expected during steady-state cornering. For this reason the steering wheel angle must be modified on both vehicles when the brake pressure is released. The magnitude of the required change is not significantly different between the non-*ABP* and the *ABP* vehicles.

The steering torque does not show significant differences between the *ABP* and non-*ABP* vehicles. The torque before the brakes are released is larger on the baseline vehicle, because the wheel was being turned at that time. As a result, the baseline vehicle showed a larger required rate of change of torque when the brakes were released.

7.5 Discussion of results

Proportioning the braking forces on a vehicle in order to produce laterally uneven braking forces will subject the vehicle to a yaw moment. Due to the nature of load transfer during cornering, the moment will always act to understeer the vehicle, or increase the turning radius. This moment must be opposed by a higher than normal steering wheel angle, relative to the same maneuver in a vehicle with a typical brake system.

The steering wheel angle in steady-state cornering can be approximated, for a simplified vehicle model, as the contour plot shown in Figure 7.2. For an understeer vehicle, the required steer angle increases with increasing vehicle velocity, and decreases with increasing radius of turn. For the *ABP* vehicle with proportioned brakes, the steer angle becomes a function also of master cylinder brake pressure (Equation 7.5.1).

$$\begin{aligned} \delta_{baseline\,vehicle} &= f\left(velocity,\ radius\right) \\ \delta_{active\,braking\,vehicle} &= f\left(velocity,\ radius,\ brake\,pressure\right) \end{aligned} \tag{7.5.1}$$

The steer angle of the *ABP* vehicle with no braking will be the same as for a non-*ABP* vehicle. When brakes are applied, the brake forces create a moment, and the moment changes the required steer angle. The magnitude of the moment applied is a function of load transfer (lateral acceleration), and of master cylinder pressure.

The *ABP* system applies more rear brakes, and less front brakes, relative to the baseline vehicle. Increasing the rear brake force decreases the rear lateral (cornering) force, for the slip angle at the moment the brakes are applied. Under a typical situation, this may lead to oversteering instability, as the reduction in rear axle traction causes the vehicle to yaw out of control, but the *ABP* brake forces creates an understeering yaw moment that keeps the vehicle stable. The understeering yaw moment implies that more steer angle would be required, but the reduction of rear cornering traction implies that less steer angle would be required to keep the vehicle stable. The result is that the steer angle for the *ABP* vehicle under braking is only slightly larger than the steady-state steer angle for a given speed.

Clearly, the yaw moment created by laterally offset braking forces will affect the motion of an automobile. The driver of the *ABP* vehicle must change his steering in reaction to the moments applied to the vehicle, in order to drive on the desired path. The required changes in steering due to the braking moments were seen to be on the same order of magnitude as changes in steering experienced in driving a conventional vehicle, due to transient effects and normal driving dynamics. In the simulation of braking from 110 $\frac{km}{h}$ to 80 $\frac{km}{h}$, the simulations showed that the driver of the *ABP* vehicle was able to follow the path with less rapid changes in steering wheel angle, and less rapid changes in steering wheel torque, relative to the baseline vehicle. At the very least, any changes in vehicle motion imposed by the braking forces of the *ABP* system are within the range of disturbances which can be tolerated by a typical driver.

Chapter 8

Braking Simulations

It was desired to perform a series of simulations to evaluate the effectiveness of the active brake proportioning control system. For consistency, all simulations were performed on the modified CarSim large sedan vehicle model (Appendix A). To keep the results to a reasonable breadth, the simulations were limited to this one vehicle type only. However, the effectiveness of the load predictive control system was previously verified on an additional vehicle model, representing a mid-sized *crossover* vehicle (Appendix B).

8.1 Overview

Each simulation was performed in CarSim. Simulations of the *baseline* vehicle, without *ABP*, were performed internally in CarSim on a sedan vehicle with a typical brake system. The simulations for the vehicle with *ABP* were performed using CarSim and Simulink co-simulation. At each simulation time-step, the vehicle accelerations and driver brake pedal input were exported to Simulink, where the proportion of brake pressure to each wheel was calculated, and exported back to the CarSim vehicle model.

For the simulations of ABS-equipped vehicles, CarSim / Simulink co-simulation was used for both the non-*ABP* and *ABP* vehicles. The ABS model was designed to represent a 4-channel ABS system, meaning that the pressure can be cycled at all four wheels individually. For each wheel, at each time step, the slip ratio is calculated (Equation 3.2.1). When the slip ratio at a wheel rises above 15%, the brake to that wheel is turned off. When the slip ratio recovers as low as 5%, the brake is turned back on. There is no delay programmed into the controller, so the cycle time of the system is determined by the vehicle and tire dynamics (i.e. how fast the wheel will accelerate and decelerate between 5% and 15% slip).

Each simulation was constructed to examine a braking event in which the limits of traction will likely be exceeded, in at least one of the vehicle models. Specifically, it was attempted to make the braking in each simulation severe enough to cause at least one tire to lock up in the baseline vehicle. The same simulation performed on the *ABP* vehicle would ideally show improvement in stopping distance, driver steer requirements, or vehicle path following ability. The baseline and *ABP* vehicle models are identical in all ways except the brakes applied to each wheel.

Furthermore, it was attempted to make each braking simulation representative of a realistic situation that would be considered safety critical. The situations are such that improved braking ability, or steerability, may play a major role in preventing an accident.

8.2 Straight-line braking

The first, and most simple, simulation is braking to a stop while driving in a straight line. The simulation may be interpreted as a situation in which a driver observes an oncoming obstacle, and rapidly applies increasing brake pressure to attempt to bring the vehicle to a stop. Straight line braking is an extremely important aspect of everyday driving. Occasional emergency stops will occur, during which the highest level of possible straight line deceleration is desired.

In each straight-line braking simulation, the vehicle initially cruises at 210 $\frac{km}{h}$ in a straight line, with zero throttle. After 10 seconds, the vehicle speed is reduced to 200 $\frac{km}{h}$ due to engine-braking and driveline inefficiencies. Aerodynamic effects are neglected. The vehicle brakes are applied according to Figure 8.1, with no brake pressure up until time $10s$, and a linear rise up to $30\,MPa$ after $10\,s$. The baseline vehicle uses a brake proportioning

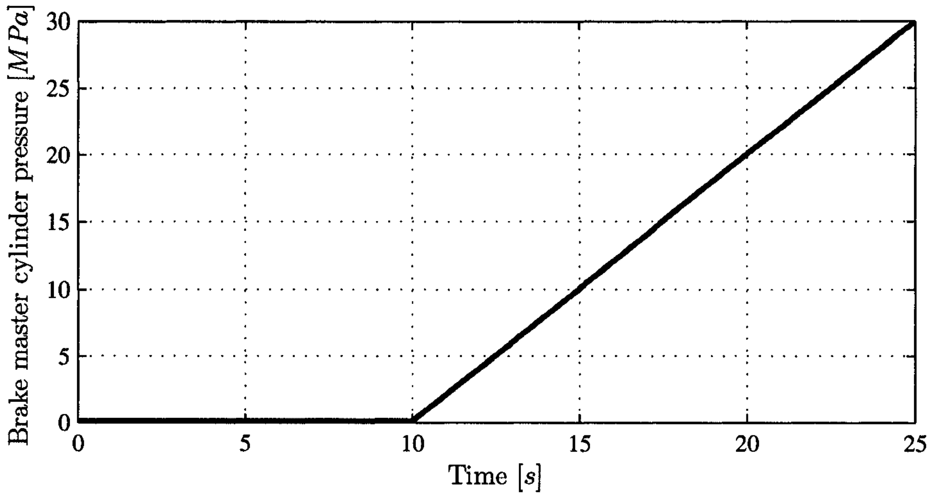

Figure 8.1: *Master cylinder brake pressure curve for straight line braking.* The brake pressure applied to the brake master cylinder during straight line braking simulations. Starting at ten seconds, pressure increases linearly to 30 MPa.

ratio, Φ, of 0.23. This means that for any unit of brake pressure demanded by the driver at the master cylinder, 70% goes to the front axle, and 30% to the rear axle (Equation 5.6.1). The *ABP* vehicle distributes the master cylinder pressure to each wheel following the control methods described in Chapter 6.

8.2.1 Straight-line braking: Non-ABS vehicles

Table 8.1: *Straight line braking (no ABS): Simulation results summary*

Vehicle model	Stopping time	**Change**	Position
Baseline	10.12 s		on path
ABP	10.07 s	-0.5 %	on path

The first simulation compares the straight line braking performance of the baseline vehicle and the *ABP* vehicle, both without anti-lock brakes. An overview of the final state of the vehicles is presented in the Table 8.1. The *ABP* vehicle stops slightly faster than the baseline vehicle (0.5 % reduction in stopping time), while both vehicles remain perfectly on the straight line path.

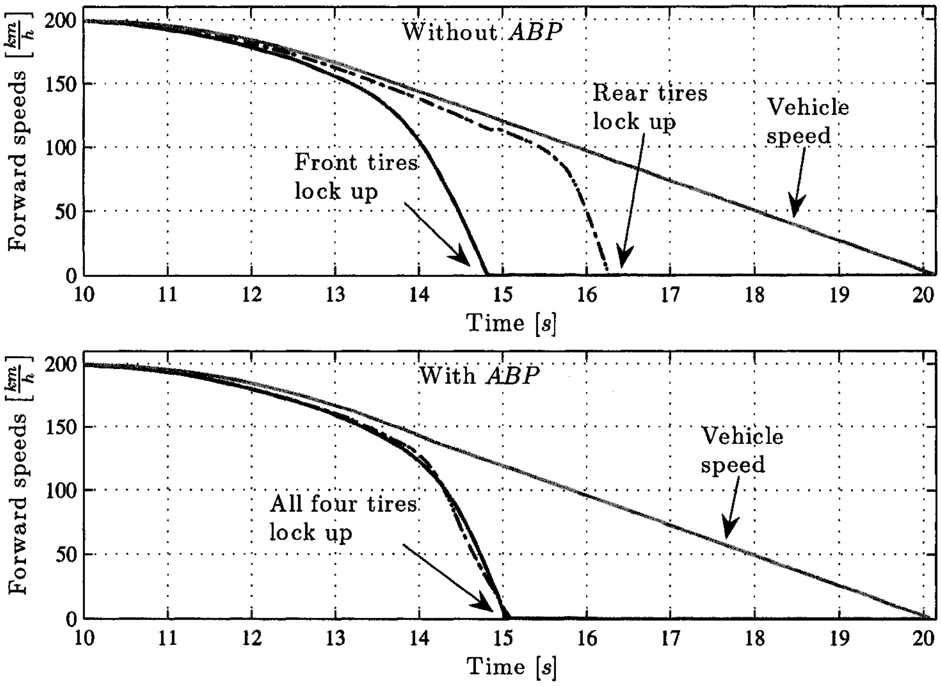

Figure 8.2: *Straight line braking (no ABS): Vehicle and wheel speeds.* The vehicle speed and wheel speeds are shown during the braking event, for the baseline vehicle (upper plot) and *ABP* vehicle (lower plot). The static brake proportioning on the baseline vehicle results in front lockup long before rear lockup, while the *ABP* vehicle causes all tires to lock simultaneously.

The vehicle speeds during the braking event are presented in Figure 8.2. Due to the large proportioning of front axle braking on the baseline vehicle, the front tires lock shortly after braking begins. The rear brakes lock approximately 1.5 seconds later. On the *ABP* vehicle, however, the brake pressure is modulated based on the measured deceleration. The effectiveness of the system in utilizing equal traction at all tires is shown by all four tires locking at approximately the same time. All four tires lock on the *ABP* vehicle later than the front tires lock on the baseline vehicle.

The brake pressures applied during the straight line braking event are displayed in

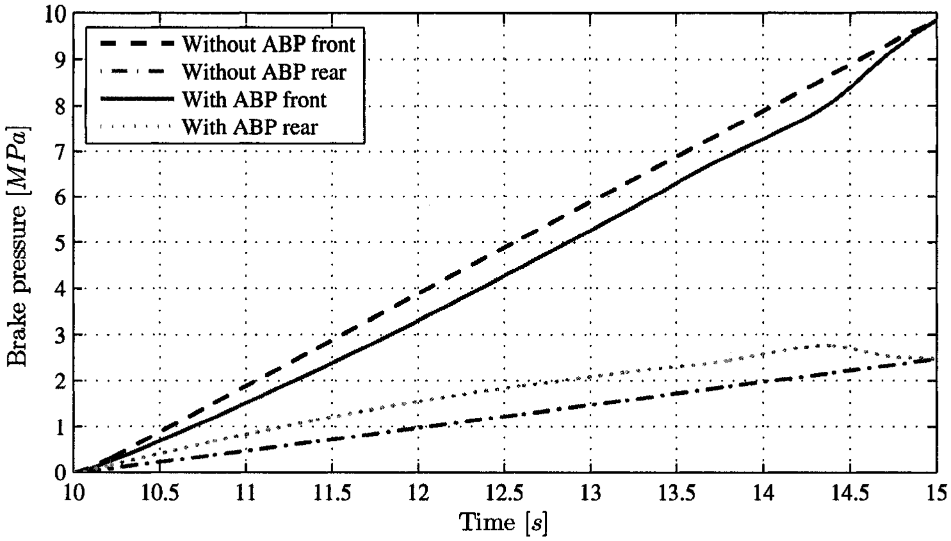

Figure 8.3: *Straight line braking (no ABS): Brake pressure.* The brake pressure to both the front and rear axles during the straight line braking event is presented. The brake pressures on the baseline vehicle simply follow a percentage of the master cylinder pressure, while the *ABP* vehicle pressure is a function of vehicle dynamics.

Figure 8.3. The brake pressures on the baseline vehicle are a static distribution of the master cylinder pressure. The *ABP* vehicle brake pressures are proportioned based on vehicle dynamics, and apply more rear braking, relative to the baseline vehicle. Figure 8.4 displays the brake pressure distribution, presented as front pressure versus rear pressure. The proportioning resulting from the *ABP* vehicle closely resembles the shape of the optimal curve from Section 5.4. The brake pressure curve of the *ABP* vehicle applies much more braking to the rear tires. The shape of the braking curve for the *ABP* vehicle suggests that the acceleration based control allows the brakes to closely approximate the true optimal brake curve. This is further enforced by the fact that all four tires on the *ABP* vehicle lock up simultaneously.

As stated in Section 5.4, the optimal braking force curve should provide the maximum *wheels-unlocked deceleration.* In particular, in order to achieve the highest wheels-unlocked deceleration, it was desired to utilize equal amounts of the available traction at the front and rear axles. The longitudinal accelerations (Figure 8.5) verify that the *ABP* vehicle

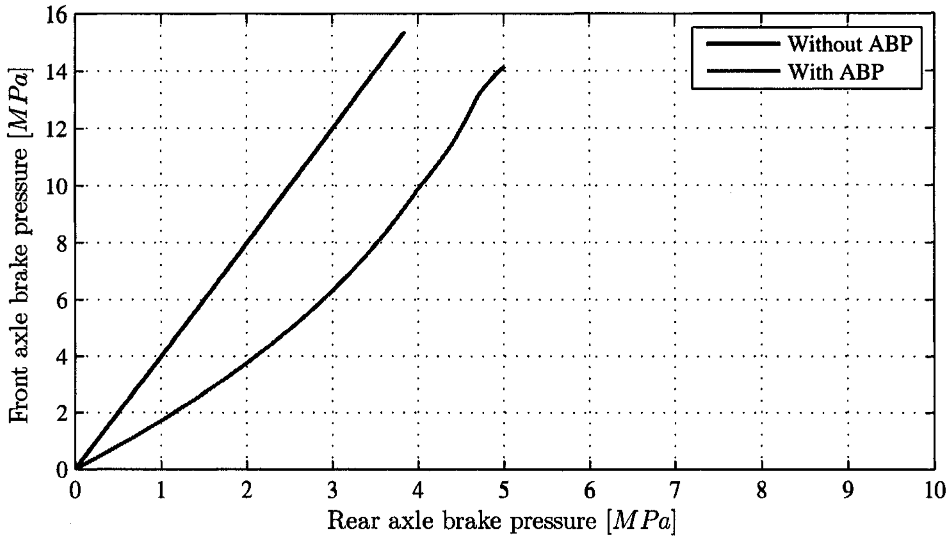

Figure 8.4: *Straight line braking (no ABS): "Braking curve" - front axle braking versus rear axle braking.* The braking curves for the baseline and ABP vehicles are presented. While the baseline vehicle has static proportioning, it should be observed that the ABP vehicle creates a curve similar to the optimal curve presented in Section 5.4

achieves higher peak deceleration than the baseline vehicle.

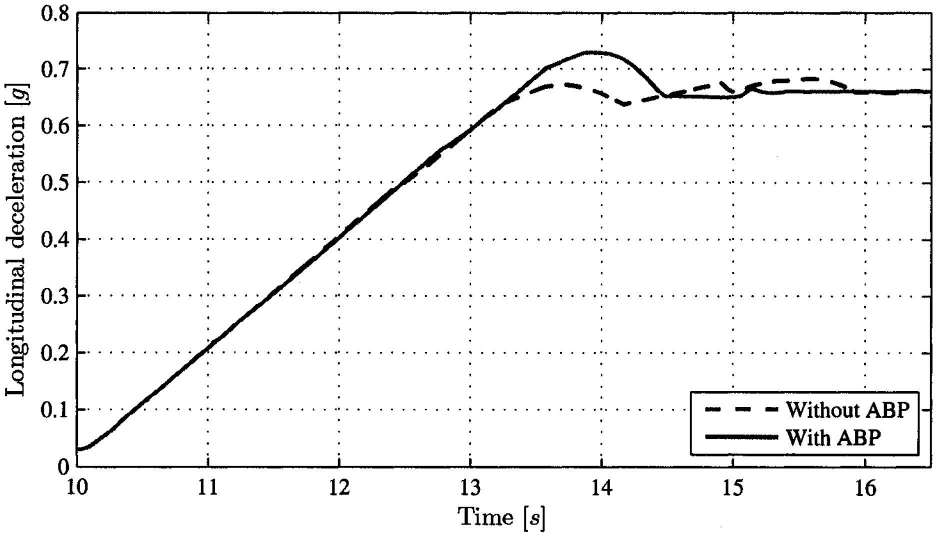

Figure 8.5: *Straight line braking (no ABS): Longitudinal deceleration.* The longitudinal deceleration levels for the baseline and *ABP* vehicles are presented. The *ABP* vehicle achieves higher maximum deceleration by utilizing equal traction at all tires.

8.2.2 Straight-line braking: ABS vehicles

Table 8.2: Straight line braking (with ABS): Simulation results summary

Vehicle model	Stopping time	**Change**	Position
Baseline	10.05 s		on path
ABP	9.91 s	−1.35 %	on path

The second simulation compares the straight line braking behaviour of the baseline and *ABP* vehicles, both equipped with ABS. Table 8.2 provides an overview of the results. The baseline ABS vehicle stops faster than either the baseline or *ABP* vehicle in the previous simulation, without ABS. The *ABP* ABS vehicle, however, again stops faster than the equivalent baseline vehicle. The margin of improvement (1.35%) is larger than for the non-ABS simulation. Both vehicles adhered to the desired path, with no apparent instability.

Figure 8.6 displays the vehicle and wheel forward speeds through the braking event. In this case, the ABS system prevents any of the wheels from slowing to a premature stop. Thus, each wheel slows to a stop at the same time as the overall vehicle. ABS actuation is visible as individual wheel speeds slow down, then spike back up to the vehicle speed (as brake pressure is cycled off and on), and continue to cycle up and down. It should be observed that the onset of ABS occurs earlier for the baseline vehicle, and only for the front tires, while ABS braking begins later for the *ABP* vehicle, and does so for all four tires.

The brake pressure applied at the wheels is presented in Figure 8.7. The activation of ABS braking can be clearly seen as pressure spikes, as the pressure is quickly cycled off and on. The baseline vehicle, with front-favoured brake pressure, required front ABS at $\sim 13.6\,s$, and rear ABS at $\sim 15.2\,s$. In comparison, the ABS initiates on the *ABP* vehicle, for all tires, at $\sim 14.16\,s$.

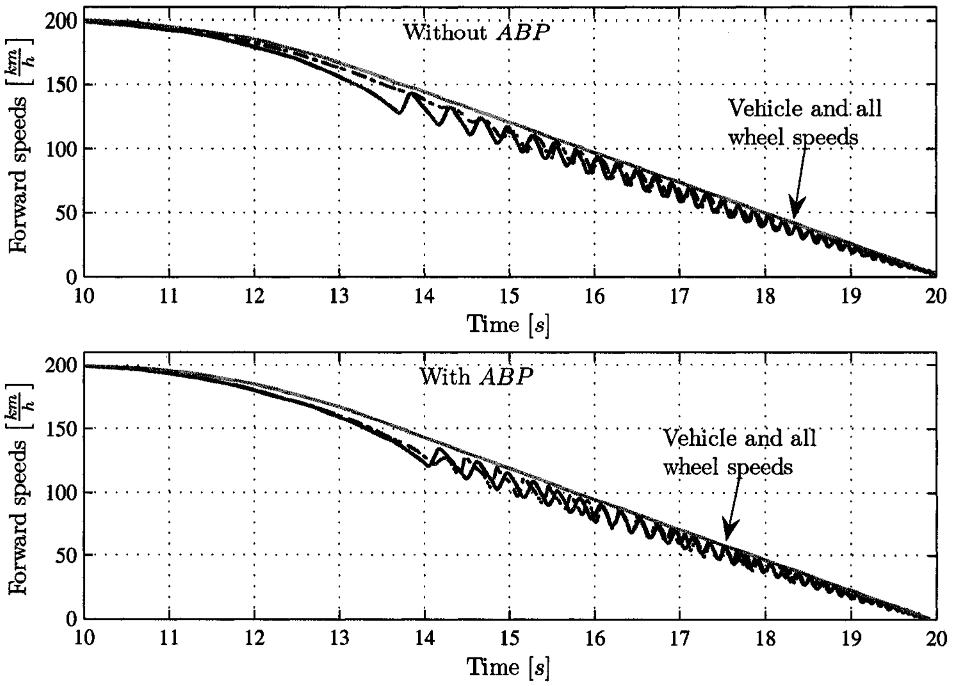

Figure 8.6: *Straight line braking (with ABS): Vehicle and wheel speeds.* The vehicle speed and wheel speeds are shown during the braking event, for the baseline vehicle (upper plot) and *ABP* vehicle (lower plot). For both vehicles, the ABS system prevents any tires from locking up, hence the vehicle and the tires slow to a stop at the same time. The onset of ABS braking occurs earlier on the baseline vehicle.

The longitudinal deceleration levels (Figure 8.8) again show that the *ABP* vehicle achieves a higher wheels-unlocked deceleration than the baseline vehicle. With the addition of ABS, the baseline vehicle is able to match the peak deceleration of the *ABP* vehicle. As the tires successively lock up, the ABS system keeps each one near its peak traction condition, and continues to increase the braking at the others. However, the *ABP* vehicle is able to achieve and *sustain* the peak deceleration with the tires unlocked, while the baseline vehicle only achieves the peak deceleration during spikes of brake pressure application. This results in a faster stopping time for the *ABP* vehicle.

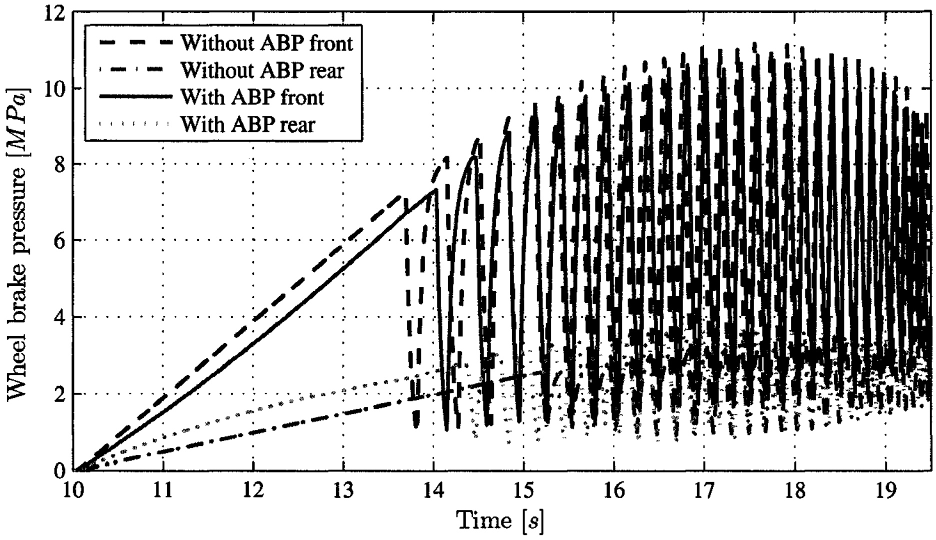

Figure 8.7: *Straight line braking (ABS): Brake pressure.* The brake pressures applied to the wheels are presented. The baseline and *ABP* front tires have similarly large pressures, relative to the rear. The *ABP* front pressure is lower, and thus the onset of ABS is seen to occur later. ABS action is clearly visible as pressure spikes, as pressure is cycled off and on.

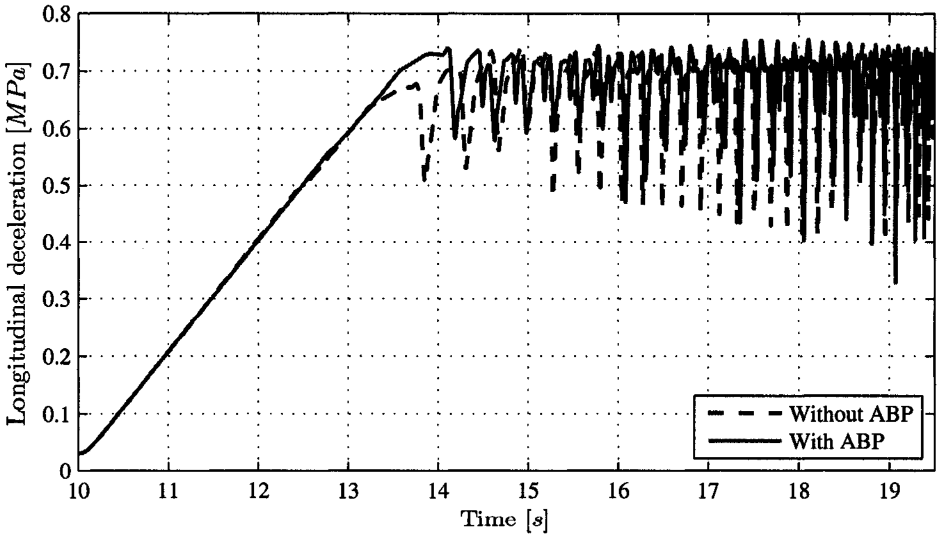

Figure 8.8: *Straight line braking (ABS): Longitudinal deceleration.* The longitudinal deceleration achieved by the ABS-equipped vehicles in straight line braking is presented. The *ABP* vehicle achieves peak wheels-unlocked deceleration earlier, and sustains it longer, than the baseline vehicle.

8.3 Braking while cornering

The second simulation examines the case of combined braking and cornering on a constant radius corner. The active brake proportioning system is expected to improve braking performance appreciably during cornering, as the baseline vehicle braking system is designed only for straight line performance. The braking while cornering simulations replicate a driving situation in which the vehicle is cornering at expressway speeds, and requires emergency braking to avoid colliding with a blockage in the road. It represents a realistic situation, in which a braking system designed for straight line braking may not offer the ideal braking solution.

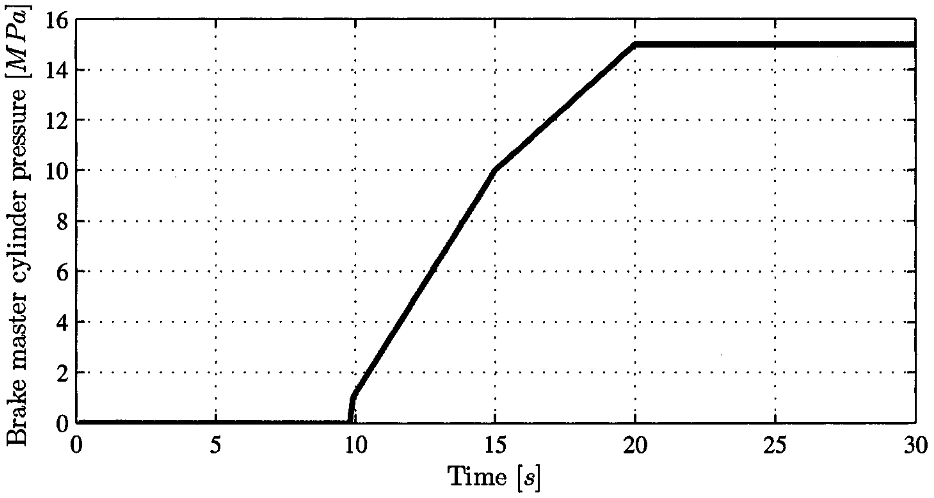

Figure 8.9: *Master cylinder pressure for braking while cornering simulations.* The master cylinder brake pressure is applied during the steady-state cornering maneuver, with no braking until 10 *s*, and a tri-linear braking curve after 10 *s*. The pressure is distributed to each wheel based on static proportioning for the baseline vehicle, or active proportioning for the *ABP* vehicle.

For the braking while cornering simulations, the vehicle corners on a constant 152.4 *m* radius circle, in a left turn. The cornering is held in steady-state for ten seconds. After ten seconds, the brakes are applied according to the master cylinder pressure curve shown in Figure 8.9.

8.3.1 Braking while cornering: Non-ABS vehicles

Table 8.3: *Cornering and braking (no ABS): Simulation results summary*

Vehicle model	Stopping time	**Change**	Position
Baseline	5.805 s		$-1.25\ m$ off path
ABP	5.705 s	$-1.72\,\%$	$-0.5\ m$ off path

The initial braking and cornering test compared the stopping ability of the non-ABS baseline and *ABP* vehicles. An overview of the simulation results is presented in Table 8.3. The stopping time of the *ABP* vehicle was 1.72 % shorter than the stopping time of the baseline vehicle.

The wheel and vehicle speeds are presented in Figure 8.10. As might be expected, the front inside (left) tire locks up first on the baseline vehicle, at $\sim 13.8\ s$. This is a consequence of the weight transferred off the left tires, onto the right tires. For the *ABP* vehicle, all tires lock up nearly simultaneously at $\sim 14.25\ s$.

The brake pressures applied to each wheel are presented in Figure 8.11. For both front and rear brakes, the active proportioning system applies more braking to the outside (right) tires, as expected, due to the cornering lateral acceleration. The right rear tire receives nearly as much brake pressure as the front left tire. Figure 8.12 presents the brake pressure in the front pressure versus rear pressure format (left plot), as well as left side pressure versus right side pressure (right plot). Although each wheel was braked individually, the plots were obtained by summing all front pressures, all left side pressures, etc. As with the straight line braking simulation, the front versus rear braking curve closely approximates the optimal curve described in Section 5.4. The inside pressure versus outside pressure plot

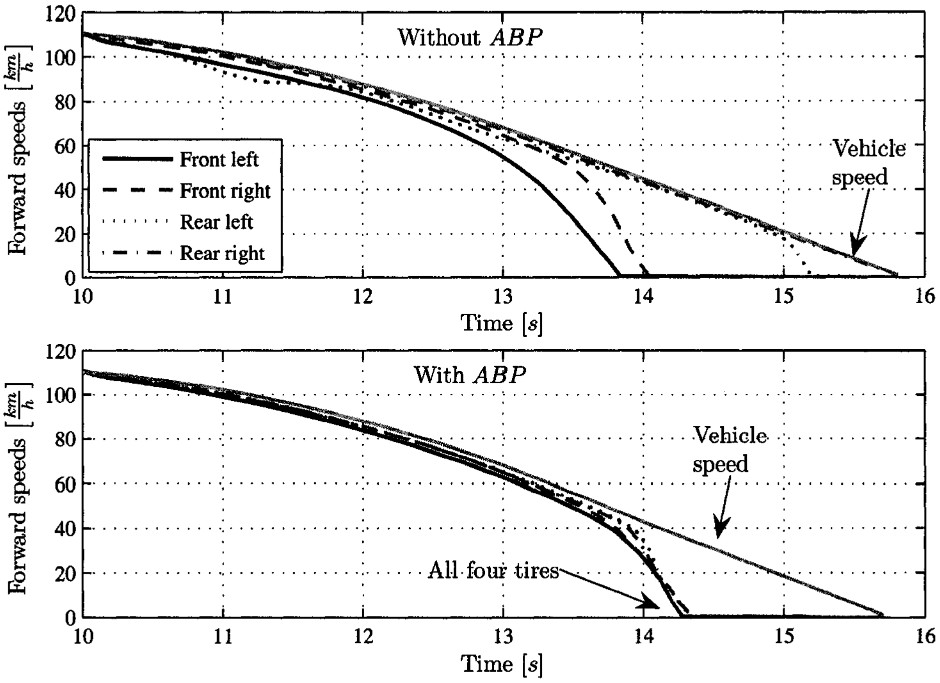

Figure 8.10: *Cornering and braking (no ABS): Vehicle and wheel speeds.* The vehicle speed and wheel speeds are shown during the braking event, for the baseline vehicle (upper plot) and *ABP* vehicle (lower plot). The baseline vehicle locks up the front left and front right tires, successively, beginning at $\sim$ 13.8 s. The *ABP* vehicle locks up all four tires nearly simultaneously, at $\sim$ 14.25 s.

resembles a *lateral optimal curve*, representing the optimal distribution of braking forces between inside and outside tires, subject to lateral acceleration.

Both steering wheel angle and steering wheel torque are presented in Figure 8.13. The results show only minor differences between the baseline and *ABP* vehicles. Upon the onset of braking, there is a small initial *ramp input* required in steering angle for the *ABP* vehicle. This is because the driver must overcome the understeering braking moments, as discussed in Chapter 7. For the remainder of the braking event, the steering torque of the *ABP* vehicle progresses along a smoother trend, as opposed to the slightly fluctuating torque curve for the baseline vehicle.

The longitudinal deceleration (Figure 8.14) again shows higher peak deceleration for the *ABP* vehicle. This is again due to the higher wheels-unlocked deceleration capability,

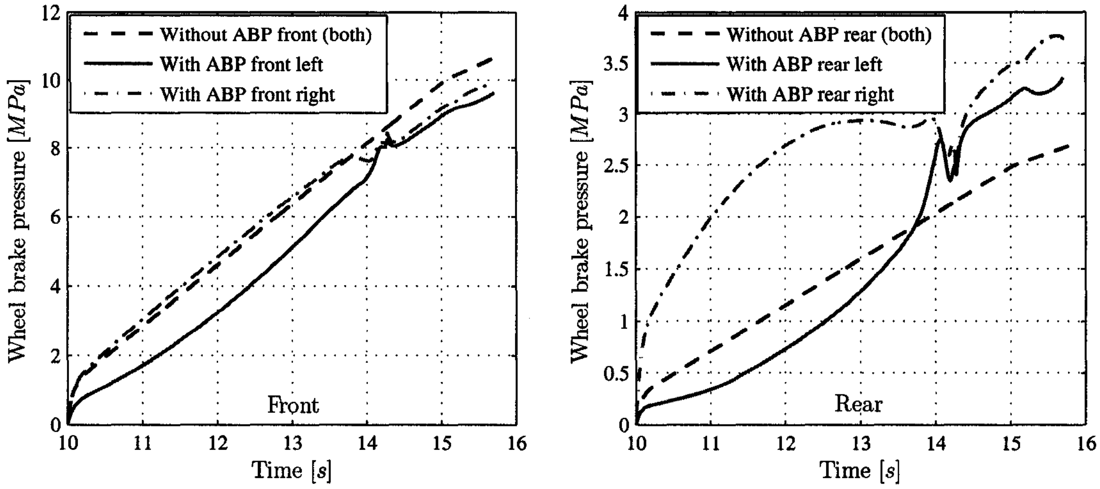

Figure 8.11: *Cornering and braking (no ABS): Brake pressure.* The brake pressure applied to each wheel is presented. The brake pressure on inside and outside tires is identical for the baseline vehicle; the *ABP* vehicle applies more pressure to the outside tires, and less to the inside tires.

due to the *ABP* system making use of the braking traction available at each tire, without causing premature lock-up. The increase in longitudinal deceleration is responsible for the shorter stopping time of the *ABP* vehicle. The lateral acceleration curve is also presented in Figure 8.14. Lateral acceleration is at its largest during steady-state cornering, and decreases as the vehicle slows to a stop. As with steering wheel torque, the *ABP* vehicle is shown to follow a smoother trend in lateral acceleration, compared to the baseline vehicle. The fluctuating nature of the baseline vehicle response may be caused by the slowing (locking up) of some wheels due to overbraking of lightly loaded tires. The uneven wheel speeds may affect the motion of the vehicle.

The lateral deviation from the desired path is presented in Figure 8.15. This represents how far the vehicle swerves off the steady-state cornering path. The final resting place of both vehicles is off the path in the negative direction, though the deviation is much larger for the baseline vehicle.

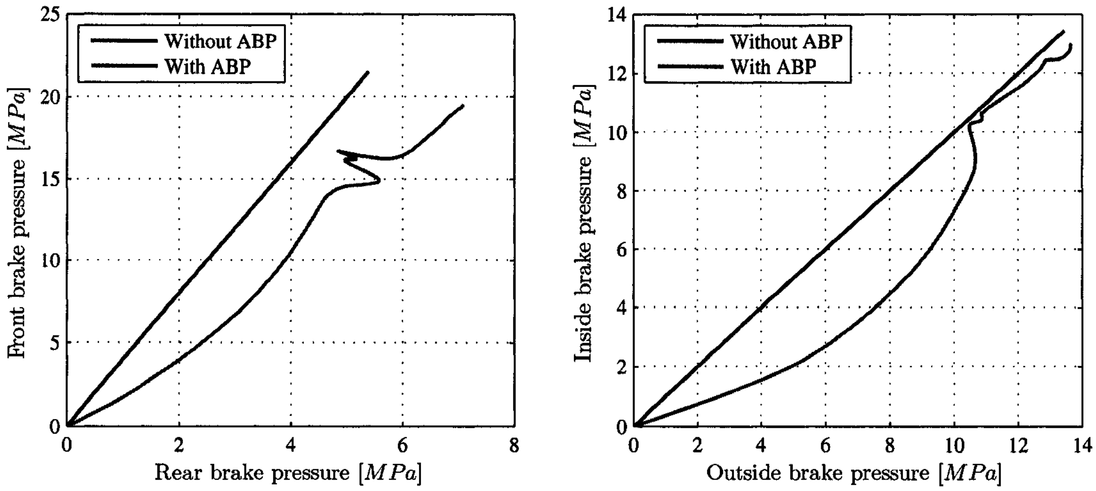

Figure 8.12: *Cornering and braking (no ABS): "Braking curve" - front braking versus rear braking, and inside braking versus outside braking.* Front braking forces versus rear braking forces is presented. The trend is linear for the baseline vehicle, and approximates the *optimal curve* for the *ABP* vehicle. The sum of inside braking forces is plotted versus the sum of outside braking forces, creating a *lateral optimal curve* (a function of lateral acceleration).

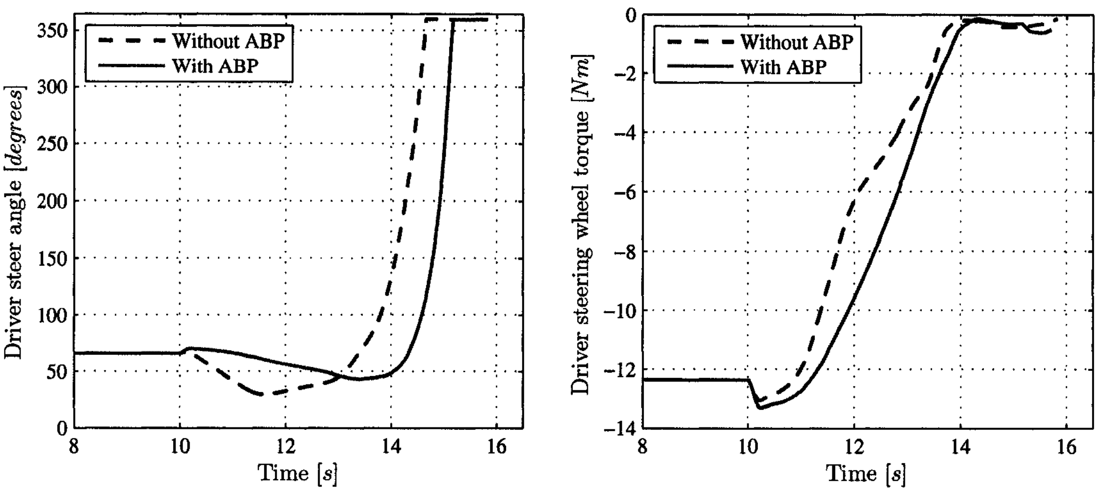

Figure 8.13: *Cornering and braking (no ABS): Steering wheel angle and steering wheel torque.* The steering wheel angle and steering wheel torque required from the driver are presented, for each vehicle. For both curves, the *ABP* vehicle sees larger spike increases at the onset of braking. The baseline vehicle torque appears to fluctuate more than that of the *ABP* vehicle.

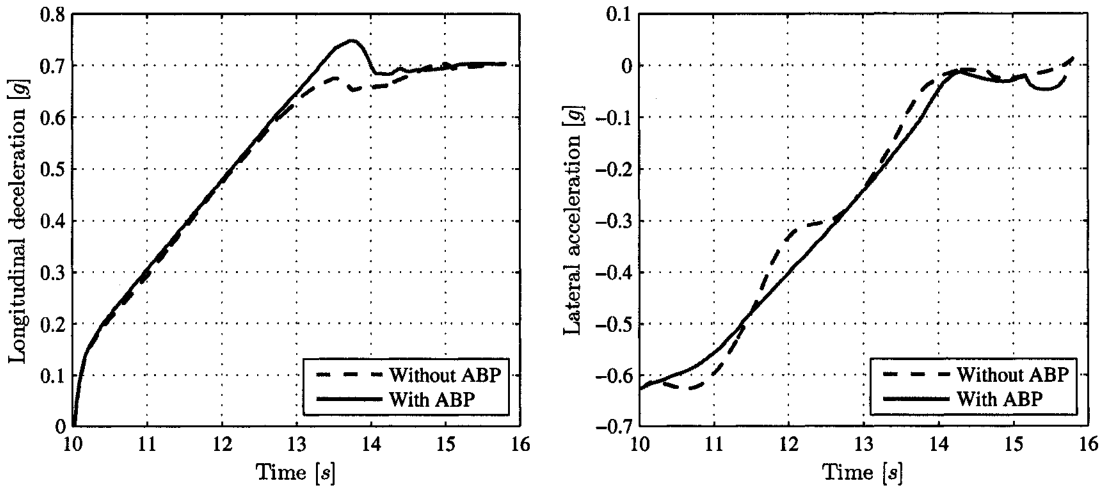

Figure 8.14: *Cornering and braking (no ABS): Longitudinal deceleration and lateral acceleration.* The longitudinal deceleration and lateral acceleration of both vehicles are presented. As in the straight line case, the *ABP* vehicle achieves a larger wheels-unlocked longitudinal deceleration, contributing to shorter stopping times. The lateral acceleration trend is shown to be *smoother* for the *ABP* vehicle.

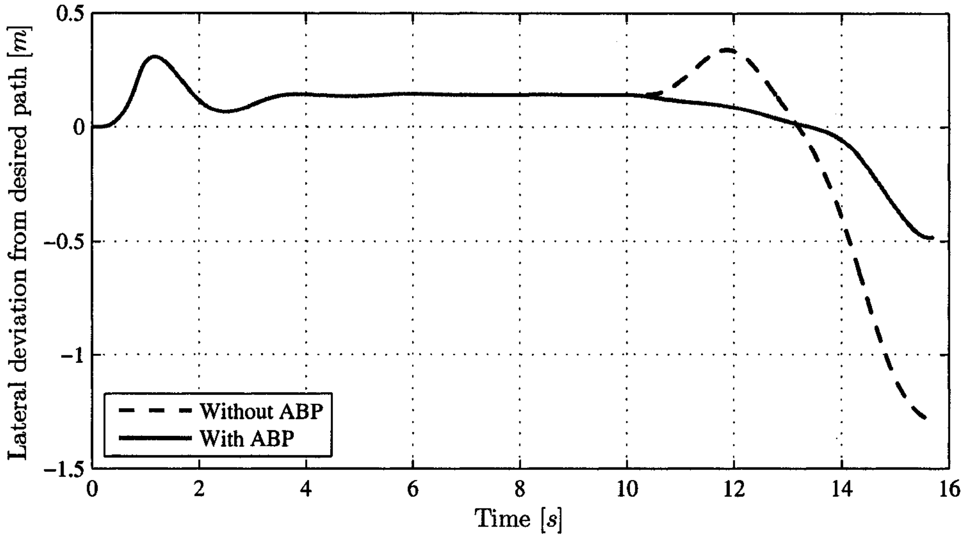

Figure 8.15: *Cornering and braking (no ABS): Lateral deviation from desired path.* The lateral deviation off the desired vehicle path is plotted, for both vehicles. Both vehicles swerve off the path as they stop, though the baseline vehicle does so more than the *ABP* vehicle. The baseline vehicle undergoes a swerve off the path at the onset of braking, which the driver model was unable to correct.

8.3.2 Braking while cornering: ABS vehicles

Table 8.4: *Cornering and braking (with ABS): Simulation results summary*

Vehicle model	Stopping time	**Change**	Position
Baseline	5.87 s		on path
ABP	5.75 s	−2.04 %	on path

The second braking and cornering test compared the stopping ability of the ABS-equipped baseline and *ABP* vehicles. An overview of the simulation results is presented in Table 8.4. The stopping time of the *ABP* vehicle was 2.04 % shorter than that of the baseline vehicle. As with the straight line braking simulations, the margin of improvement in stopping time is larger for the ABS case.

Figure 8.16 presents the wheel speeds and vehicle speeds for both vehicles, through the braking event. Similarly to the straight line braking with ABS simulation, no tires lock up, as ABS braking intervenes to keep them spinning. The onset of ABS braking is extremely delayed for the *ABP* vehicle. The front left tire locks up and requires ABS at $\sim 12.8\ s$ on the baseline vehicle, whereas all tires slip at the same time and require ABS at $\sim 13.7\ s$ on the *ABP* vehicle.

The brake pressure at each wheel is displayed in Figure 8.17. The active proportioning of the brakes drastically changes the lockup behaviour of the tires. The front left brake is observed to enter ABS braking much later for the *ABP* vehicle, as the pressure is redistributed to the outside and rear tires. Both rear tires on the *ABP* vehicle eventually require ABS, while the rear tires on the baseline vehicle are underbraked, and never lock up.

The steering wheel angle and steering wheel torque are presented in Figure 8.18. The

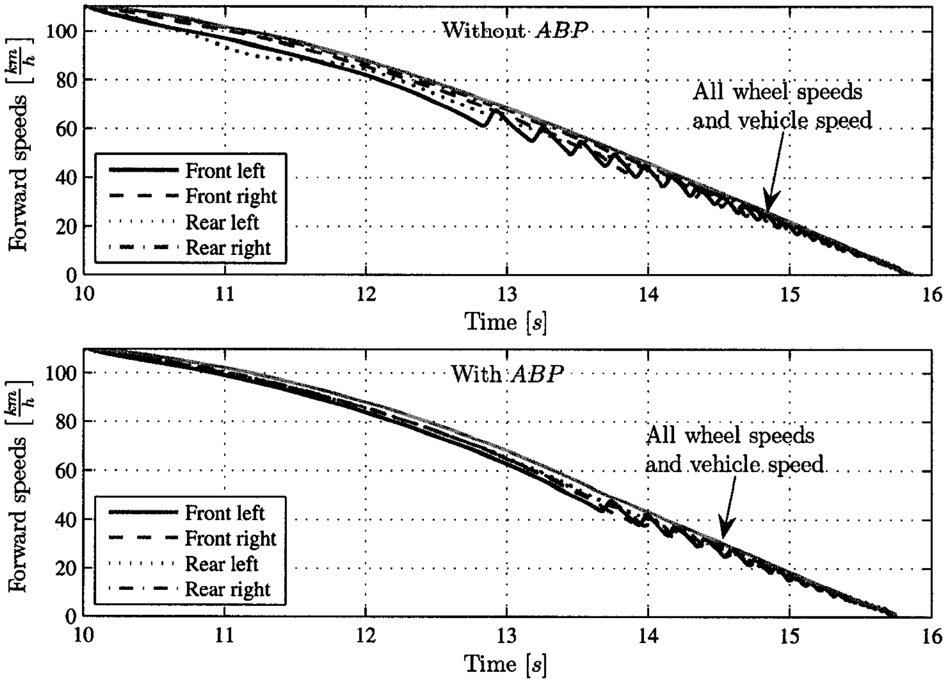

Figure 8.16: *Cornering and braking (with ABS): Vehicle and wheel speeds.* The vehicle speed and wheel speeds are shown during the braking event, for the baseline vehicle (upper plot) and *ABP* vehicle (lower plot). The baseline vehicle requires ABS braking at the front left tire at ~ 12.8 *s*. The *ABP* vehicle requires ABS braking at all four tires nearly simultaneously, at ~ 13.7 *s*.

trends are very similar to the non-ABS case, with the exception that ABS actuation creates vibrations through the steering system. The later onset of ABS braking for the *ABP* vehicle implies that the driver may avoid experiencing this ABS feedback through the steering wheel.

Figure 8.19 displays the longitudinal deceleration and lateral acceleration. As with the ABS case of straight line braking, the *ABP* vehicle achieves peak deceleration before locking any tires, followed by the baseline vehicle later achieving the same level of deceleration. Again, because the *ABP* vehicle sustains peak deceleration before locking any tires, the average deceleration level of the *ABP* vehicle is higher than that of the baseline vehicle. As with the non-ABS case for braking and cornering, the lateral acceleration curve follows a much smoother trend for the *ABP* vehicle.

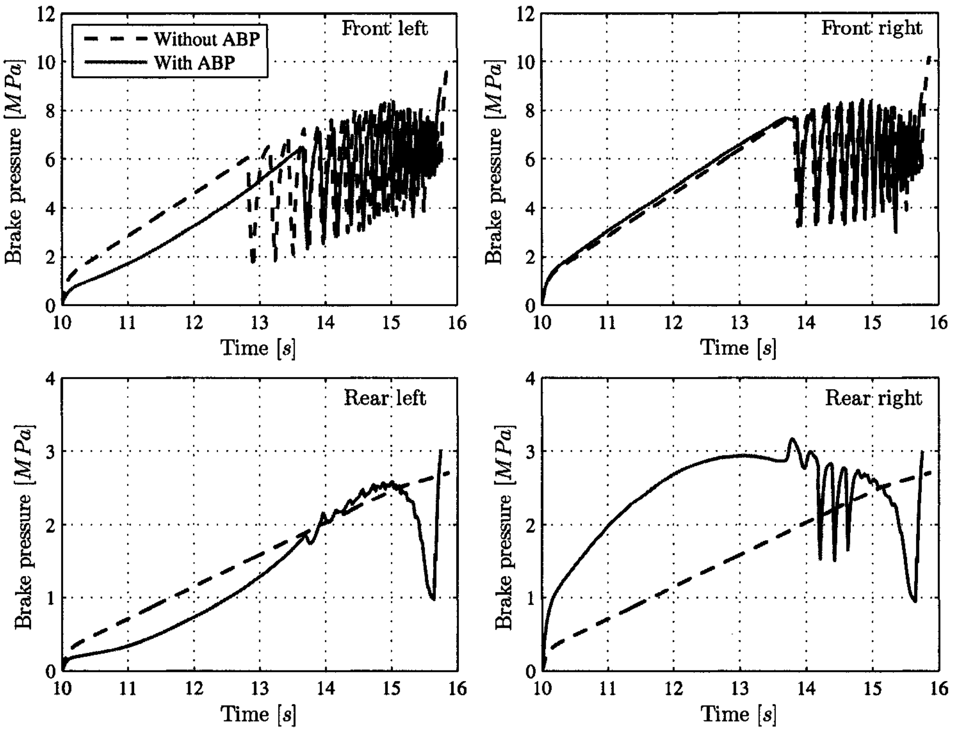

Figure 8.17: *Cornering and braking (with ABS): Brake pressure.* The brake pressure applied to each wheel is presented. The active proportioning system delays the onset of ABS braking, but eventually requires ABS on all four tires. The baseline vehicle requires ABS early on the front left tire, but never requires ABS on the underbraked rear tires.

The primary advantage of ABS systems is retaining the steerability of the vehicle. The lateral deviation plot (Figure 8.20) confirms the improvements due to ABS, as both vehicles come to rest on the desired path, rather than off the path as in the non-ABS case (Figure 8.13). As in the non-ABS case, the baseline vehicle shows a swerve into the turn at the onset of braking, which the driver is unable to prevent.

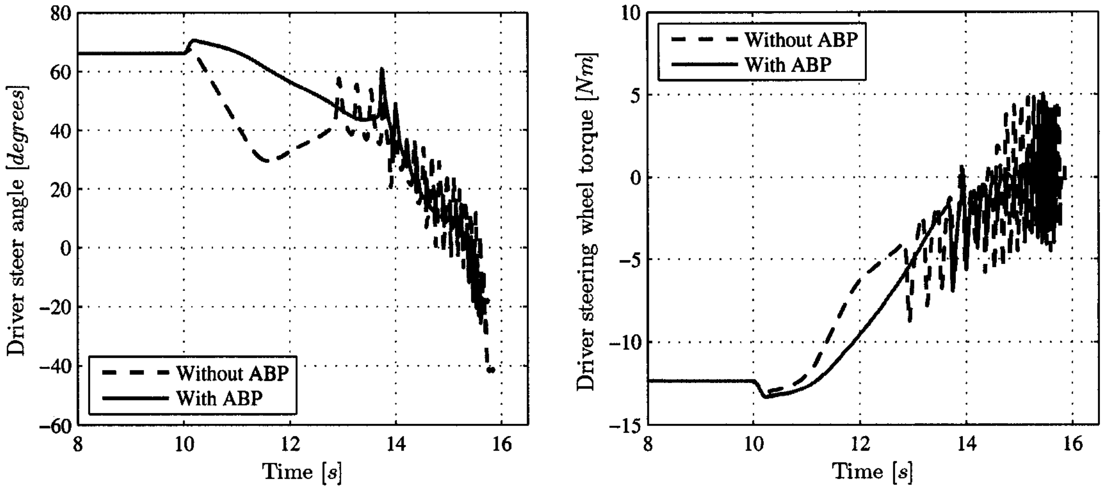

Figure 8.18: *Cornering and braking (with ABS): Steering wheel angle and steering wheel torque.* The steering wheel angle and steering wheel torque required from the driver are presented, for each vehicle. For both curves, the *ABP* vehicle sees larger spike increases at the onset of braking. The baseline vehicle torque appears to fluctuate more than that of the *ABP* vehicle. Both curves show vibrations through the steering system due to the onset of ABS braking.

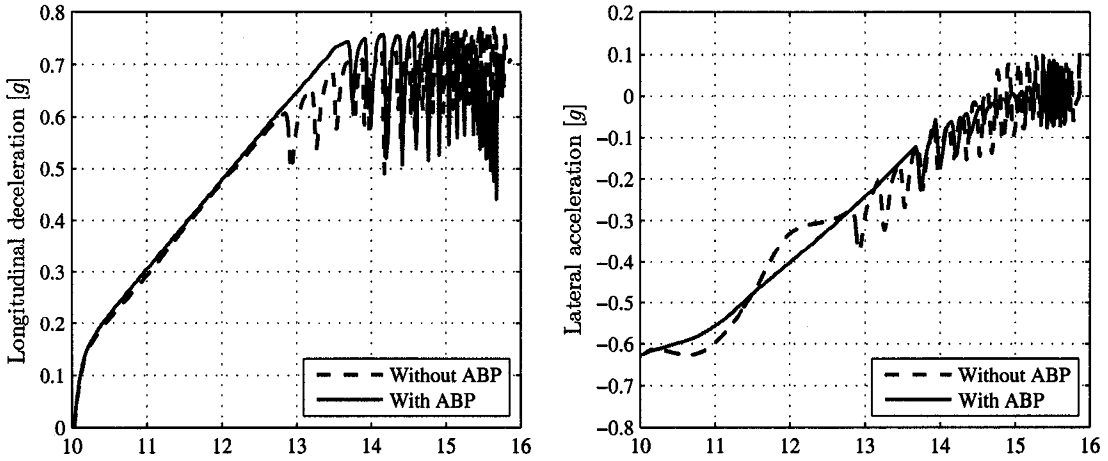

Figure 8.19: *Cornering and braking (with ABS): Longitudinal deceleration and lateral acceleration.* The longitudinal deceleration and lateral acceleration of both vehicles are presented. As in the straight line case, the *ABP* vehicle achieves a larger wheels-unlocked deceleration, contributing to shorter stopping times. The lateral acceleration trend is shown to be *smoother* for the *ABP* vehicle.

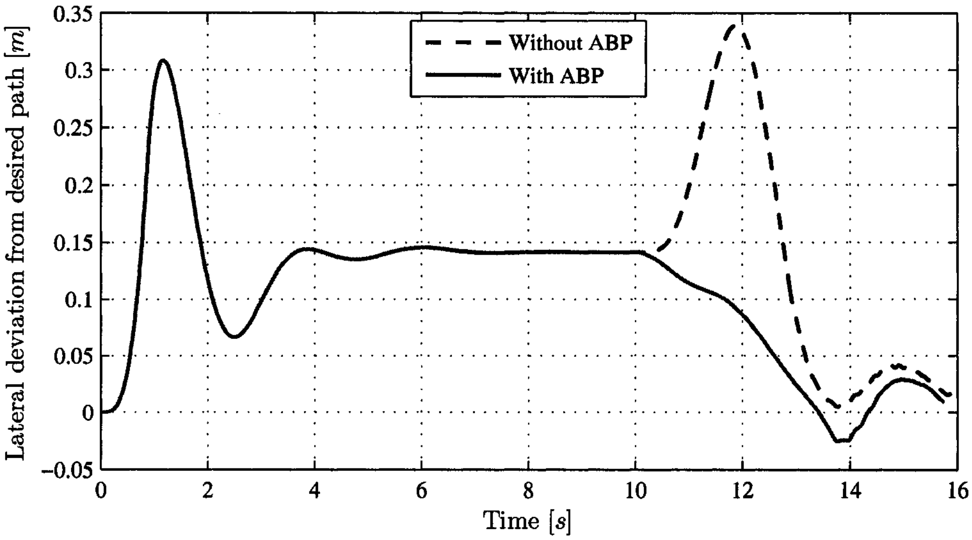

Figure 8.20: *Cornering and braking (with ABS): Lateral deviation from desired path.* The lateral deviation off the design vehicle path is plotted, for both vehicles. Both vehicle swerve off the path as they stop, though the baseline vehicle does so more than the *ABP* vehicle. The baseline vehicle undergoes a swerve off the path at the onset of braking, which the driver model was unable to correct.

8.4 Braking and cornering with obstacle

The third situation to be simulated is a more complicated case of combined braking and cornering, during which the vehicle must also swerve to avoid an oncoming obstacle. It is realistic to expect that for a quickly approaching obstacle, such as a deer, a driver may quickly apply brakes *and* attempt to steer the vehicle.

For the braking while cornering with obstacle simulations, the vehicle corners on a constant 152.4 m radius circle, in a left turn, at $110\frac{km}{h}$. The cornering is held in steady-state for ten seconds. After ten seconds, the brakes are applied according to the master cylinder pressure curve shown in Figure 8.9, and the vehicle attempts to perform a double lane change maneuver. The double lane change consists of a 3.5 m swerve *into* the turn, followed by a return to the original circular path.

Further obstacle avoidance simulations were performed, in which the vehicle was required to swerve *out of* the curve. These simulations were also conducted for both ABS and non-ABS equipped vehicles. The results of these simulations have been omitted for brevity, but are presented in Appendix C, Section C.2.

8.4.1 Braking and cornering with obstacle (inside swerve): Non-ABS vehicles

Table 8.5: *Braking and cornering with obstacle (inside swerve, no ABS): Simulation results summary*

Vehicle model	Stopping time	Change	**Position**
Baseline	6.405 s		off path, out of control
ABP	8.040 s	25.52 %	on path

The first inside obstacle maneuver was simulated for the baseline and *ABP* vehicles without ABS. Table 8.5 gives an overview of the final state of the vehicles. While the *ABP*

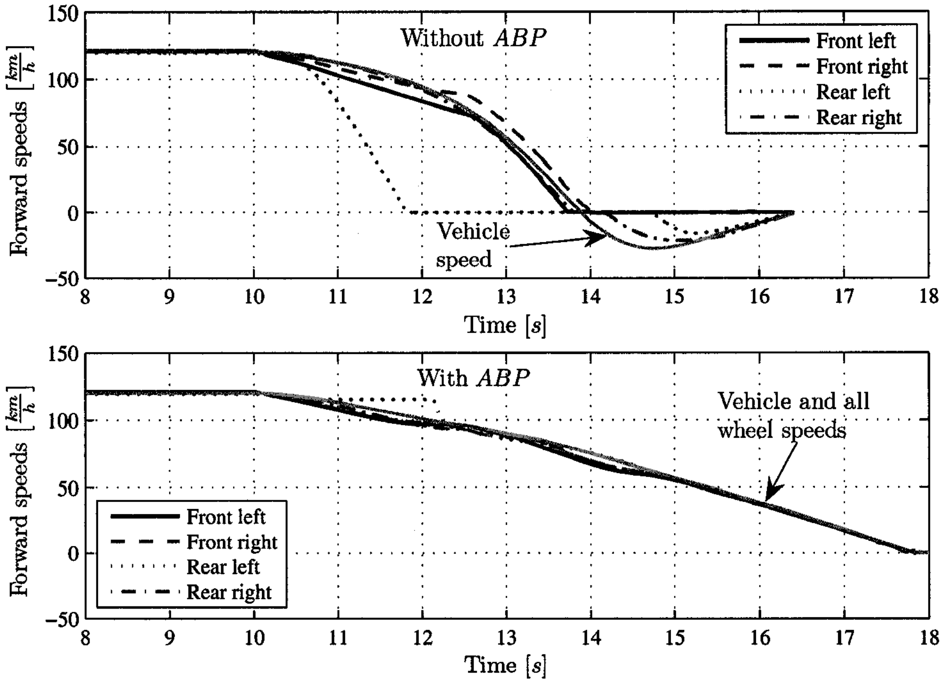

Figure 8.21: *Braking and cornering with obstacle (inside swerve, no ABS): Vehicle and wheel speeds.* The speeds of the vehicles and each wheel during the braking / obstacle event are presented. Even without ABS, no tires lock up for the *ABP* vehicle. The baseline vehicle locks up one tire early in the maneuver. The negative vehicle speed for the baseline vehicle results from the fact that the vehicle has lost control and is rolling backwards.

vehicle adequately followed the desired path, and completed the double lane change, the baseline vehicle ended the simulation off the path and fully out of control. This result is also clearly shown in the vehicle body slip angle plot (Figure 8.22). A vehicle is generally considered to be uncontrollable if the body slip angle grows above 10 degrees. The slip angle of the non-*ABP* vehicle is observed to become excessively large as it spins out of control, while that of the *ABP* vehicle remains small.

The speeds of each wheel and vehicle are shown in Figure 8.21, and the brake pressures applied for each vehicle are displayed in Figure 8.23. The *ABP* vehicle distributes the braking effort such that no tires lock up during the maneuver. The baseline vehicle, however, locks up the inside rear tire early in the maneuver. The brake pressure data shows that the *ABP* vehicle applies approximately zero braking to the inside rear tire, preventing

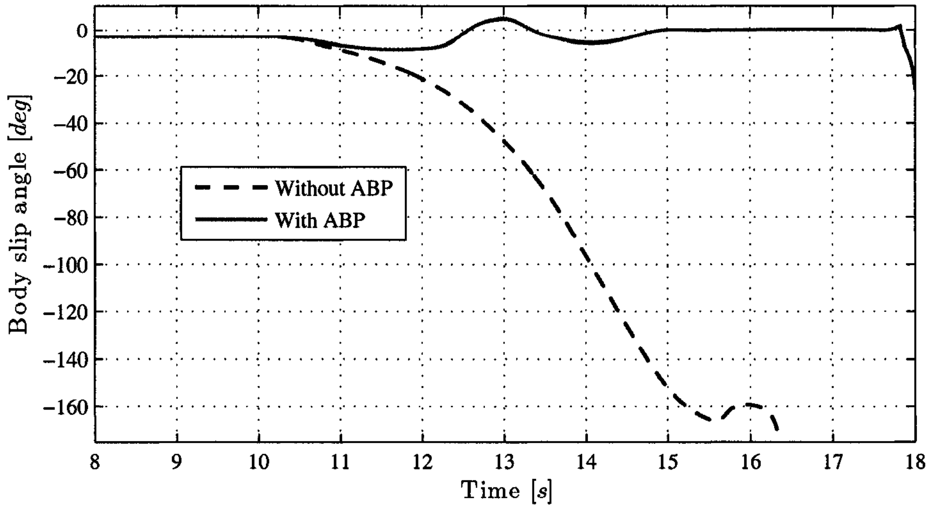

Figure 8.22: *Braking and cornering with obstacle (inside swerve, no ABS): Body slip angle.* The body slip angle of the *ABP* and non-*ABP* vehicles are shown, for the braking with obstacle avoidance maneuver. The slip angle trend for the *ABP* vehicle is typical for a cornering vehicle performing a lane-change maneuver. The slip angle for the non-*ABP* vehicle grows excessively large, signifying that the vehicle has spun around, out of control.

it from locking up. The vehicle speed of the baseline vehicle becomes negative at ~ 14 *s*, indicating that after the heading of the vehicle became reversed, the vehicle began rolling backwards.

The steering wheel angle and torque results, and the acceleration results, are presented in Figure 8.24 and Figure 8.25, respectively. The steering curves and lateral acceleration curve of the baseline and *ABP* vehicle show major differences. Because the baseline vehicle loses traction, and the ability to negotiate the double lane change, there is no apparent pattern in the steering wheel angle, steering wheel torque, and lateral acceleration. The steering and lateral acceleration plots for the *ABP* vehicle show a rise and fall as the vehicle enters and leaves the lane change. The baseline vehicle also cannot successfully generate braking deceleration, while the *ABP* vehicle is able to generate longitudinal deceleration similar to that seen in the previous simulations.

Figure 8.26 displays the trajectory of both vehicles, as well as the ideal target trajectory.

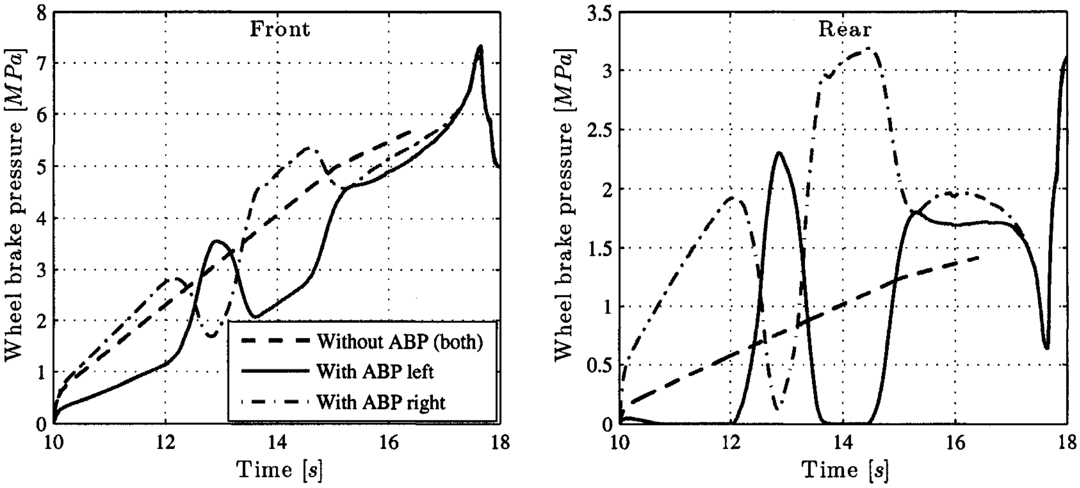

Figure 8.23: *Braking and cornering with obstacle (inside swerve, no ABS): Brake pressure.* The brake pressures applied at each wheel during the braking with obstacle event are presented. The *ABP* vehicle initially applies approximately zero braking to the rear left tire, prevented it from locking up as it does on the baseline vehicle. As the *ABP* vehicle enters and exits the lane change, the braking force between left and right sides is adjusted.

The scale of the plot shows only the period from approximately 13 – 18 *s*. The baseline vehicle experiences a loss of traction, and is unable to remain on the path during the maneuver. The final position of the baseline vehicle is far off the path, and rotated nearly 180° from the correct heading. The *ABP* vehicle, however, has remained on the path, and completed the obstacle avoidance maneuver.

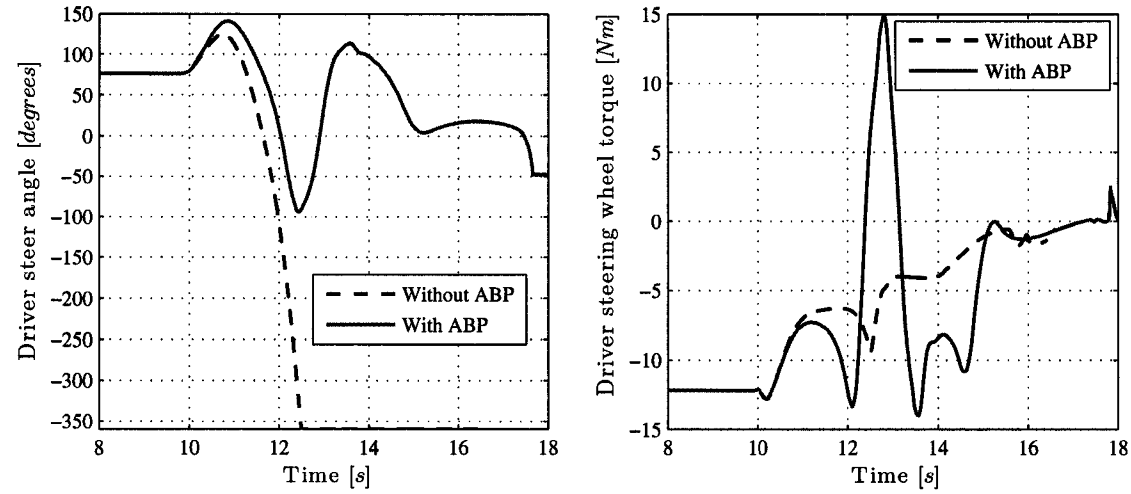

Figure 8.24: *Braking and cornering with obstacle (inside swerve, no ABS): Steering wheel angle and steering wheel torque.* The steering wheel and steering torque results are presented. The steering torque achieved is much larger for the *ABP* vehicle, as the driver successfully performs the double lane change. For the baseline vehicle, the steering angle goes to −360° as the vehicle loses control.

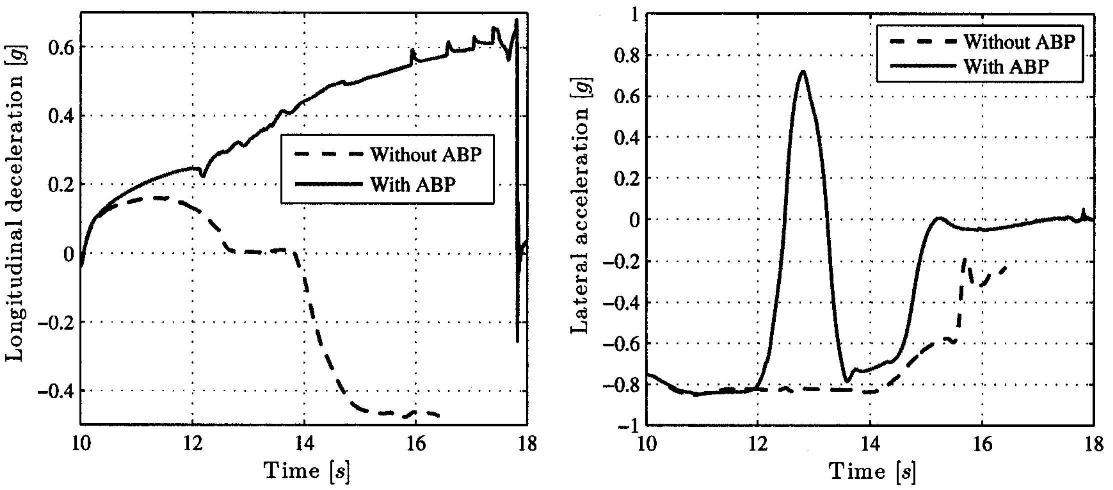

Figure 8.25: *Braking and cornering with obstacle (inside swerve, no ABS): Longitudinal deceleration and lateral acceleration.* The longitudinal deceleration, and lateral acceleration are presented. The *ABP* vehicle achieves a longitudinal deceleration of 0.6 g, while the baseline vehicle loses control and does not decelerate as intended. The baseline vehicle also cannot generate the lateral acceleration required for the double lane change.

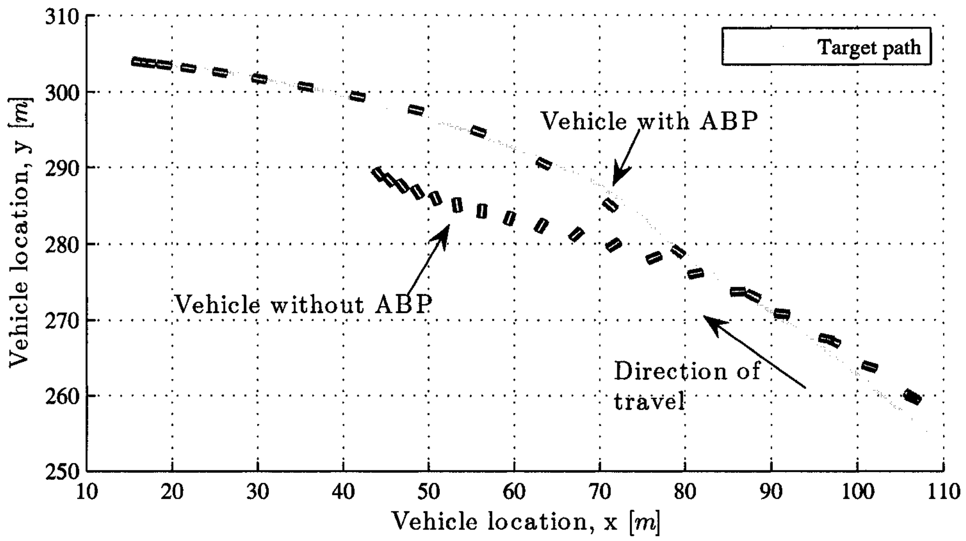

Figure 8.26: *Braking and cornering with obstacle (inside swerve, no ABS): Vehicle trajectory.* The driving paths (location and heading) of the vehicles are shown from an overhead view. The vehicles are represented as small rectangles, in the proportions of an automobile. Observe that the baseline vehicle leaves the desired path and spins backwards, while the *ABP* vehicle follows the path.

8.4.2 Braking and cornering with obstacle (inside swerve): ABS vehicles

Table 8.6: *Braking and cornering with obstacle (inside swerve, with ABS): Simulation results summary*

Vehicle model	Stopping time	Change	**Position**
Baseline	6.60 s		off path, out of control
ABP	7.85 s	18.9 %	on path

The second inside obstacle maneuver was simulated for the baseline and *ABP* vehicles, equipped with ABS. Table 8.6 gives an overview of the final state of the vehicles. The *ABP* vehicle adequately followed the desired path, and completed the double lane change, and despite the addition of ABS, the baseline vehicle ended the simulation off the path and fully out of control.

The vehicle and wheel speeds are shown in Figure 8.27. As with the non-ABS case, no tires slip enough on the *ABP* vehicle to require ABS. The inside rear tire begins to slip early in the simulation, and requires ABS, for the baseline vehicle. The baseline vehicle again loses control and spins, indicated by the negative vehicle velocity between 14 and 16 seconds, and the magnitude of the body slip angle in Figure 8.28. The brake pressure curves (Figure 8.29) show that the baseline vehicle requires ABS braking on three out of four tires, while the *ABP* vehicle does not use ABS. ABS does not prevent the baseline vehicle from losing control, and the *ABP* vehicle does not require ABS, thus the steering and acceleration results closely resemble those for the non-ABS braking case. The plots are presented in Appendix C, Section C.1.1.

Figure 8.30 displays the trajectory of both ABS vehicles, as well as the ideal target trajectory. The scale of the plot shows only the period from approximately 13 – 18 s. The baseline vehicle again experiences a loss of traction, and is unable to remain on the

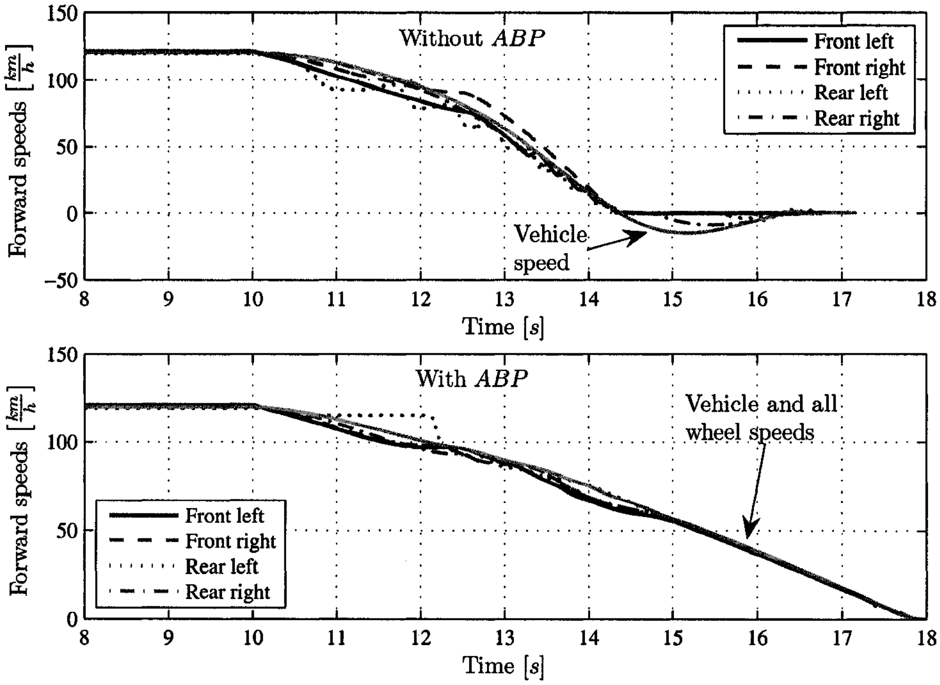

Figure 8.27: *Braking and cornering with obstacle (inside swerve, with ABS): Wheel and vehicle forward speeds.* The speeds of the vehicles and each wheel during the braking and cornering with obstacle event are presented. Again, no tires lock up for the *ABP* vehicle, and thus ABS actuation is not required. The baseline vehicle requires ABS for the inside rear tire early in the maneuver. The baseline vehicle loses control and ends the simulation with a negative velocity.

path through the maneuver. The final position of the baseline vehicle is far off the path, and rotated nearly 100° from the correct heading. The *ABP* vehicle, however, has again remained on the path, and completed the obstacle avoidance maneuver. The addition of ABS did not prevent the loss of control of the baseline vehicle, though the final heading was *closer* to the correct path than for the non-ABS case.

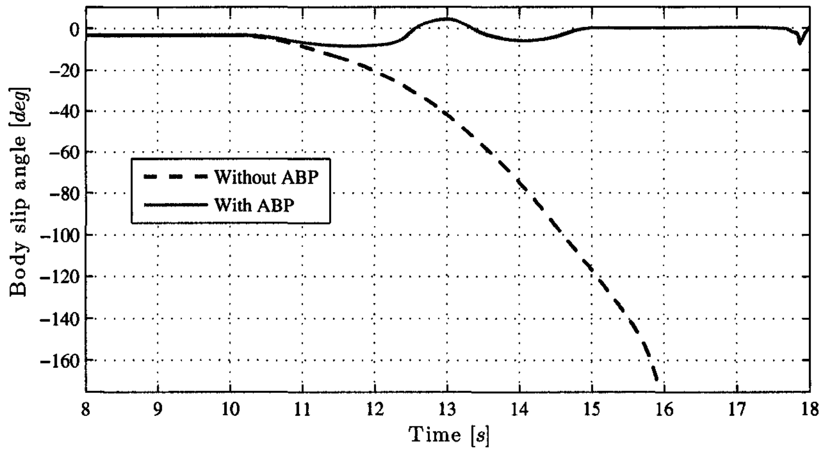

Figure 8.28: *Braking and cornering with obstacle (inside swerve, with ABS): Body slip angle.* The body slip angle of the ABS-equipped *ABP* and non-*ABP* vehicles are shown, for the braking with obstacle avoidance maneuver. The slip angle trend for the *ABP* vehicle is typical for a cornering vehicle performing a lane-change maneuver. The slip angle for the non-*ABP* vehicle grows excessively large, signifying that the vehicle has spun around, out of control.

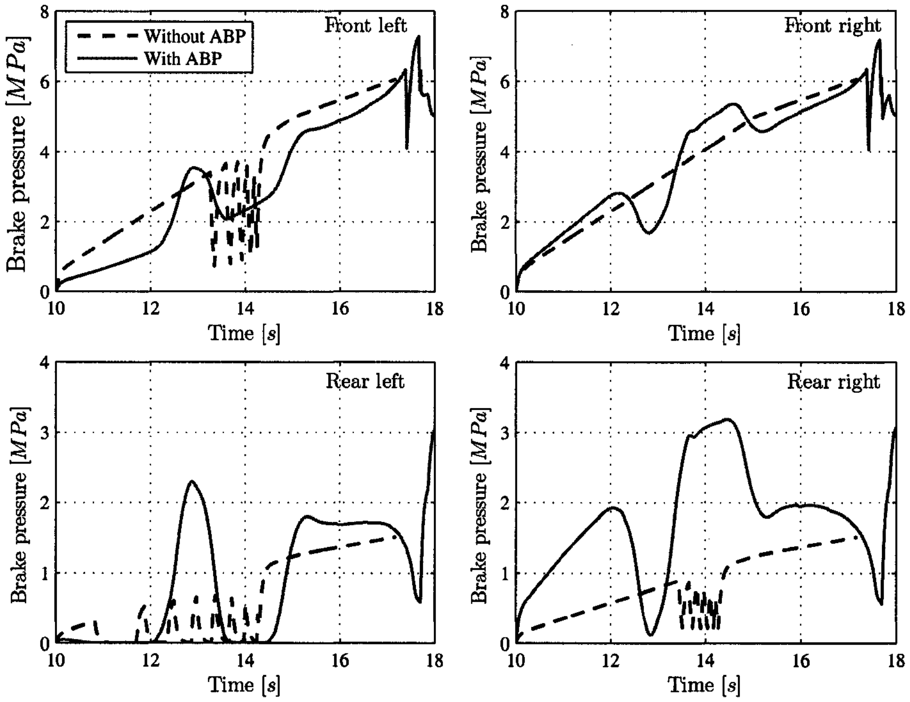

Figure 8.29: *Braking and cornering with obstacle (inside swerve, with ABS): Brake pressure.* The brake pressures applied at each wheel during the braking and cornering with obstacle event are presented. The ABP vehicle initially applies approximately zero braking to the rear left tire, prevented it from locking up as it does on the baseline vehicle. The ABP vehicle prevents the need for any ABS, while three of four tires on the baseline vehicle require ABS.

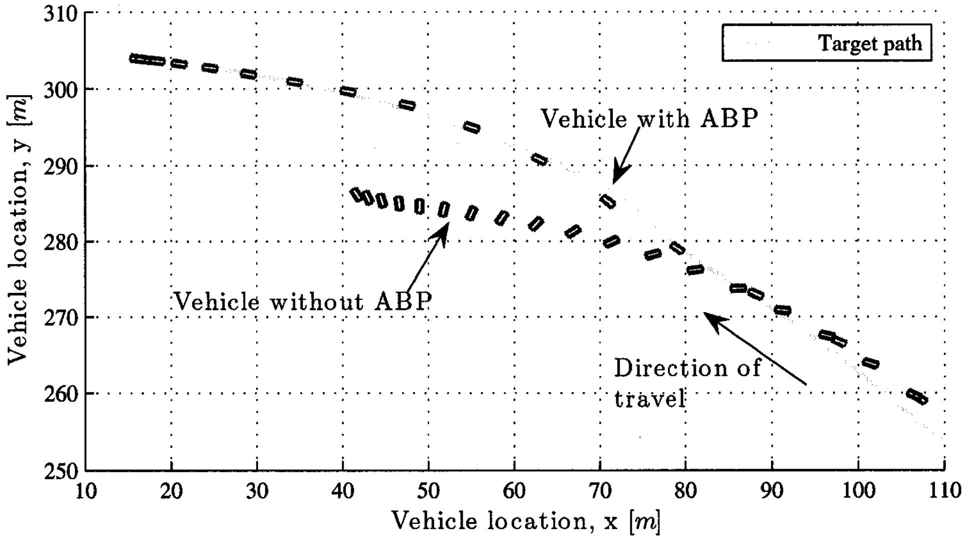

Figure 8.30: *Braking and cornering with obstacle (inside swerve, with ABS): Vehicle trajectory.* The driving paths (location and heading) of the vehicles are shown from an overhead view. The vehicles are represented as small rectangles, in the proportions of an automobile. Observe that, as in the non-ABS case, the baseline vehicle leaves the desired path and spins backwards, while the *ABP* vehicle follows the path.

8.5 Discussion of Results

A series of simulations were performed on a typical passenger sedan, in order to assess the effects of active brake pressure proportioning on a vehicle undergoing emergency stopping maneuvers. The maneuvers investigated were straight line braking, braking while cornering at steady-state, and braking while cornering and simultaneously performing an obstacle avoidance maneuver.

In both straight line and cornering maneuvers, the *ABP* vehicle distributed brake pressure in a manner that caused all tires to lose traction simultaneously. Based on the concepts of ideal brake force distribution ($\mu_{front} = \mu_{rear} = a$), and the optimal braking force curve, it can be concluded that the control method is successful in utilizing equal traction at each of the braked tires. Furthermore, the control system is successful in following a *lateral* optimal curve, and correctly laterally proportioning braking forces based on whether or not the vehicle is cornering.

In each simulated case, the *ABP* vehicle was able to stop faster than the baseline vehicle. This was directly caused by the equal utilization of traction at each tire. The braking forces, and hence the vehicle deceleration, were able to achieve higher levels before any tires began to lock up. The higher sustained deceleration levels translated to shorter stopping times.

When the *ABP* vehicle was equipped with ABS, and compared to a baseline vehicle with ABS, advantages were still apparent. The most obvious, and expected, result was the delayed onset of ABS braking. In each simulation, the baseline vehicle required ABS sooner than the *ABP* vehicle. In the cornering with obstacle simulations, the *ABP* vehicle completely avoided the need for ABS, while the baseline vehicle required ABS on three of four tires.

For the case of ABS braking, the stopping times were again shorter for the *ABP* vehicle. Furthermore, the margin of improvement was larger than for the non-ABS vehicle simulations. In each braking maneuver, before tires lock up, the *ABP* vehicle is able to achieve a higher deceleration. With the addition of ABS, the baseline vehicle was able to reach the same peak deceleration value during ABS braking. However, the benefits of attaining peak deceleration before locking the tires was that the deceleration was sustained for a moment of time, without the pressure pulses associated with ABS. Thus, the delayed onset of ABS braking achieved by the *ABP* vehicle resulted in shorter stopping times.

For the simulations of braking and cornering while simultaneously avoiding an obstacle, the *ABP* vehicle displayed stability benefits. As the brakes were applied, the baseline vehicle locked up a single tire. The *ABP* vehicle chose not to request any braking force at that tire, and hence did not lock it up. Then, when the lane-change was attempted, the baseline vehicle's locked tire was unable to generate satisfactory lateral forces to perform the maneuver. The result was that the baseline vehicle left the path and went out of control. Further simulations were performed with the swerving maneuver out of the turn, rather than into it, with the same result (Appendix C, Section C.2). The results of the simulations suggest that *correctly* utilizing the available traction for braking likewise ensures that the most traction possible will be available for handling. Hence, the brake proportioning control is successful in improving the handling stability of the vehicle.

The effects of brake control strategy on the steerability of the vehicle were also investigated. In all cases, the effects on driver requirements were minimal. The moments created by applying uneven braking forces necessitated additional steering input at some points. However, the steering requirements were no less predictable than for the baseline vehicle. In fact, steering trends during cornering and braking suggested that the *ABP* vehicle would offer smoother steering torque (steering feeling) during deceleration. This may be a consequence of the individually fluctuating wheel speeds of the baseline vehicle, as wheels lose traction at different times. The only conclusion to be drawn from the steering plots is that actively controlling the vehicle brake pressures, even at extreme braking situations, causes no noticeable negative effects on the driver requirements. The ABS simulations also showed ABS vibration feedback through the steering system. Thus, the delayed onset of

ABS braking suggests that, at the very least, the control system may spare the driver from being subjected to the disturbing vibrations.

Chapter 9

Conclusions and Recommendations

The braking system is the most safety critical component of an automobile, and is wholly responsible for stopping the vehicle once it is moving. Traditional brake designs, using mechanical-hydraulic circuits, are necessarily designed as a series of compromises. They provide adequate, but not optimal, braking over a large range of conditions. Modern automotive electronics are maturing to the point where fully electronic or electronically controlled braking systems will soon go into production on passenger vehicles. This has prompted the investigation of the possible benefits of an active-predictive brake control system, which would eliminate the compromises in brake pressure distribution.

The proposed control algorithm was developed in MATLAB Simulink, making use of nominal vehicle properties, and sensor data from two accelerometers. The effects of the control system were simulated using CarSim and Simulink. The controlled (ABP) vehicle was compared in all cases to a baseline vehicle, with a braking system representative of that on a typical passenger car.

It was found that it is possible to accurately predict the normal load at each tire on a vehicle undergoing a general acceleration vector, using only nominal vehicle parameters and accelerometer sensor input. Steady-state errors were found to be less than five percent, while errors during transient combined longitudinal-lateral cases were larger, but acceptable. Accelerometers are readily available, and commonly used, automotive sensors. Thus, it should be expected that the cost of implementation of the proposed control system would not be prohibitive.

The braking simulation results show that the active brake proportioning control consistently reduces the stopping times of vehicles undergoing different types of braking maneuvers. Distributing brake pressure based on predicted levels of tractive ability produced braking forces which approximated the optimal braking curve. This results in equal traction utilization at each tire, and hence maximizes the wheels-unlocked deceleration attainable by the vehicle.

The effects of the proposed controls on the driver experience were also investigated. It was found that although the modifications to brake distribution will cause understeering moments on the vehicle, the effects are on an order of magnitude which is easily counter-acted by a typical driver. Furthermore, the *ABP* vehicle exhibited smoother lateral acceleration trends, accompanied by smoother steering wheel torque requirements. It is expected that the cause of the improvements is the near equal rolling speed at each wheel caused by the control system. Thus, the expected net effect on the driver is a moderately improved feel to the driving experience.

In order to improve the accuracy of the brake force distribution, the load prediction algorithm could be improved. The current system shows the accuracy that can be obtained when limited to simple vehicle parameters and accelerations. In order to increase the accuracy of the predictions, the information input into the system needs only to be improved. For simplicity, the algorithm assumes constant values of *CG* height, weight, front and rear roll centre height, track width, wheelbase, etc. If increased accuracy was desired, all kinematic and compliance effects of the vehicle suspension could be included. Furthermore, measures may be taken to understand whether the vehicle is loaded with additional passengers or cargo. If four-wheel linear potentiometers were used to detect suspension compression at each wheel, the system may use this data rather than relying on accelerations.

In reality, accelerometers are subject to the accelerations imparted by the vehicle, and accelerations due to gravity. Though the accelerometers are aligned perfectly longitudinally and laterally when the vehicle is at rest, during vehicle suspension motion they will rotate relative to the ground. Whenever the accelerometer is rotated, it will measure a portion of the acceleration due to gravity. A roll or pitch angle of 5° would impart a false acceleration reading of $1\,g \cdot \sin(5^\circ) = 0.087\,g$. These effects were ignored in the simulations, but it may be prudent to include them if the controls were to be implemented on a vehicle.

To determine the true viability of the control system using actual physical components, data on the electronic braking hardware is required. In the absence of knowledge regarding the hardware, the system was assumed to be able to apply whatever brake pressure it saw fit at each time step, with no consideration of the rate of change of pressure. The response time of the brake components themselves may very likely limit the abilities of the system to react to changes in vehicle accelerations. Response time should be included, if possible, in any future work.

The implementation of a fully functional ABP system into a prototype vehicle presents a challenge in terms of braking hardware. The hardware must be capable of producing rapidly changing brake pressures individually at each wheel-brake assembly. Producing such rapid and accurately modulated pressure signals would be a challenge for existing hydraulic systems within the cost envelope of a typical mass-market vehicle. A possible solution may be the use of electronically programmable wheel-motors at each wheel. This proposed drivetrain architecture would replace all powertrain hardware with individual traction motors placed within each wheel. The controllability of modern electric motors would enable such a system to create satisfactory braking torque for implementation of the ABP system proposed in this thesis. The enhanced controllability would also facilitate seamless implementation of ABS, traction control, vehicle stability control, all-wheel drive, weather sensitive handling, and other useful features that could potentially enhance safety, economy and driveability. Alternatively, fully motorized electrically actuated brake calipers could be implemented on a vehicle with a more conventional powertrain. Motorized brakes would be capable of accurate torque application control, without requiring a drastic redesign of vehicle architecture. This concept may be well suited for implementation on a state-of-the-art hybrid electric vehicle (HEV), taking advantage of high levels of on-board electrical power.

The simulation results comparing the behaviour of the active brake proportioning vehicle to a conventional vehicle are very promising. In addition to improved performance in terms of braking ability, the *ABP* vehicle displayed significantly increased vehicle stability during extreme braking and handling maneuvers. It is expected that the implementation of this system would increase the safety of an automobile, even when compared to current braking safety systems such as ABS. Further investigation into the implementation of this system would be worthwhile.

References

[1] M. Blundell and D. Harty, *The Multibody Systems Approach to Vehicle Dynamics*, Butterworth Heinemann, Oxford, 2004.

[2] G. Buschmann, H. T. Ebner, and W. Kuhn, *Electronic brake force distribution control - a sophisticated addition to ABS*, SAE Paper, 920646 (1992).

[3] S. B. Choi, T. H. Lee, Y. S. Lee, and M. S. Han, *Control performance of an electrorheological valve based vehicle anti-lock brake system, considering the braking force distribution*, Smart Materials and Structures, 14 (2005), pp. 1483–1492.

[4] M. Denny, *The Dynamics of Antilock Brake Systems*, European Journal of Physics, 26 (2005), pp. 1007–1016.

[5] C. M. Farmer, *New evidence concerning fatal crashes of passenger vehicles before and after adding antilock braking systems*, Accident Analysis and Prevention, 33 (2001), p. 361369.

[6] C. M. Farmer, A. K. Lund, R. E. Trempel, and E. R. Braver, *Fatal crashes of passenger vehicles before and after adding antilock braking systems*, Accident Analysis and Prevention, 29 (1997), pp. 745–757.

[7] G. Genta, *Motor Vehicle Dynamics*, World Scientific, Singapore, 1997.

[8] T. D. Gillespie, *Fundamentals of Vehicle Dynamics*, Society of Automotive Engineers, Inc., Warrendale, 1992.

[9] G. Gim and P. E. Nikravesh, *A three dimensional tire model for steady-state simulations of vehicles*, SAE Paper, 931913 (1993).

[10] P. Haney, *Racing & High Performance Tire: Using Tires to Tune for Grip and Balance*, Society of Automotive Engineers, Inc., Warrendale, 2003.

[11] H. HEISLER, *Vehicle and Engine Technology*, Society of Automotive Engineers, Inc., Warrendale, 1999.

[12] R. C. HIBBELER, *Engineering Mechanics. Statics & Dynamics*, Prentice-Hall, Inc., Upper Saddle River, 1998.

[13] W. D. JONNER, H. WINNER, L. DREILICH, AND E. SCHUNCK, *Electrohydraulic brake system - the first approach to brake-by-wire technology*, SAE Paper, 960991 (1996).

[14] K. KOIBUCHI, M. YAMAMOTO, Y. FUKADA, AND S. INAGAKI, *Vehicle stability control in limit cornering by active brake*, SAE Paper, 960787 (1996).

[15] J. D. LAMBERT, *Numerical Methods for Ordinary Differential Systems (The Initial Value Problem)*, John Wiley & Sons, Inc., Chichester, 1991.

[16] H. LEFFLER, *The brake system of the new 7 Series BMW with electronic brake and wheel slip control*, SAE Paper, 950792 (1995).

[17] R. LIMPERT, *Brake Design and Safety 2nd Edition*, Society of Automotive Engineers, Inc., Warrendale, 1999.

[18] C. S. LIU, V. MONKABA, H. TAN, C. MCKENZIE, H. LEE, AND S. SUO, *Driveline torque-bias-management modeling for vehicle stability control*, SAE Paper, 2002-01-1584 (2002).

[19] C. MARON, T. DIECKMANN, S. HAUCK, AND H. PRINZLER, *Electromechanical brake system: Actuator control development system*, SAE Paper, 970814 (1997).

[20] MECHANICAL DYNAMICS, INCORPORATED, *Using ADAMS/Tire*. 2002.

[21] MECHANICAL SIMULATION CORPORATION, *CarSim Multibody Model Descriptions*. 2006.

[22] ——, *CarSim Reference Manual Version 6.05*. 2006.

[23] W. F. MILLIKEN AND D. L. MILLIKEN, *Race Car Vehicle Dynamics*, Society of Automotive Engineers, Inc., Warrendale, 1995.

[24] H. B. PACEJKA, E. BAKKER, AND L. LIDNER, *A New Tire Model with an Application in Vehicle Dynamics Studies*, SAE Paper, 890087 (1989).

[25] J. Reimpell, H. Stoll, and J. W. Betzler, *The Automotive Chassis*, Society of Automotive Engineers, Inc., Warrendale, 2001.

[26] Robert Bosch GMBH, *Automotive electrics and electronics*, Society of Automotive Engineers, Inc., Warrendale, 1999.

[27] R. Roberts, B. Gombert, H. Hartmann, D. Lange, and M. Schautt, *Testing the mechatronic wedge brake*, SAE Paper, 2004-01-2766 (2004).

[28] R. Roberts, M. Schautt, H. Hartmann, and B. Gombert, *Modelling and validation of the mechatronic wedge brake*, SAE Paper, 2003-01-3331 (2003).

[29] D. E. Schenk, R. L. Wells, and J. E. Miller, *Intelligent braking for current and future vehicles*, SAE Paper, 950762 (1995).

[30] P. E. Wellstead and N. B. O. L. Pettit, *Analysis and Redesign of an Antilock Brake System Controller*, IEE Proceedings - Control Theory and Applications, 144 (1997), pp. 413–426.

[31] J. Y. Wong, *Theory of Ground Vehicles*, John Wiley & Sons, Inc., Chichester, 2001.

[32] P. Wright, *Formula 1 Technology*, Society of Automotive Engineers, Inc., Warrendale, 2001.

Appendix A

CarSim large sedan vehicle model

The vehicle model options and parameters in CarSim allow nearly any type of vehicle to be modeled. In order to investigate what would be considered a *typical* vehicle, a modified version of the CarSim *large sedan* vehicle model was designed (Figure A.1). The major nominal vehicle parameters (those used by Simulink for the control algorithm) can be found in Table B.1.

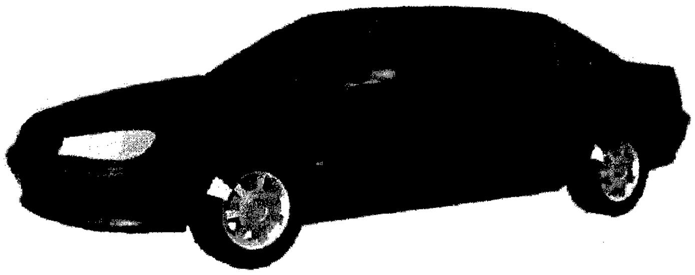

Figure A.1: Graphical representation of CarSim large sedan vehicle model

Many small changes were made to the vehicle to improve accuracy. The coil spring curves used in the vehicle model were replaced with nonlinear sample data provided by Reimpell et al. [25]. Rear steer effects were turned off. The tire data provided with CarSim representing a 205/60R14 tire was used, with only slight modifications for improved accuracy. Aerodynamic effects were disabled, as it was desirable to not have any external effects confounded with the effects of interest.

Table A.1: *CarSim large sedan model parameters.*

Property	Value	Units
Weight (W)	16740	N
Static rear axle load ($F_{Z,Rear,static}$)	6338.6	N
CG Height (h)	0.542	m
Wheelbase (L)	2.69	m
Track width (T)	1.54	m
Front suspension stiffness (one side) (k_f)	15266.7	$\frac{N}{m}$
Rear suspension stiffness (one side) (k_r)	20000	$\frac{N}{m}$
Tire vertical stiffness (k_{ft},k_{rt})	220,000	$\frac{N}{m}$
Approximate brake proportioning (Φ)	0.23	[–]
Front roll stiffness ($K_{roll,front}$)	344	$\frac{Nm}{deg}$
Rear roll stiffness ($K_{roll,rear}$)	384	$\frac{Nm}{deg}$
Front roll centre height ($h_{rc,front}$)	4.425	mm
Rear roll centre height ($h_{rc,rear}$)	1.8	mm
Front rotating mass	100	kg
Front rotating inertia (I_f)	1.8	kgm^2
Rear rotating mass	80	kg
Rear rotating inertia (I_f)	1.8	kgm^2
Tire rolling radius (r)	0.301	m

Appendix B

Predictive controls: alternate vehicle

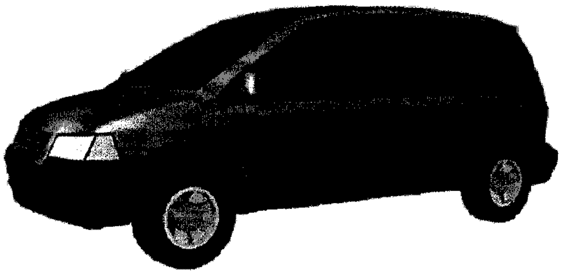

Figure B.1: Graphical representation of CarSim crossover vehicle model

The control algorithm developed in Chapter 6 predicts the normal load on each tire, subject to a general acceleration vector. The prediction is performed using only nominal vehicle parameters and acceleration sensors. The correlation results between the *true* tire-load values calculated by the CarSim vehicle model, and the predicted values, were displayed for the large sedan vehicle model in Section 6.2.4. The prediction capability of the algorithm was also tested on an alternative vehicle model with a different set of nominal vehicle parameters.

The results (Figure B.2) showed that the tire normal loads in the CarSim vehicle model were predicted with good correlation by the control algorithm. The error in lateral load transfer during steady-state cornering was less than $\sim 5\%$ at both the front and rear axles.

Table B.1: *CarSim crossover vehicle model parameters.*

Property	Value	Units
Weight (W)	20454	N
Static rear axle load ($F_{Z,Rear,static}$)	9360	N
CG Height (h)	0.645	m
Wheelbase (L)	2.954	m
Track width (T)	1.68	m
Front suspension stiffness (one side) (k_f)	40,000	$\frac{N}{m}$
Rear suspension stiffness (one side) (k_r)	30,000	$\frac{N}{m}$
Tire vertical stiffness (k_{ft},k_{rt})	300,000	$\frac{N}{m}$
Approximate brake proportioning (Φ)	0.23	[–]
Front roll stiffness ($K_{roll,front}$)	251	$\frac{Nm}{deg}$
Rear roll stiffness ($K_{roll,rear}$)	344	$\frac{Nm}{deg}$
Front roll centre height ($h_{rc,front}$)	87.5	mm
Rear roll centre height ($h_{rc,rear}$)	68	mm
Front rotating mass	96	kg
Front rotating inertia (I_f)	1.8	kgm^2
Rear rotating mass	96	kg
Rear rotating inertia (I_f)	1.8	kgm^2
Tire rolling radius (r)	0.353	m

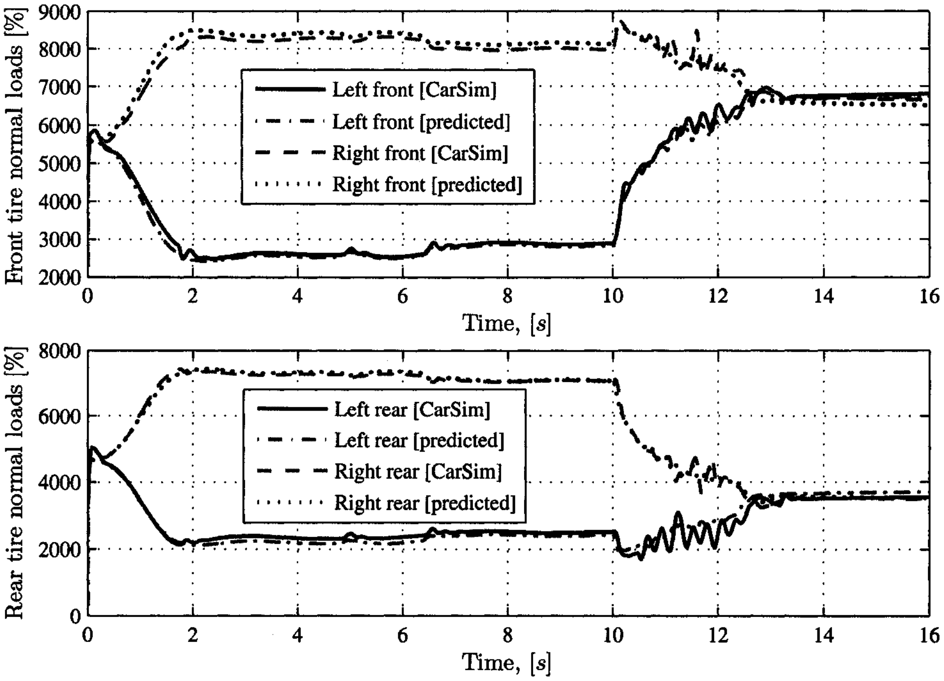

Figure B.2: *Tire loads during cornering maneuver (crossover vehicle model).* During a cornering maneuver simulation using a CarSim crossover vehicle model, the actual and predicted tire normal loads were observed. The predicted loads from Simulink show close agreement with those from CarSim. The error in lateral load transfer was ~ 4% during steady-state cornering.

Appendix C

Additional simulation result plots

Additional simulation results plots are presented here. The results are additional plots for the *braking and cornering with obstacle (inside swerve, with ABS)* simulations, as well as both *braking and cornering with obstacle (outside swerve)* simulations. The results are in agreement with those shown in Chapter 8.

C.1 Braking and cornering with obstacle (inside swerve)

C.1.1 Braking and cornering with obstacle (inside swerve): ABS vehicles

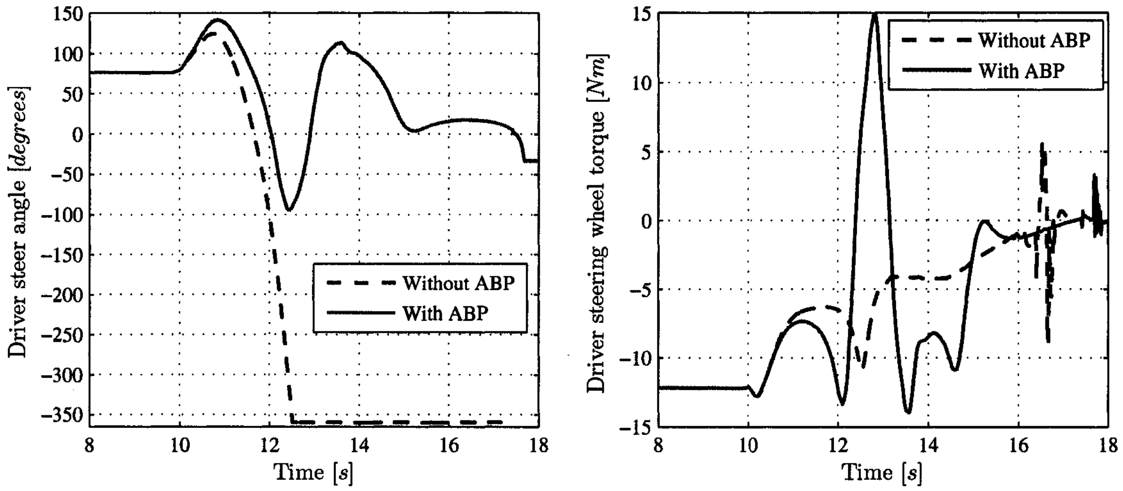

Figure C.1: *Braking and cornering with obstacle (inside swerve, with ABS): Steering wheel angle and steering wheel torque.* The steering wheel and steering torque results are presented. The results are very similar to the non-ABS case. The *ABP* vehicle shows the trends expected for a double lane change, while the baseline vehicle loses control.

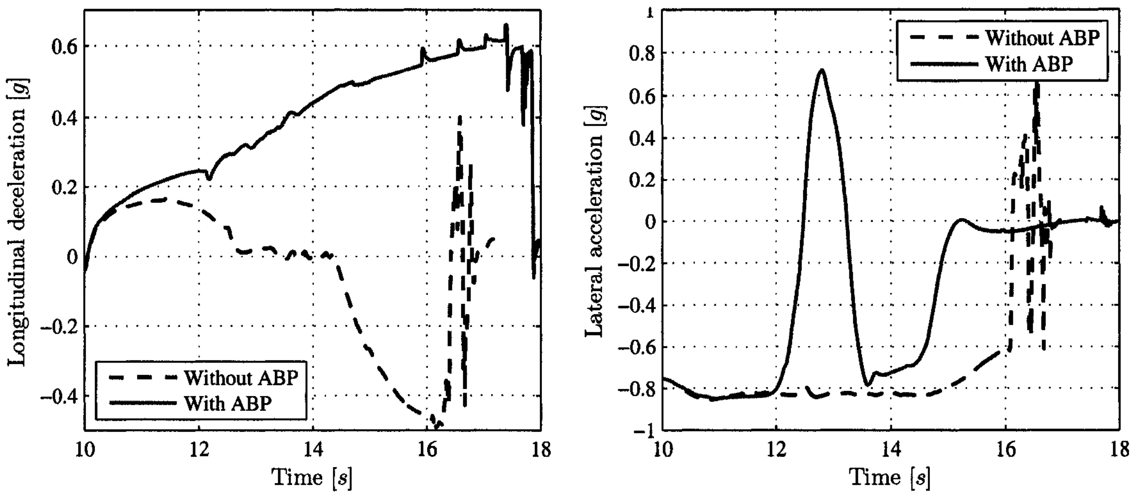

Figure C.2: *Braking and cornering with obstacle (inside swerve, with ABS): Longitudinal deceleration and lateral acceleration.* The longitudinal deceleration, and lateral acceleration are presented. Similar to the non-ABS case, the *ABP* vehicle generates the expected longitudinal and lateral accelerations, while the baseline vehicle loses traction and fails to generate accelerations as expected.

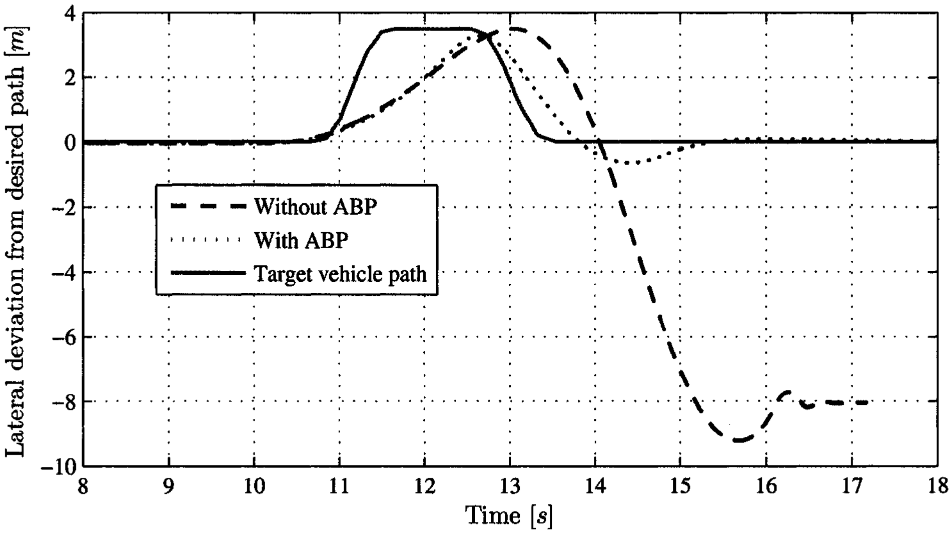

Figure C.3: *Braking and cornering with obstacle (inside swerve, with ABS): Lateral deviation from desired path.* The desired path of the vehicles, relative to the curved path, is shown by the solid line. The *ABP* vehicle completes the double lane change and returns to the desired path, while the baseline vehicle loses control.

C.2 Braking and cornering with obstacle (outside swerve)

Braking and cornering with obstacle (outside swerve): Non-ABS vehicles

Table C.1: *Braking and cornering with obstacle (outside swerve, no ABS): Simulation results summary*

Vehicle model	Stopping time	Change	**Position**
Baseline	5.95 s		off path, spun out
Controlled	7.06 s	18.7 %	on path

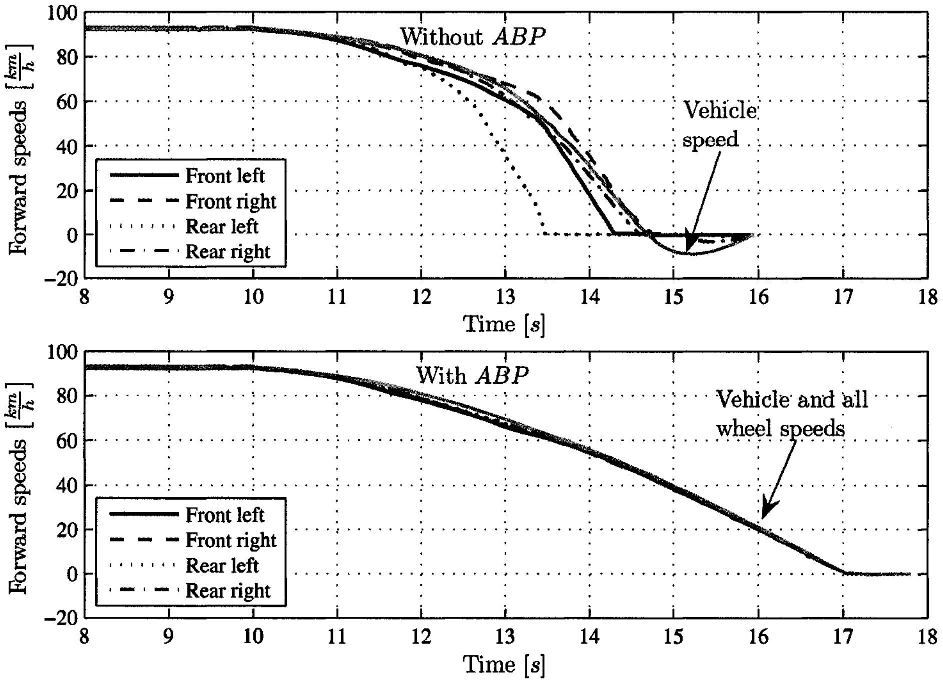

Figure C.4: *Braking and cornering with obstacle (outside swerve, no ABS): Vehicle and wheel speeds.* The speeds of the vehicles and each wheel during the braking / obstacle event are presented. Even without ABS, no tires lock up for the *ABP* vehicle. The baseline vehicle locks up one tire early in the maneuver. The negative vehicle speed for the baseline vehicle results from the fact that the vehicle has lost control and is rolling backwards.

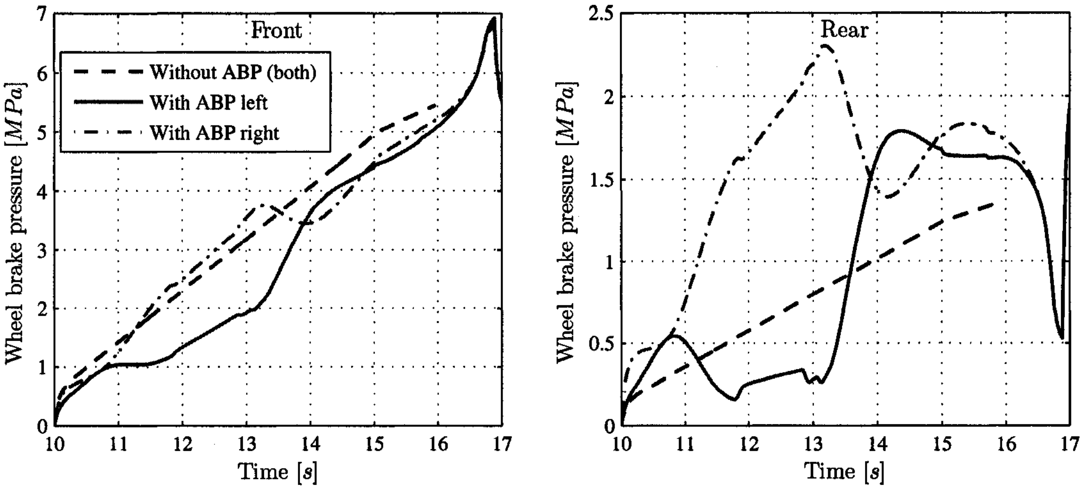

Figure C.5: *Braking and cornering with obstacle (outside swerve, no ABS): Brake pressure.* The brake pressures applied at each wheel during the braking with obstacle event are presented. As the *ABP* vehicle enters and exits the lane change (11 – 14s), the braking force between left and right sides is adjusted.

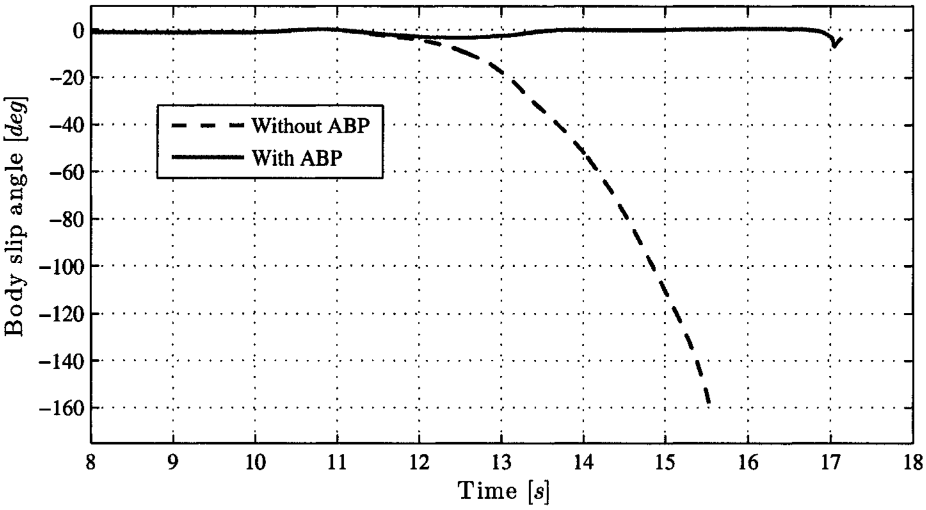

Figure C.6: *Braking and cornering with obstacle (inside swerve, no ABS): Body slip angle.* The body slip angle of the *ABP* and non-*ABP* vehicles are shown, for the braking with obstacle avoidance maneuver. The slip angle trend for the *ABP* vehicle is typical for a cornering vehicle performing a lane-change maneuver. The slip angle for the non-*ABP* vehicle grows excessively large, signifying that the vehicle has spun around, out of control.

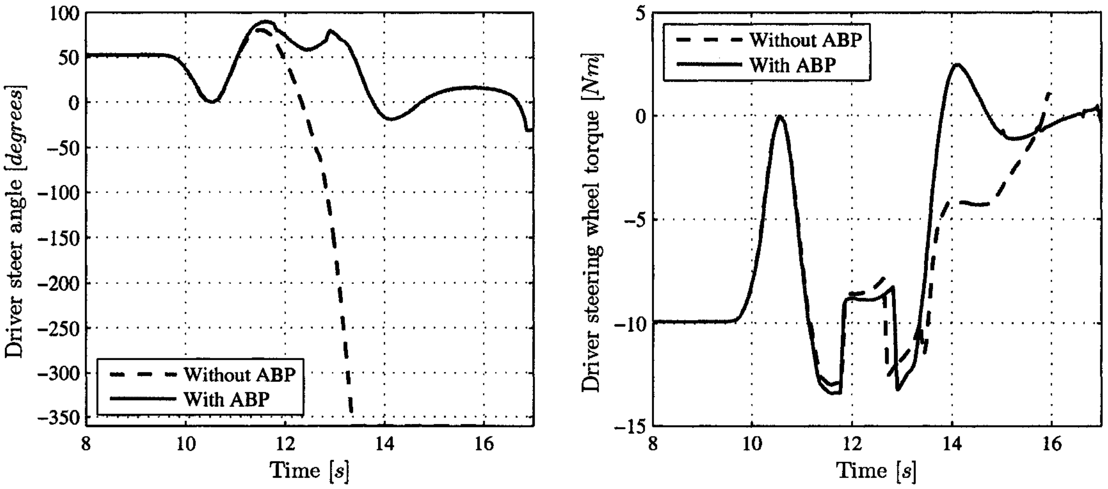

Figure C.7: *Braking and cornering with obstacle (outside swerve, no ABS): Steering wheel angle and steering wheel torque.* The steering wheel and steering torque results are presented. For the baseline vehicle, the steering angle goes to −360° as the vehicle loses control.

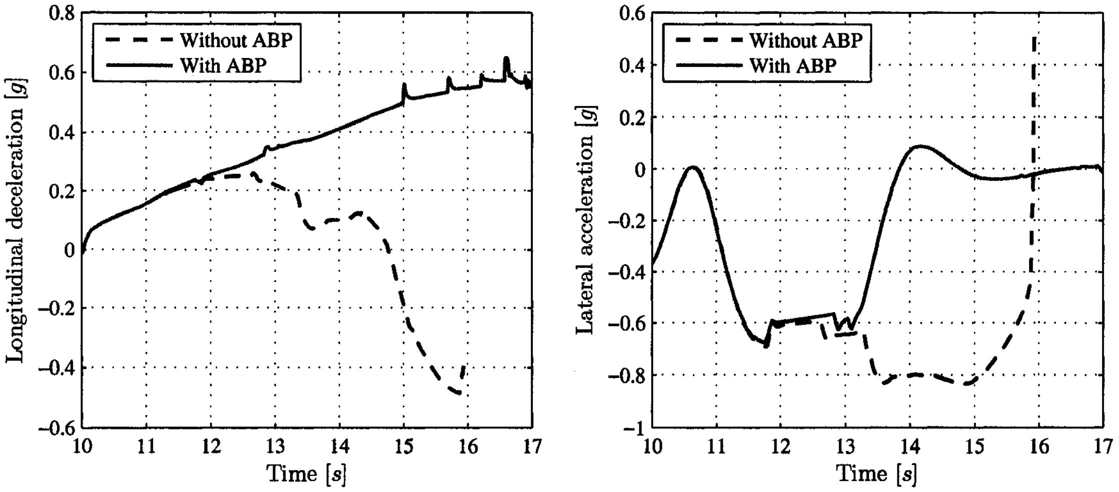

Figure C.8: *Braking and cornering with obstacle (outside swerve, no ABS): Longitudinal deceleration and lateral acceleration.* The longitudinal deceleration, and lateral acceleration are presented. The *ABP* vehicle achieves a longitudinal deceleration of 0.6 g, while the baseline vehicle loses control and does not decelerate as intended.

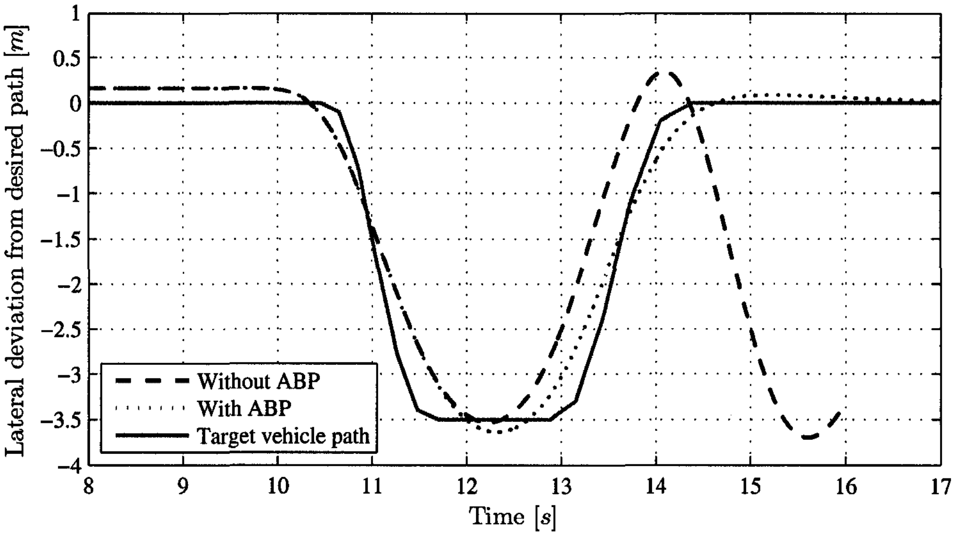

Figure C.9: *Braking and cornering with obstacle (outside swerve, no ABS): Lateral deviation from desired path.* The desired path of the vehicles, relative to the curved path, is shown by the solid line. The *ABP* vehicle completes the double lane change and returns to the desired path. The baseline vehicle loses control while attempting to bring the vehicle back onto the curved path after the lane change maneuver.

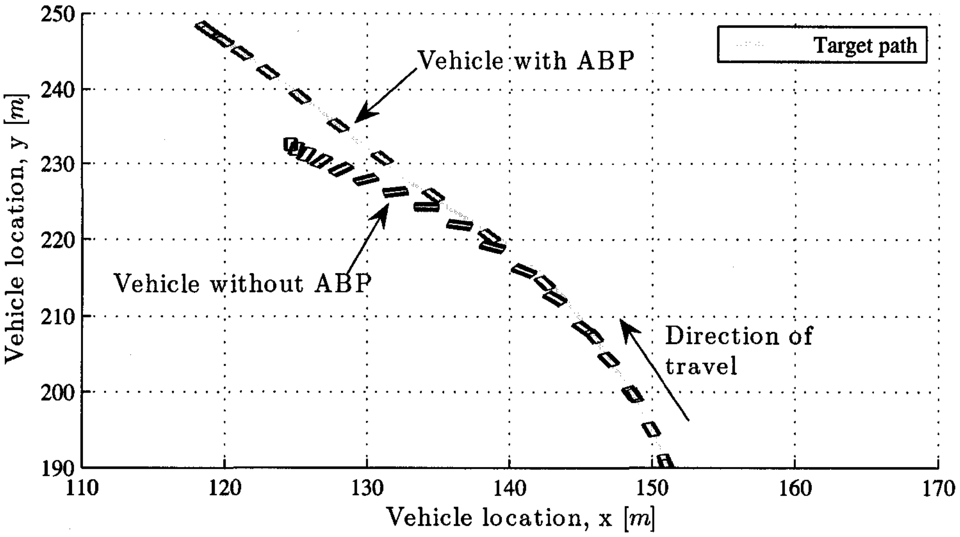

Figure C.10: *Braking and cornering with obstacle (outside swerve, no ABS): Vehicle trajectory.* The driving paths (location and heading) of the vehicles are shown from an overhead view. The vehicles are represented as small rectangles, in the proportions of an automobile. Observe that the baseline vehicle leaves the desired path and spins backwards, while the *ABP* vehicle follows the path.

C.2.1 Braking and cornering with obstacle (outside swerve): ABS vehicles

Table C.2: *Braking and cornering with obstacle (outside swerve, with ABS): Simulation results summary*

Vehicle model	Stopping time	Change	**Position**
Baseline	6.6 s		off path, spun out
Controlled	7.05 s	17.5 %	on path

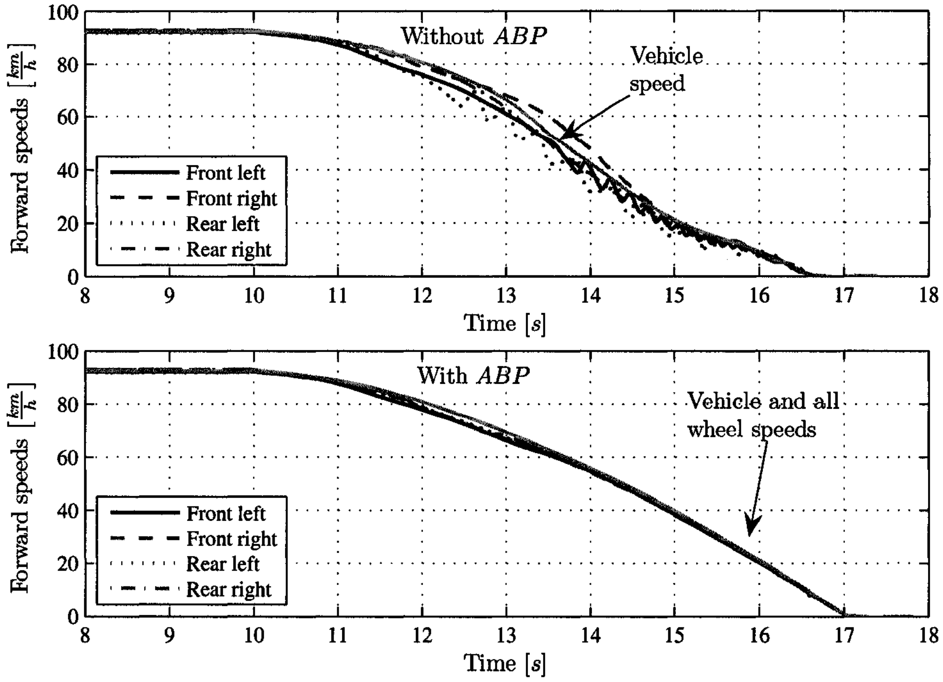

Figure C.11: *Braking and cornering with obstacle (outside swerve, with ABS): Wheel and vehicle forward speeds.* The speeds of the vehicles and each wheel during the braking and cornering with obstacle event are presented. Again, no tires lock up for the *ABP* vehicle, and thus ABS actuation is not required. The baseline vehicle requires ABS for the inside rear tire early in the maneuver. With the addition of ABS, the baseline vehicle heading does not fully reverse, thus the velocity remains positive.

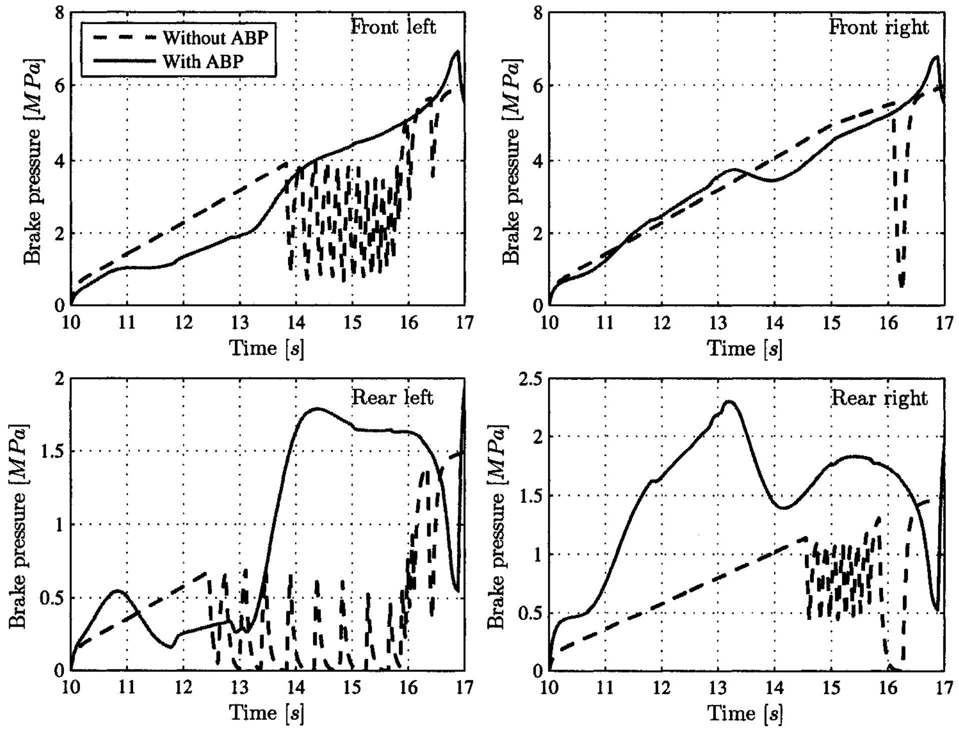

Figure C.12: *Braking and cornering with obstacle (outside swerve, with ABS): Brake pressure.* The brake pressures applied at each wheel during the braking and cornering with obstacle event are presented. The *ABP* vehicle prevents the need for any ABS braking, while all four tires on the baseline vehicle require ABS.

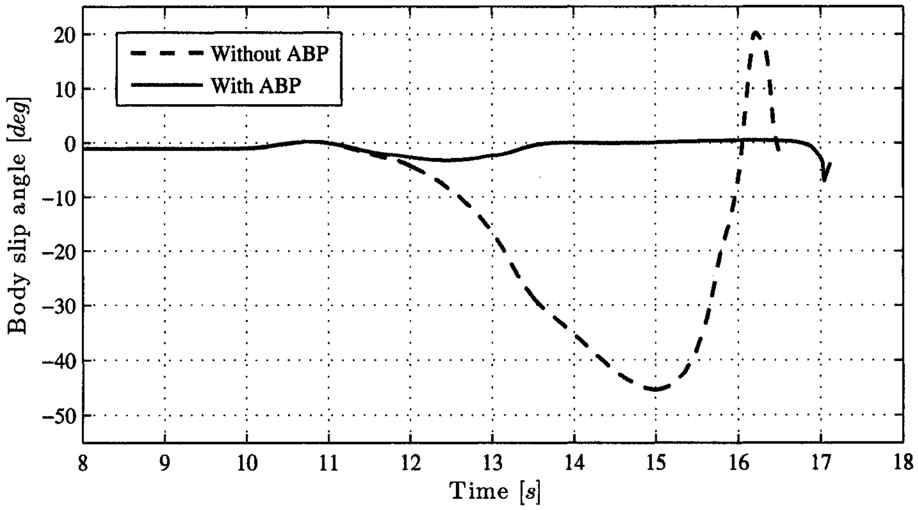

Figure C.13: *Braking and cornering with obstacle (inside swerve, with ABS): Body slip angle.* The body slip angle of the ABS-equipped *ABP* and non-*ABP* vehicles are shown, for the braking with obstacle avoidance maneuver. The slip angle trend for the *ABP* vehicle is typical for a cornering vehicle performing a lane-change maneuver. The slip angle for the non-*ABP* vehicle grows excessively large, signifying that the vehicle has spun around, out of control.

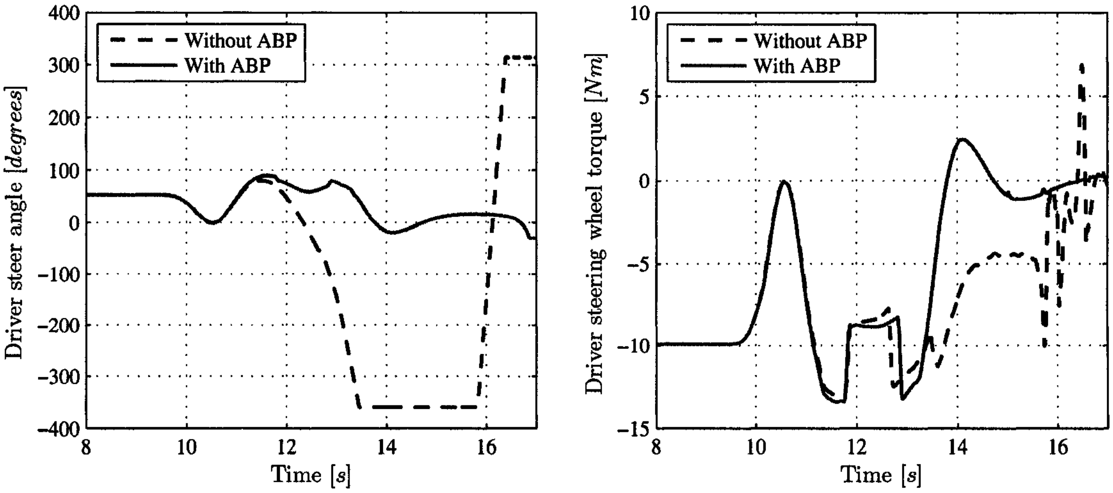

Figure C.14: *Braking and cornering with obstacle (outside swerve, with ABS): Steering wheel angle and steering wheel torque.* The steering wheel and steering torque results are presented. The results are very similar to the non-ABS case. The *ABP* vehicle shows the trends expected for a double lane change, while the baseline vehicle loses control.

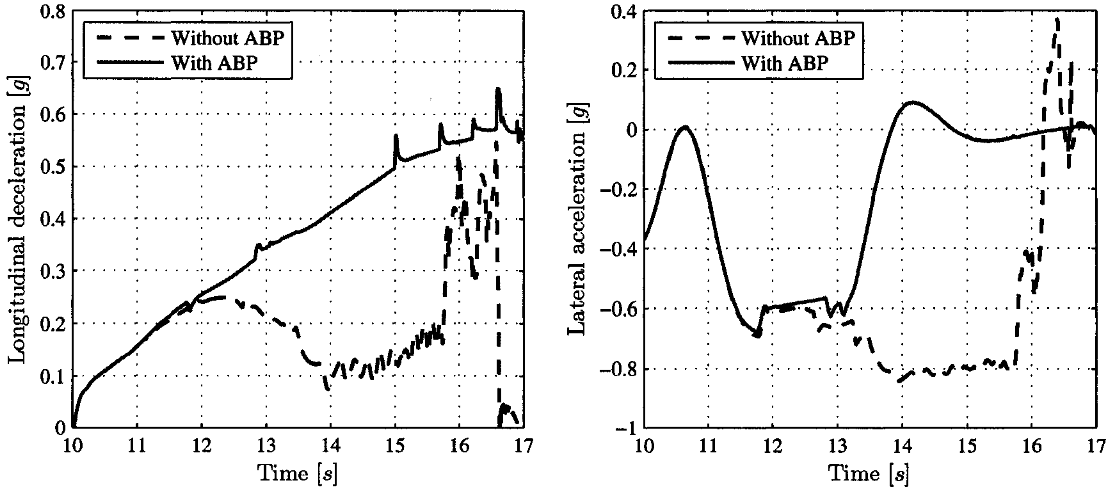

Figure C.15: *Braking and cornering with obstacle (outside swerve, with ABS): Longitudinal deceleration and lateral acceleration.* The longitudinal deceleration, and lateral acceleration are presented. Similar to the non-ABS case, the *ABP* vehicle generates the expected longitudinal and lateral accelerations, while the baseline vehicle loses traction and fails to generate accelerations as expected.

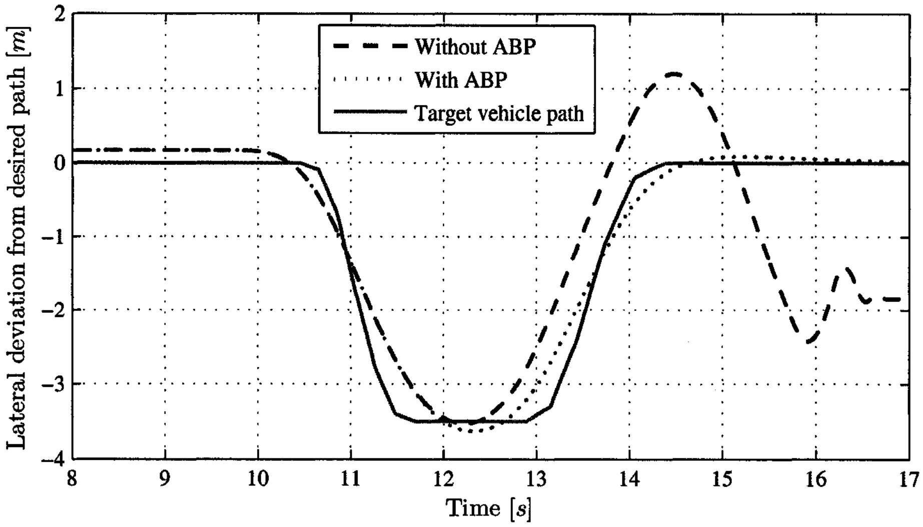

Figure C.16: *Braking and cornering with obstacle (outside swerve, with ABS): Lateral deviation from desired path.* The desired path of the vehicles, relative to the curved path, is shown by the solid line. The *ABP* vehicle completes the double lane change and returns to the desired path. The baseline vehicle loses control while attempting to bring the vehicle back onto the curved path after the lane change maneuver.

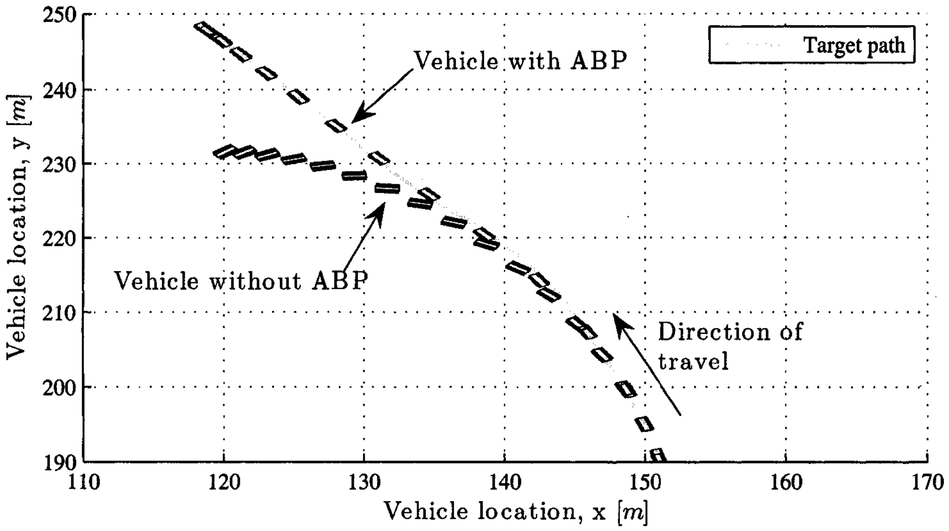

Figure C.17: *Braking and cornering with obstacle (outside swerve, with ABS): Vehicle trajectory.* The driving paths (location and heading) of the vehicles are shown from an overhead view. The vehicles are represented as small rectangles, in the proportions of an automobile. Observe that, as in the non-ABS case, the baseline vehicle leaves the desired path and spins , while the *ABP* vehicle follows the path. The baseline vehicle in this case ends up rotated ~ 90° from the proper heading.

Vita Auctoris

Nathan C. Nantais was born on October 14, 1981, in Windsor, Ontario, Canada. He graduated from Holy Names High School in 2000. He then attended the University of Windsor, where he earned the degree of Bachelor of Applied Science in Mechanical Engineering, Automotive Option, with Great Distinction. He is presently a candidate for the Master of Applied Science in Mechanical Engineering degree at the University of Windsor, and is scheduled to graduate in October 2006.